3-1-2013

Pupil wavefront manipulation for the compensation of mask topography effects in optical nanolithography

Monica Sears

PUPIL WAVEFRONT MANIPULATION FOR THE COMPENSATION OF MASK TOPOGRAPHY EFFECTS IN OPTICAL NANOLITHOGRAPHY

by

MONICA KEMPSELL SEARS

A DISSERTATION

Submitted in partial fulfillment of the requirements
For the degree of Doctor of Philosophy
in
Microsystems Engineering
Kate Gleason College of Engineering
at the
Rochester Institute of Technology

March 2013

Author: _____

Monica Kempsell Sears
Microsystems Engineering Program

Certified by: _____

Bruce W. Smith, Ph.D.
Professor of Microsystems Engineering

Approved by: _____

Bruce W. Smith, Ph.D.
Director of Microsystems Engineering Program

Certified by: _____

Harvey J. Palmer, Ph.D.
Dean, Kate Gleason College of Engineering

NOTICE OF COPYRIGHT

REPRODUCTION PERMISSION STATEMENT

Permission Granted

TITLE:

"PUPIL WAVEFRONT MANIPULATION FOR THE COMPENSATION OF MASK TOPOGRAPHY EFFECTS IN OPTICAL NANOLITHOGRAPHY"

Signature of Author:_____ Date: _____

Pupil Wavefront Manipulation for the Compensation of Mask Topography Effects in Optical Nanolithography

By

Monica Kempsell Sears

Submitted by Monica Kempsell Sears in partial fulfillment of the requirements for the degree of Doctor of Philosophy in Microsystems Engineering and accepted on behalf of the Rochester Institute of Technology by the dissertation committee.

We, the undersigned members of the Faculty of the Rochester Institute of Technology, certify that we have advised and/or supervised the candidate on the work described in this dissertation. We further certify that we have reviewed the dissertation manuscript and approve it in partial fulfillment of the requirements of the degree of Doctor of Philosophy in Microsystems Engineering.

Approved by:

Dr. Bruce W. Smith _____
(Committee Chair and Dissertation Advisor) Date

Dr. Roger Gaborski _____
(Committee Member) Date

Dr. Zhaolin Lu _____
(Committee Member) Date

Dr. Robert Socha _____
(Committee Member) Date

Dr. Grover Swartzlander _____
(Committee Member) Date

KATE GLEASON COLLEGE OF ENGINEERING
MICROSYSTEMS ENGINEERING PROGRAM
ROCHESTER INSTITUTE OF TECHNOLOGY

March 2013

ABSTRACT

Kate Gleason College of Engineering
Rochester Institute of Technology

Degree: Doctor of Philosophy **Program:** Microsystems Engineering

Name of Candidate: Monica Kempsell Sears

Title: Pupil Wavefront Manipulation for the Compensation of Mask Topography Effects in Optical Nanolithography

As semiconductor optical lithography is pushed to smaller dimensions, resolution enhancement techniques have been required to maintain process yields. For some time, the customization of illumination coherence at the source plane has allowed for the control of diffraction order distribution across the projection lens pupil. Phase shifting at the mask plane has allowed for some phase control as well. However, geometries smaller than the imaging wavelength introduce complex wavefront effects that cannot be corrected at source or mask planes. Three dimensional mask topography effects can cause a pitch dependent defocus (ΔBF), which can decrease the useable depth of focus (UDOF) across geometry of varying density. Wavefront manipulation at the lens pupil plane becomes necessary to provide the degrees of freedom needed to correct for such effects. The focus of this research is the compensation of such wavefront phase error realized through manipulation of the lens pupil plane, specifically in the form of spherical aberration. The research does not attempt to improve the process window for one particular feature, but rather improve the UDOF in order to make layouts with multiple pitches possible for advanced technology nodes.

The research approach adopted in this dissertation includes rigorous simulation, analytical modeling, and experimental measurements. Due to the computational expense of rigorous calculations, a smart genetic algorithm is employed to optimize multiple spherical aberration coefficients. An analytical expression is formulated to predict the best focus shifts due to spherical aberration applied in the lens pupil domain. Rigorously simulated trends of best focus (BF) through pitch and orientation have been replicated by the analytical expression. Experimental validation of compensation using primary and secondary spherical aberration is performed using a high resolution wavefront manipulator. Subwavelength image exposures are performed on four different mask types and three different mask geometries. UDOF limiting ΔBF is observed on the thin masks for contact holes, and on thick masks for both one directional (1D) and two directional (2D) geometries. For the contact holes, the applied wavefront correction decreases the ΔBF from 44 nm to 7 nm and increases the UDOF to 109 nm, an 18% improvement. For the 1D geometries on a thick mask, the through pitch UDOF is increased from 59 nm to 108 nm, an 83% improvement. Experimental data also shows that an asymmetric wavefront can be tuned to particular geometries, providing a UDOF improvement for line ends under restricted processing conditions.

The experimental data demonstrates that pupil wavefront manipulation has the capability to compensate for mask topography induced ΔBF. This dissertation recommends that corrective spherical aberration coefficients be used to decrease pitch dependent best focus, increase process yield, and ultimately expand the design domain over parameters such as mask materials and mask feature densities. The effect of

spherical aberration applied in the pupil plane is to provide a wavefront solution that is equivalent to complex multiple-level mask compensation methods. This will allow the advantages of thicker masks to be explored for further applications in semiconductor optical lithography.

Abstract Approval: Committee Chair: _____

Program Director: _____

Dean, KGCOE: _____

ACKNOWLEDGMENTS

First and foremost, I want to thank my parents, Jim and Lesley Kempsell, for encouraging and believing in me. I thank Pama, my grandmother, for always supporting my education. I thank my husband, Tom Sears, for his love and support, as well as my in-laws, Mike & Joan Sears and Wayne and Diana Pete. I thank Wendy Kempsell Jacinto and James Kempsell for being the best siblings one could hope for and always lending an ear when needed. I would also like to show gratitude to my friends Chelsea Mackos and Jamie Swan for their moral support.

I sincerely thank my advisor, Dr. Bruce Smith, for not only kindling my interest in lithography more than 10 years ago, but for leading me through my research. It is a pleasure to thank my committee members Dr. Roger Gaborski, Dr. Zhaolin Lu, Dr. Robert Socha, and Dr. Grover Swartzlander for their guidance of my dissertation. I thank the RIT Nanolithography Research Lab members for their valuable discussions and their friendship; Neal Lafferty, Peng Xie, Andrew Estroff, Germain Fenger, Burak Baylav, and Christopher Maloney. I acknowledge the assistance I've received from the Microsystems faculty and staff, especially Sharon Stevens and Lisa Zimmerman. I am indebted to the IMEC lithography department for providing me with the tools and materials required for the experimental portion of my research. I owe my deepest gratitude to Joost Bekaert for many valuable discussions as well as countless hours in the cleanroom. I am grateful to Lieve Van Look and Vicky Philipsen for their expertise and advice. I acknowledge KLA-Tencor for the use of PROLITH™ and PRODATA™. I also acknowledge the financial support I've received through the Semiconductor Research Corporation's Scholarship Program and the National Science Foundation's Graduate Research Fellowship Program.

TABLE OF CONTENTS

LIST OF FIGURES

LIST OF TABLES

LIST OF ACRONYMS

1D	One Directional [mask pattern]
2D	Two Directional [mask pattern]
3D	Three Dimensional [mask topography]
AltPSM	Alternating Phase Shift Mask
AttPSM	Attenuated Phase Shift Mask
CD	Critical Dimension
CPL	Chromeless Phase Lithography
BF	Best Focus
DOF	Depth of Focus
EL	Exposure Latitude
FEM	Focus Exposure Matrix
ILS	Image Log Slope
MEEF	Mask Enhancement Error Factor
MoSi	Molybdenum-Oxide Silicon-Oxide
MTF	Modulation Transfer Function
NILS	Normalized Image Log Slope
NTD	Negative Tone Development
OAI	Off-Axis Illumination
OPC	Optical Proximity Correction
OPD	Optical Path Difference
OPW	Overlapping Process Window
PSF	Point Spread Function
PSM	Phase Shift Mask
SEM	Scanning Electron Microscope
SCAAM	Sidewall Chrome Alternating Aperture Mask
SMO	Source Mask Optimization
SRAF	Sub-Resolution Assist Feature
TaSiON	Tantalum Silicon-Oxi-Nitride
UDOF	Useable Depth of Focus

1. INTRODUCTION

The semiconductor industry is driven by the downscaling of the integrated circuit in order to provide faster processing capabilities for the computers and smartphones of today. Douglas Englebart was the first to discuss the projected downscaling of integrated circuit size in a 1960 lecture [1]. Soon after, Gordon Moore's papers were published which led to the now well known Moore's law [2]–[4]. Lithography has become the bottleneck of the industry, relied upon to continually provide higher resolution features with large process latitudes. In order to meet demands, the lithography community has decreased the exposure wavelength and increased the size of the projection optics. Now, with an exposure wavelength of 193 nm, material limitations prevent further scaling [5], [6].

In order to reach the 22 nm node and beyond with optical lithography, double or even triple patterning will likely be used with systems capable of printing a pitch (p) of 80 nm [7], [8]. However, imaging with subwavelength mask features cause phenomena commonly referred to as mask topography effects, that result in different optimal process conditions for each feature density. This dissertation addresses the issue of printing multiple feature densities on a single layout with an acceptable overlapping process latitude.

In this section, first an introduction to lithography is given. Then the analysis of a focus exposure matrix is presented. Next, the resolution enhancement techniques that

have been instrumental in extending optical lithography are discussed. Finally, the problem statement and approach are reviewed.

1.1 Projection optical lithography

1.1.1 Lithography system

Optical lithography is the semiconductor fabrication process used along with etching to create a pattern on the wafer. Near UV radiation of wavelength λ is used to transfer a pattern from the mask into a light sensitive and etch resistant film (resist), which is then etched into the underlying film or substrate. Positive resist creates a resist pattern corresponding to the dark regions of the mask, whereas the pattern due to negative resist corresponds to the transparent regions. Lithographic pattern transfer originated as a contact system, where the mask was in contact with the wafer, but this resulted in contamination and damage to the mask. Proximity printing provided a small gap between the mask and wafer which prevented damage; however, the minimum feature size was limited by the feature size on the mask. Projection lithography uses a projection lens system to minify the features on the mask. This reduction allows nanometer sized features to be resolved, limited only by diffraction [9].

A projection lithography system has four primary stages; source, mask, objective lens, and wafer. In a Köhler illumination setup, the source is imaged onto the entrance pupil of the objective by the condenser optics, and the mask is imaged onto the wafer by the objective optics. A simple diagram is shown in Figure 1, where the marginal rays from both the source and the mask are drawn. Note that the objective lens is modeled as the entrance pupil (NP) and exit pupil (XP). Since the source is imaged to the entrance pupil plane, each point in the source becomes a plane wave at the mask. This setup is

ideal for non-uniform sources since it allows the mask to be illuminated with uniform light.

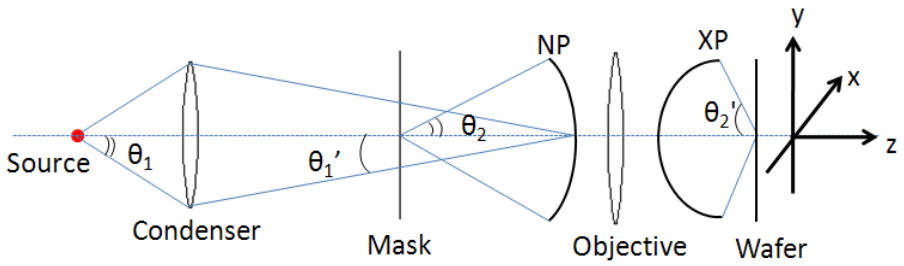

Figure 1: Schematic of Köhler illumination. NP/XP is the entrance/exit pupil of the objective lens. Polar coordinate of the objective lens is (r, φ).

The numerical aperture is defined as the refractive index of the imaging material multiplied by the sine of the half angle. In air, the numerical aperture on the condenser side is NA_c=sin(θ_1) and the numerical aperture of the objective is NA=sin(θ_2'). An immersion lithography system utilizes a high index material between the last projection element and the wafer in order to increase the NA of the objective; NA=$n$sin(θ_2'). For incoherent light, the ratio of NA_c to NA is defined as the partial coherence, σ. The resolution, defined as the minimum achievable half pitch, is determined by the partial coherence, the exposure wavelength, and the NA of the objective.

$$hp_{min} = \frac{p_{min}}{2} = \frac{\lambda}{2(\sigma + 1)NA} \quad (1)$$

This resolution equation, derived from Rayleigh's imaging equations, is commonly referred to as "Rayleigh's criteria" [10]. The reduction ratio, R, can be calculated as the ratio of the angle in the exit pupil to the angle in the entrance pupil. The inverse of the reduction ratio is defined as the transverse magnification, M_T.

$$M_T = \frac{1}{R} = \frac{\sin(\theta_2')}{\sin(\theta_2)} = \frac{u'}{u} = \frac{v'}{v} \quad (2)$$

A convenient notation method is to use direction cosines in the frequency domain: $u = cos\varphi sin\theta$, $v = sin\varphi sin\theta$, $\gamma = cos\theta$ defined so that $u^2+v^2+\gamma^2=1$. The angle θ is in the meridional plane, defined by the yz plane, and φ is in the xy plane. The entrance pupil plane of the objective lens is defined in coordinates of (u,v), and the coordinates in the exit pupil are defined as (u',v'). In order to conserve the energy transferred from entrance to exit pupil, a magnification induced obliquity factor relates the object side electric field to the image side electric field.

The diagram in Figure 1 is drawn assuming partially coherent light, where the mask is illuminated by plane waves with a small range of angles. If coherent light was used, the source could be modeled as a point source, and the mask would be imaged with a single plane wave. The schematic is a simplified setup, whereas a real tool's projection optic is made up of numerous elements in order to decrease the angle of propagation through each lens to decrease the effect of residual aberrations. Numerous optical design considerations have been studied for optimizing optical lithography lens systems [11]–[13]. One design technique that is commonly used is called double telecentricity, where the entrance pupil and exit pupil are both imaged at infinity [14]. This allows the principal ray (centered in a fan of rays) to be parallel to the optical axis. This is done in order to maintain exact magnification as the object or image plane are run through focus, such as through topographical requirements, since the angle of the principal ray will not change.

1.1.2 Focus exposure matrix

The cutline of the aerial image intensity from periodic equal lines and spaces (a 1:1 duty ratio) is shown in Figure 2. This aerial image (AI) is calculated with 3 beam coherent imaging; the interference between the 0^{th} diffraction order and the $\pm1^{st}$ diffraction orders. The AI is shown both in focus (blue) and with some amount of defocus (red). For this aberration free system, there exists a horizontal position, x_I, where the intensity does not vary as a function of focus, defined as the isofocal point. The isofocal intensity, shown in green, represents the threshold which would result in a constant critical dimension (CD) through focus. The isofocal point can be found from the derivative of the aerial image with respect to defocus, δ. The AI's phase error in the pupil plane induced by defocus, given in Equation 3, is a function of the optical path difference (OPD) between the ideal spherical wavefront in focus and out of focus.

$$\Phi = \frac{2\pi}{\lambda} OPD = \frac{2\pi}{\lambda} n\delta(1 - \cos\theta) \approx \frac{2\pi}{\lambda} n\delta\left(\frac{1}{2} sin\theta^2\right) \tag{3}$$

The approximation in Equation 3 is done by truncating the Taylor series expansion after the first term, thus is only valid at small angles. This phase error is due to the paraxial defocus, where the OPD from a spherical wavefront is approximated by a parabola [15]. A common representation of OPD uses Zernike polynomials to decompose the pupil plane phase, discussed further in section 2.1.4. The Zernike polynomial attributed to the paraxial defocus, z_4, has a simple relationship to the defocus distance [16].

$$z_4 = \frac{\delta NA^2}{4\lambda} \tag{4}$$

The exact defocus due to a sphere shaped wavefront would require the inclusion of higher order Zernike polynomials. The electric field at the wafer for a space *s* and pitch *p* (which is derived in section 2.1.1) is a function of the phase error in the pupil plane, Φ.

$$A(x) = \frac{s}{p} + 2\frac{s}{p} sinc\left(\frac{s}{p}\right) e^{\mathrm{i}\Phi} cos\left(\frac{2\pi x}{p}\right) \tag{5}$$

The irradiance is found from the complex square of the electric field, using the identities $e^{i\Phi} + e^{-i\Phi} = 2\cos\Phi$ and $2\cos^2 x = 1 + \cos(2x)$.

$$\mathrm{I(x)} = A(x)^2 = \left(\frac{s}{p}\right)^2 + 4\left(\frac{s}{p}\right)^2 sinc\left(\frac{s}{p}\right)\cos(\Phi)\ cos\left(\frac{2\pi x}{p}\right)$$

$$+2\left(\frac{s}{p}\right)^2 sinc^2\left(\frac{s}{p}\right)\left(1 + cos\left(\frac{4\pi x}{p}\right)\right) \tag{6}$$

Equation 5 shows that the defocus phase error demodulates the fundamental cosine term. The derivative of irradiance with respect to defocus is:

$$\frac{\partial \mathrm{I}}{\partial \delta} = -4\left(\frac{s}{p}\right)^2 sinc\left(\frac{s}{p}\right)\sin(\Phi)\ cos\left(\frac{2\pi x}{p}\right)\left(\frac{2\pi n}{\lambda}(1 - \cos\theta)\right) \tag{7}$$

Setting $\partial \mathrm{I}/\partial\delta = 0$ and solving for x_I, the equation simplifies to $0 = \cos(2\pi x_I/p)$. Thus x_I, the isofocal point, is found to be at $p/4$, or half of the space size for features with 1:1 duty ratio.

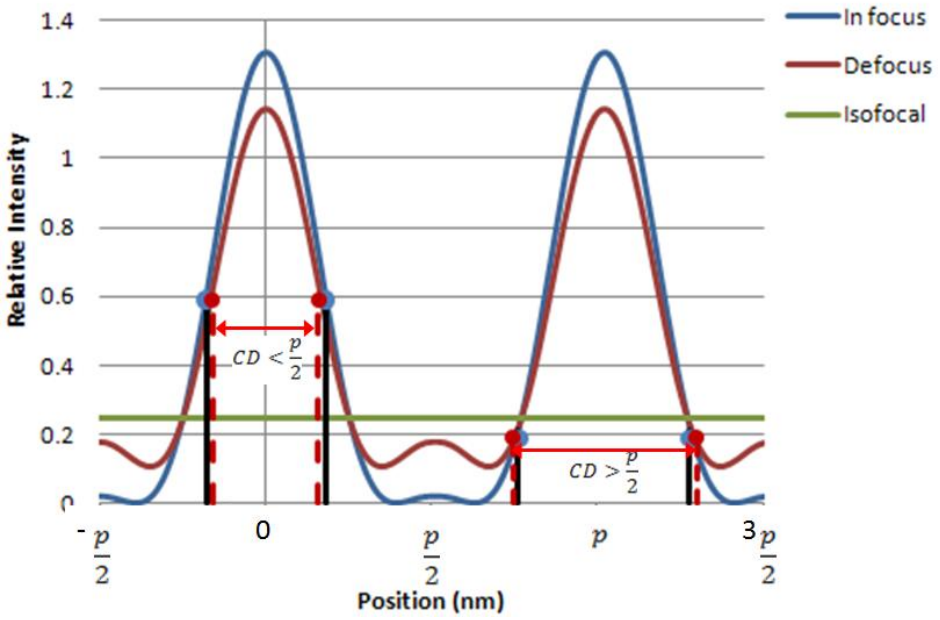

Figure 2: Calculation of aerial image space CD using intensity threshold. The space CD decreases when out of focus if an intensity threshold greater than the isofocal intensity (green) is used, and the space CD increases out of focus when the intensity threshold is less than the isofocal intensity.

Here, an example is given to show the calculation of the best focus (BF) and depth of focus (DOF) [17]. Calculations of a 45 nm line imaged into air were done with a vector-based lithography image simulator, KLA-Tencor PROLITH^{TM} [18]. First, line CD through focus is plotted at multiple exposure doses, shown in Figure 3a. The dose is calculated as the inverse of the aerial image intensity threshold. With an applied dose of 2 mJ/cm^2, the CD remains rather constant through focus, so that particular dose is deemed the isofocal dose. For an applied dose larger than the isofocal dose, the line CD will be smaller, especially when out of focus. For an applied dose smaller than the isofocal dose, the line CD will be larger, especially when out of focus. This plot is defined as a focus exposure matrix (FEM) where the dose is on the z axis. FEM fitting equations have been derived in order to accurately predict the physics [19]. The BF is defined as the center of the FEM, which is 0 nm in this aberration-free aerial image system.

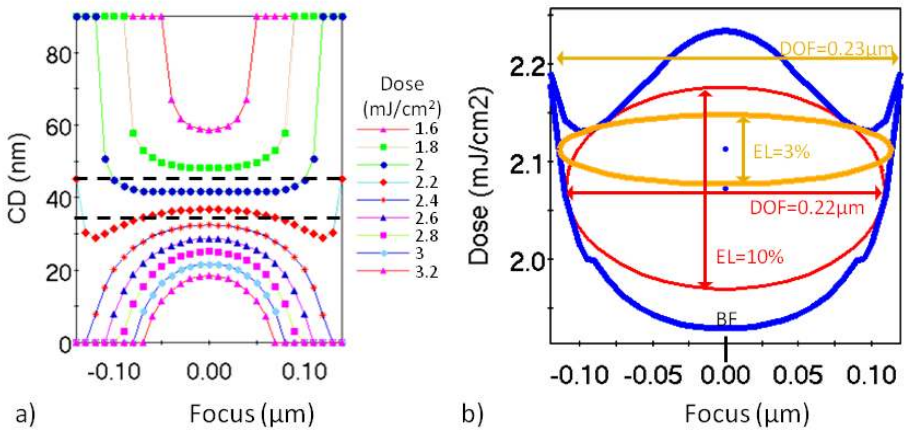

Figure 3: a) FEM for 45 nm line simulated in PROLITH™. Black dashed lines represent process conditions which result in CD values within ±10% specification b) Process latitude is found by fitting an ellipse inside the process window (blue). Larger DOF can be found with a smaller EL.

Next, the process window was found by finding the range of parameters over which the CD remains acceptable, shown as blue in Figure 3b. When using criteria of ±10% CD, this FEM reveals that when including the ranges of dose from 1.97 to 2.17, the acceptable focus range is from -0.11µm to +0.11 µm, shown as the red ellipse in Figure 3b. The depth of focus (DOF) is defined as this acceptable range in defocus values; DOF= 0.22 µm. A larger DOF can be found by using a smaller range of doses from 2.09 to 2.15, shown as the orange ellipse in Figure 3b with an exposure latitude of 3%. The exposure latitude (EL) is defined as the acceptable range in exposure values, normalized to the exposure. The process latitude can be calculated as the product of DOF and EL, and is directly proportional to the yield of the process. Often the process latitude is defined as the DOF at a specified EL. The FEM of an aberration free system is very straightforward to compute, but becomes more complex when objects that induce aberrations, such as resist or mask topography, are included.

1.2 Resolution enhancement techniques

In addition to wavelength and numerical aperture scaling, several significant advances have been made to extend the resolution of optical lithography. Each resolution enhancement technique (RET) is based on the fundamentals of projection optics, first described by Airy in 1835 [20]. RET is typically implemented at the mask plane to modify the amplitude (OPC), phase (PSM), and direction (OAI) of the wavefront. In this section, methods to optimization the mask (OPC/PSM) and the source (OAI) will be reviewed, as well as the field of joint source mask optimization (SMO).

1.2.1 Mask optimization

1.2.1.1 Optical Proximity Correction (OPC)

Optical Proximity Correction (OPC) improves the output image by fundamentally changing the amplitude of the diffraction orders leaving the mask. OPC is not a young technology; in the 1960s, corners of a microphotograph object underwent a serif treatment to compensate for corner rounding [21]. In the early 1980s, Bahaa Saleh's research group studied compensation for high-contrast imaging in an iterative approach, which eventually gave rise to today's field of computational OPC [22]–[24].

OPC gets its name from the phenomenon that the image of identical features is different based on the neighboring features in proximity [25]–[28]. This causes a line with a 1:1 duty ratio to produce a different aerial image than a line that is isolated. An aerial image's bias is the amplitude of the 0^{th} diffraction order, which is $(s/p)^2 = (1/2)^2 = 0.25$ for 1:1 lines and $(3/4)^2 = 0.56$ for 1:3 lines, as shown in Figure 4 [29]. This difference in bias means that at a given exposure dose, the CD of these features will

be different, especially when out of focus, resulting in a degraded DOF for isolated features. Rule based correction methods enlarge isolated features so that they print at the same dimension as dense features [30]–[32].

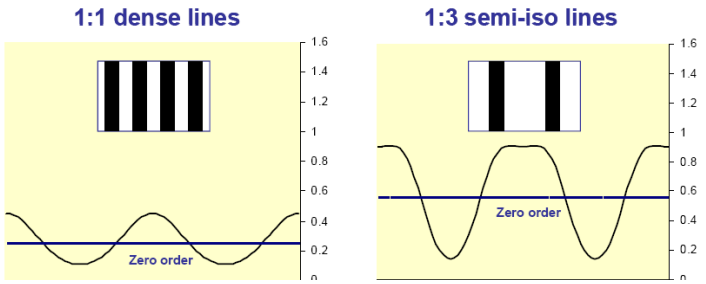

Figure 4: Aerial image of 1:1 and 1:3 lines

Another method of OPC is to introduce sub-resolution assist features (SRAFs) which modify the aerial image but do not resolve individually [33]. Figure 5 shows that the aerial images for various duty ratios have biases from 0.4 up to 0.8. With the introduction of SRAFs, the range in bias is only from 0.4 to 0.5. This improvement allows for the same size lines to have a similar CD through pitch [29]. The enhancement by SRAFs is due to the modification of the features to appear similar to the dense pitch which has the optimized illumination. Since the SRAFs cause the isolated features to appear optically dense, their DOF is increased. Additional SRAF techniques include those that have tunable transmission [34], [35].

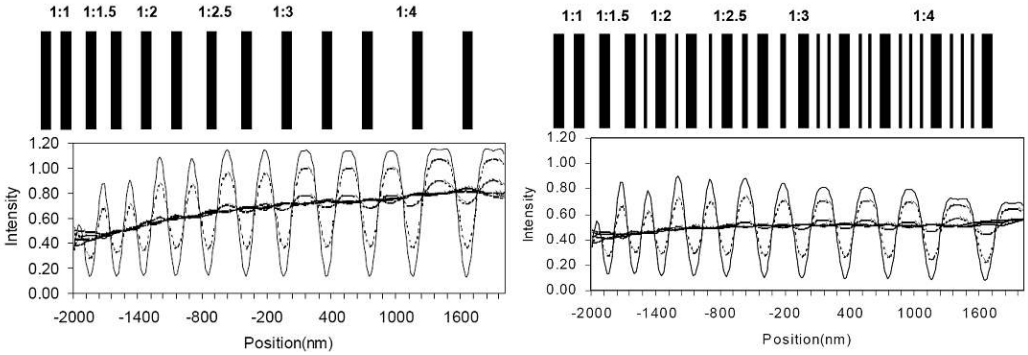

Figure 5: Introduction of SRAF provides similar bias through pitch

OPC for one directional (1D) lines is relatively straightforward but becomes very difficult with increasing pattern complexity. For two directional (2D) features, such as 90° turns and line ends, OPC features have been added to improve imaging. Common features added are negative serifs at the corner to counteract corner rounding, and positive serifs at the corners of a line end to counteract line end pullback [36], [37]. Examples of masks with OPC are shown in Figure 6 [38]. The dimensions of the serifs are too small to be resolved on the wafer because the high frequency content of the mask is not passed through the objective lens. But the serifs are successful in modifying the image by adjusting the zero-frequency content, or the local bias of the image. Their functionality can be described as dose compensation since they adjust the "local dose," which changes the dose to print a feature on target, or likewise changes the printed size for a given dose [37].

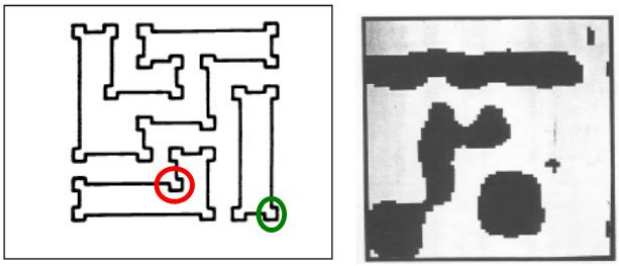

Figure 6: Masks modified with optical proximity correction. Negative serif circled in red, positive serif circled in green.

Masks become progressively more difficult to correct with smaller feature sizes. OPC algorithms have been developed to cope with the ever increasing complexity. In the early 90s, a model-based approach was developed to model systematic proximity effects according to Gabor's 1946 "Structural Theory of Information" [39]. This method involves two dimensional convolutions within a proximity domain at specified target points [40]. Edge modifying algorithms are now most common, in which the mask

feature's edges are segmented and moved iteratively to converge to the target aerial image [41]. The field of computer aided design (CAD) for lithography has now become an essential part of lithography optimization. CAD requirements have become increasingly demanding as feature sizes decrease and thus products have been developed to address specific challenges, such as reflective notching [42], process latitude based optimization [43], [44], mask topography effects [45], and full-chip OPC [46].

1.2.1.2 Phase Shift Masks

In 1879, Lord Rayleigh commented on the improved resolution a phase object would be expected to have [47], [48]. 100 years later, phase shifting was utilized for improved imaging at multiple locations around the world. In Germany, a phase shift object was used for holographic storage [49], at MIT one was used for enhancing x-ray lithography [50], and in Arizona, the theoretical pure phase object, now known as chromeless phase lithography (CPL), was studied [51]. In Japan at Nikon, a patent was filed that changed the phase of every other mask opening to reduce the fundamental frequency in half [52]. This allows phase shift masks (PSMs) to double the resolution since the objective lens is able to capture the ±1 diffraction orders for features half the size of the binary mask resolution limit [38]. Levenson at IBM then examined phase shifting both theoretically and experimentally [53], [54]. Many unique phase shifting technologies were invented, such as self aligned phase shifters [55], phase-edge shifters, rim shifters, and phase edge bessel masks [56]. Simulation and layout modification algorithms needed to be redesigned in order to handle the phase information of PSMs [57], [58], such as including the imaginary part of the transmission cross-coefficient [59], and applying the technology to logic layouts [60]–[63].

Figure 7 shows the mask schematic, electric field at the mask, diffraction pattern, electric field at the wafer, and intensity at the wafer for a binary mask as well as several types of PSMs. The schematic assumes that the mask is made of 1D periodic lines and spaces. The binary mask is generally made of chrome (Cr) on fused silica (Qz), where the Cr defines the areas in which light is blocked by the mask. The electric field at the mask then becomes high through the fused silica openings and zero at the chrome. The Fourier Transform of the 1D periodic mask features represents the discrete diffraction orders at locations corresponding to the grating equation; $p\sin\theta=m\lambda$, where an integer represents the m^{th} diffraction order. The objective lens acts as a low pass frequency filter, and for features near the resolution limit passes the 0 and ±1 orders. If the objective lens was able to transmit an infinite number of diffraction orders, the image would be a perfect reconstruction of the mask.

The electric field at the wafer becomes the inverse Fourier Transform of the filtered frequency spectrum, which is a biased cosine for binary 1D lines near the resolution limit. The bias comes from the 0^{th} diffraction order and the amplitude of the cosine comes from the amplitude of the 1^{st} diffraction orders. The aerial image is calculated as the square of the electric field at the wafer, shown in pink in Figure 7. The line CD is determined by thresholding the aerial image, which is a simplistic model of resist [64]. For positive tone resist, regions which have more intensity than the threshold become the spaces, and regions with intensity less than the threshold become the lines.

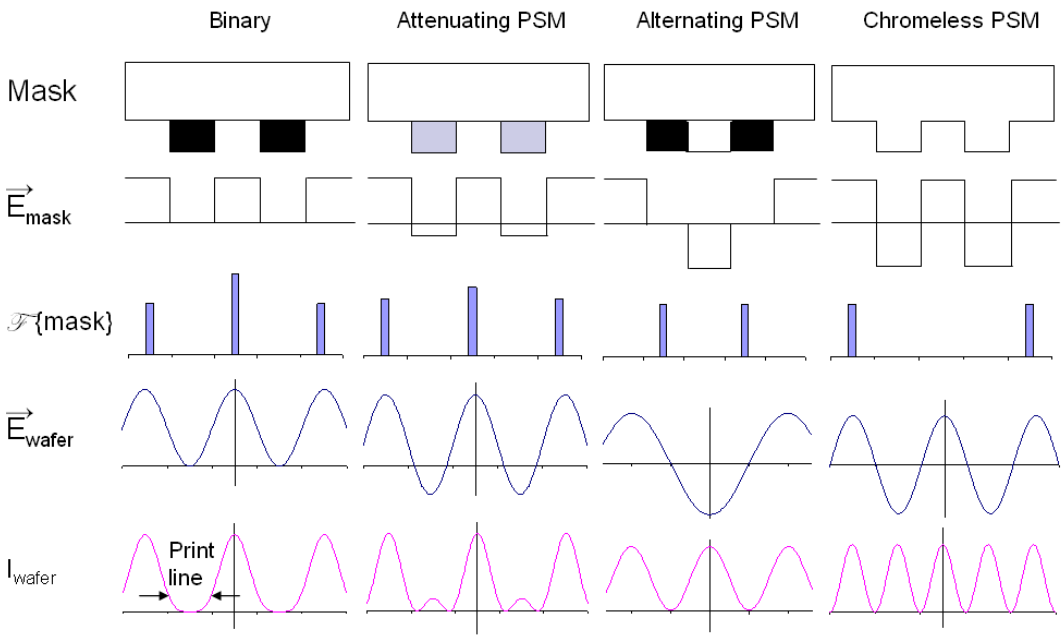

Figure 7: Schematics of binary and phase shift masks: electric field at the mask, Fourier Transform of the mask (diffraction pattern), electric field at the wafer, and intensity at the wafer (aerial image)

An attenuated phase shift mask (AttPSM) operates with a half wave (or π radians) phase shift between mask openings and neighboring dark regions [65]. By allowing some transmission in neighboring dark regions (such as 1-15%), the fraction of the passing light can be interfered with the phase shifted light transmitted through clear regions [66]. Through the careful selection and combination of absorbing and transmitting materials, this phase shift can be achieved together with the desired level of transmission. The AttPSM provides an edge enhancement effect since the resulting image electric field passes through zero, which ultimately leads to increased process latitude [67].

The alternating PSM (AltPSM) makes use of repetitive mask structures and a π phase change in the optical path length through alternating openings in between dark regions [53]. The phase shift of every other opening is achieved by etching into the fused silica mask substrate. Since the electric field at the mask for these features is negative, the

fundamental frequency of the mask is half of the binary mask. This results in ±1 diffraction orders closer together. In theory, the amplitude of the 0^{th} diffraction order is zero because the electric field at the mask averages to zero. The electric field at the wafer becomes an unbiased cosine, guaranteeing that the intensity between two spaces will always be zero [68]. The CPL mask contains two types of features, each with 100% transmission but one with a π phase shift. Again, the average electric field at the mask is zero, resulting in an unbiased cosine at the wafer. The intensity, electric field squared, becomes double the frequency of the binary mask, again doubling the resolution. The difficulty with images from a CPL mask is that the imaged lines correlate to the edges of mask features, requiring mask design for certain targets to include multiple phase levels, which increases complexity and cost [69].

Phase shift masks have proven to be useful in enhancing resolution as well as pattern fidelity. Generally, all lithographic processes in the 65 nm and 45 nm node employ some kind of phase shift mask, most commonly AttPSM [70]. Note that the previous discussion applies to coherent illumination; for a partially coherent source, an averaging effect removes such phenomena such as a zero intensity location for AttPSM. The discussion also utilizes the approximation that the electric field at the mask can be simply defined as a step function. For smaller features, the topography of the mask must be included which makes the analysis more complex.

1.2.1.3 Mask making technology

The materials used to achieve the desired phase and transmission have a large impact on the image quality of the system. In addition to chrome, additional metal absorbers to dictate the transmission include molybdenum (Mo), Hafnium (Hf), tantalum

(Ta), and tin (Ti) [71]–[73]. Common phase shifting materials include silicon dioxide (SiO_2) and silicon-oxi-nitride (SiON) [72]. As an example, a bi-layer AttPSM can be made by combining a Ta absorber layer with a SiON transparent layer to provide manipulation of both transmission and phase [74]. Earlier work has shown that a TaSiON AttPSM can provide image and process improvement compared to both Cr binary masks as well as thinner molybdenum-oxide silicon-oxide (MoSi) AttPSMs [75]. However, the use of multiple layers such as this may lead to thick mask effects, especially for low refractive index phase shifting layers and low absorbing attenuation layers that necessitate greater film thicknesses [76]. The thicker mask stack of the TaSiON has been shown to cause a pitch dependent best focus (BF) with a range of best focus, ΔBF, which degrades the useable depth of focus (UDOF) over multiple features, as discussed further in section 1.3.

A high transmission (Hi-T) AttPSM has been shown to provide process window enhancements such as reduced line end shortening, reduced corner rounding, and increased depth of focus [77]. The metrics of image log slope (ILS) and mask enhancement error factor (MEEF) have been analytically derived for Hi-T masks, which can be used to predict optimal contrast and CD control [78]. These masks, with a background intensity of 15% or more, can be achieved with a very thin MoSi absorber and an etch into Qz to dictate the 180º phase shift [79]. Hi-T masks have also been fabricated on Ta/SiO_2/Cr [80] and TaHf/SiON mask blanks [81]. The background transmission of Hi-T masks can result in background printing, which has been alleviated by a pixel based optimization that applies model-based SRAFs [82].

In theory, an AltPSM with coherent illumination provides high process latitude due to the guaranteed zero intensity between two adjacent spaces. However, in practice, scattered light from the etched feature reduces its transmission and causes an intensity imbalance [83]. The etched space has a smaller intensity than the un-etched space, resulting in line pairing; lines around the etched space print closer together than around the un-etched space. This undesired placement error effectively reduces the process latitude [84]. Several methods have been implemented to compensate for the intensity imbalance, including trench bias [85], undercuts [86], dual trench mask [87], and sidewall chrome alternating aperture mask (SCAAM) [88]. A dual trench mask is designed by optimizing the etch depth of both spaces while the phase difference between the two spaces is kept at 180º. Simulations performed in PROLITH^{TM} of a 50 nm line at a 120 nm pitch are shown in Figure 8, where the UDOF of the line, space, and shifted space is increased by the dual trench mask. For the dual trench mask in Figure 8b, the process window for the shifted space (purple) and the process window for the non-shifted space (brown) are symmetric within the process window for the line (yellow).

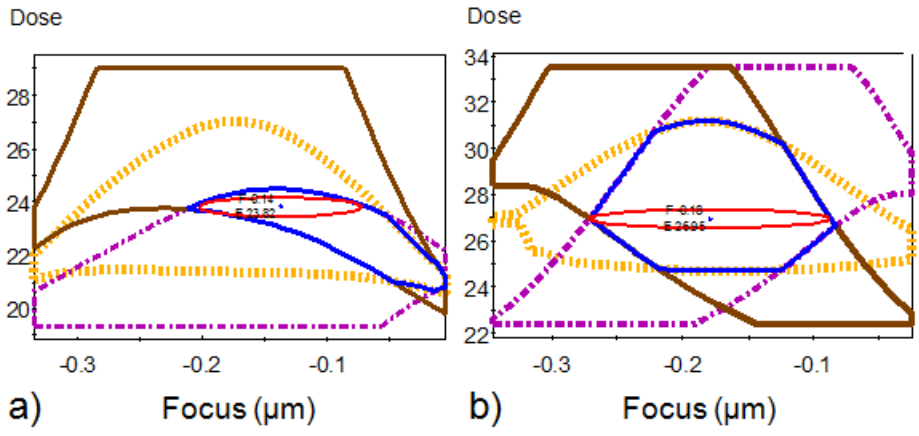

Figure 8: UDOF of 50 nm line and 70 nm space /shifted space in 120 nm pitch on a) single trench AltPSM is 130 nm and on a b) dual trench mask is 180 nm

The SCAAM reduces the impact of light scattering from glass edges by incorporating Cr on the sidewall of the etched feature [89]. The improvement is illustrated by simulations performed using the rigorous electromagnetic field modeler Dr.Litho, using the Waveguide method [90]. In Figure 9, the intensity imbalance in the aerial image is removed by a chrome width *W*=10 nm. In Figure 10, the 62 nm UDOF of the line, space, and shifted space is increased to 283 nm by the SCAAM. In Figure 10b, the process window for the shifted space (dashed) and the process window for the non-shifted space (dotted) are symmetric within the process window for the line (solid). Dual trench and SCAAM compensation methods can be successful in alleviating the intensity imbalance, however they have not been incorporated into high volume manufacturing due to the cost and complexity of numerous masking levels.

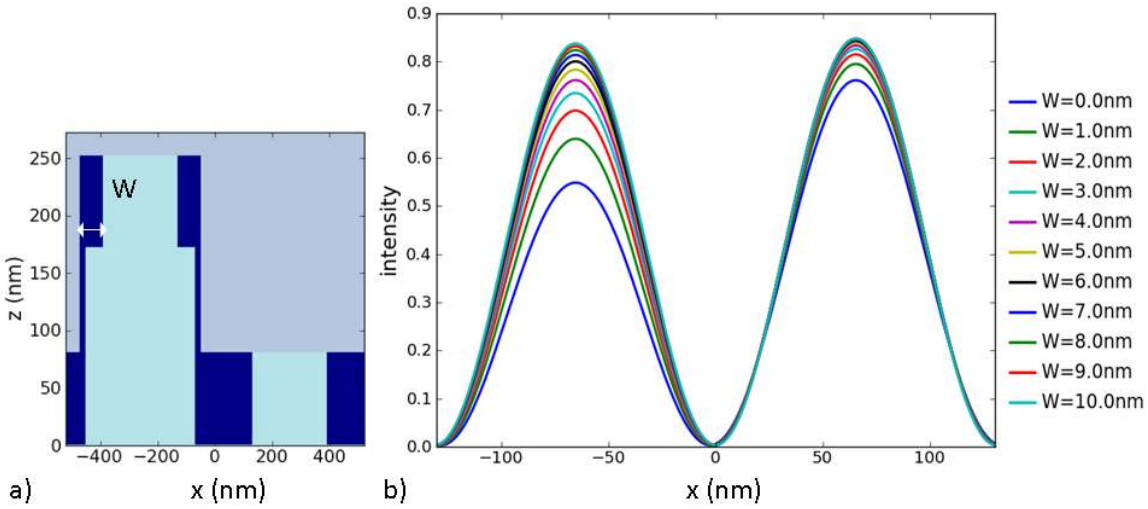

Figure 9: Sidewall Chrome Alternating Aperture Mask (SCAAM) utilizes a) chrome with width *W* on the shifted space in order to b) alleviate intensity imbalance with an optimum *W*=10 nm.

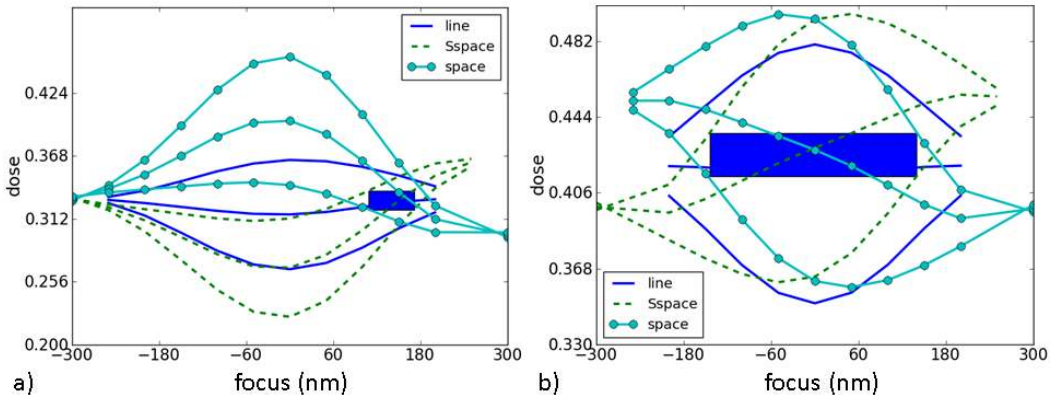

Figure 10: UDOF (shown as blue rectangle) of line, space, and shifted space of 130 nm pitch, 65 nm line, at 1.2NA is only a) 62 nm for an AltPSM and is increased to b) 283 nm for a SCAAM

Thick mask effects have resulted in a trend towards thinner mask layers with thicknesses below the imaging wavelength. Such constraints on masking layers lead to a narrow choice of materials that possess appropriate complex optical constants (n and k) and places tight demands on thickness control over large substrate areas. Additionally, it becomes more difficult to control attenuation and phase independently as can be done with a multiple layer film stack. A method to control the thick mask impact on the phase content of the diffracted field would allow for thicker stack applications.

1.2.2 Source optimization

Image improvement in microscopy by a central obscuration was first noted by Abbe in 1873 [91], and mathematically formulated by Porter in 1906 [92]. A central obscuration was implemented in lithography systems as annular illumination in the late 1980s [93]–[95]. This off-axis illumination (OAI) enhances the resolution by changing the direction of light impinging on the mask [96]. As shown in Figure 11, if on-axis illumination allows the objective lens to capture the 0 and ±1 orders, off-axis illumination with the angle to place the +1 order in the center of the objective lens would also allow the capture of the +2 order [97]. If the mask feature sizes were too small to be resolved

with on-axis illumination such that the ±1 orders were just outside the objective lens, OAI would be able to bring one of the first orders inside the lens, enhancing the resolution of the system, since only one of the 1st diffraction orders is needed to contribute to interference.

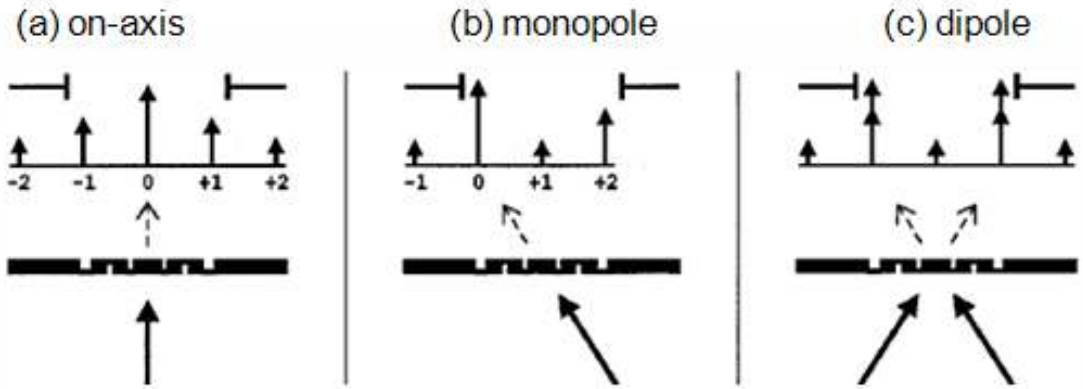

Figure 11: OAI allows for double resolution as well as improved depth of focus

Theoretically, off-axis illumination allows for twice the resolution, yet OAI is also used to enhance the image quality. Figure 11c shows that with two poles of off-axis illumination, not only will more orders be captured which gives better modulation, but the orders within the objective lens will be symmetric. A symmetric source allows the image to become more stable through focus due to the identical defocus aberration obtained by orders with the same optical path length [98]. Source symmetry also prevents pattern placement error when out of focus. In order to maintain symmetry, often a quadrant of the source is optimized and then mirrored into the other 3 quadrants [99].

Many OAI schemes have been thoroughly evaluated and are depicted in Figure 12: a) conventional b) annular [93] c) monopole [100] d) dipole [100]–[102] e) quadrupole [103]–[106] and f) quasar [107]. These illumination schemes can be created by apertures, pixilated filters [108], beam splitters [109], or conical lenses. In order to preserve the amount of intensity reaching the wafer, diffractive optical elements can be

used [110]. Freeform illumination developed by ASML allows these schemes to be created by an array of micro mirrors [111]. Certain illumination schemes are suited for particular mask patterns due to the spectral content of the layout. For example, for 1D vertical lines and spaces in a binary mask, an X-oriented dipole source has been shown to be ideal, depicted in Figure 12d. A 2D array of contacts, which have dense spatial content in both x and y directions, is best imaged with four poles, such as quadrupole or quasar, depicted in Figure 12e and 12f.

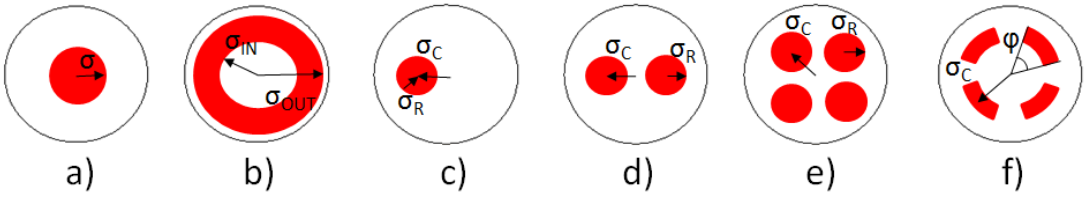

Figure 12: Example illumination schemes are shown with parametric inner, outer, radius, and center σ: a) conventional b) annular c) monopole d) dipole e) quadrupole f) quasar

The quality of the image strongly depends on the illumination source. For example, if dense 1D vertical lines are imaged with a vertical dipole, only the 0^{th} diffraction order is collected and there is no interference to create modulation. It is important to note that the optimized source depends strongly on the mask definition due to degeneracy. As previously mentioned, a dipole source is ideal for a binary mask of 1D lines because the 1^{st} order from each pole overlaps with the 0^{th} order from the other pole, resulting in an optimized depth of focus due to the symmetric intensity in the objective lens. However, when using an alternating PSM, the amplitude of the 0^{th} order is zero (see Figure 7) and the ideal source to use is on axis so that the ±1 orders are symmetric within the objective lens. As shown in Figure 13, these different mask/source combinations both result in a 1D image.

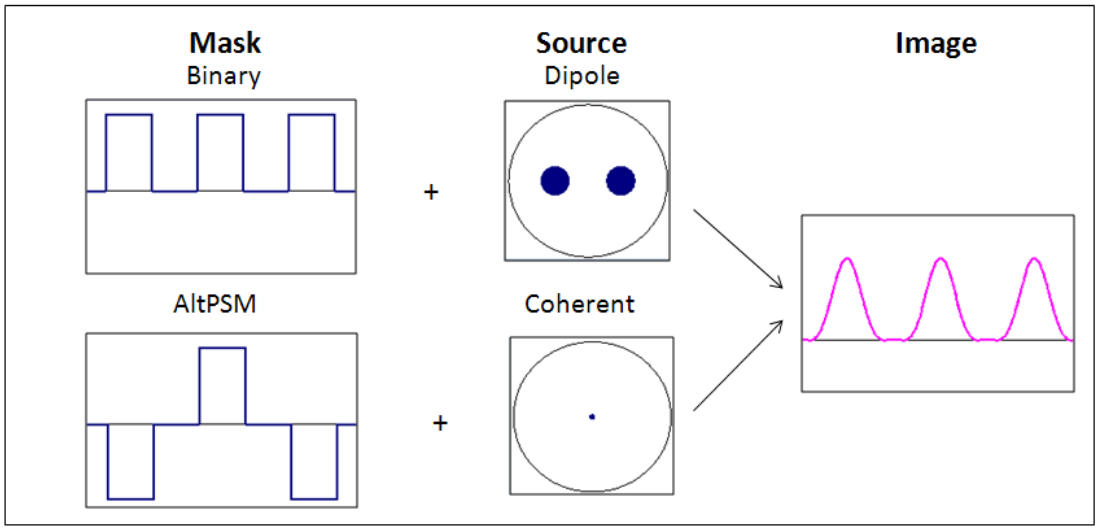

Figure 13: Multiple mask/source combinations can give identical images

There are four primary methods for source shape optimization; parametric, archel, contour, and pixel [112]. A source's quadrant under each optimization method is shown in Figure 14 [112]. Optimization metrics are typically the contrast, EL, DOF, ILS, MEEF, or some combination. The possible parametric sigma settings (σ, σ_{IN}, σ_{OUT}, σ_C, σ_R) and opening angle (φ), are depicted in Figure 12. The advantage of parametric optimization is the reduced number of optimization parameters. However, the parametric source shapes are not tied to the properties of optical equations, thus the optimization becomes highly non-linear. Also, since the simple geometric shapes do not cover all possible solutions, it may not contain the best optimum in the parameter space [112]. In contour optimization, a continuous shape representing one quadrant of the source is varied, using the coordinates of curve segments as parameters. In pixel-based optimization, the source is divided into discrete pixels, each of which can be optimized for a grey-level intensity [113], [114]. This optimization method provides the most degrees of freedom, but with the cost of the highest computational complexity. In archel optimization, each diffraction order is identified within the pupil plane, and a unit circle

(σ=1) is drawn around it. Regions of two-beam interference are those which are contained within two circles thus are included in the optimized source [98]. Archel optimization of a 1D binary mask with a pitch smaller than the coherent resolution limit would select dipole regions.

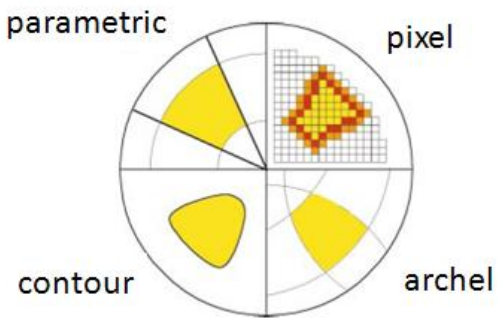

Figure 14: Four methods of source optimization

Source optimization for one target pitch is straightforward. However, the improvement by OAI on a dense pitch can come at the expense of pitches with lower frequencies, referred to as "forbidden pitches" [115]. Assist features can be added to increase the process latitude of sparse pitches that suffer degraded DOF due to OAI [116]. A customized illumination aperture made from combining the optimized illumination shapes for several pitches has been used to enhance UDOF for 1D through pitch features [117]. However, the problem gets increasingly difficult with increasing mask complexity, such as 2D features. The task of optimizing the system for multiple feature structures gave rise to the field called joint source and mask optimization where the source is simultaneously optimized with the mask in order to increase pattern fidelity.

1.2.3 Source and Mask Optimization

Resolution enhancement techniques originated with OPC, which optimizes the mask for a given source. Source optimization for a given mask has been useful to determine the ideal source for a fixed mask. The next realm of RET is joint source mask

optimization (SMO), which allows for the improvement in image quality for arbitrary two directional patterns with degrees of freedom in both mask and source.

In contrast to a direct problem which attempts to predict the response of a system, an inverse problem can be defined as finding the required inputs for a given response [118]. For a medical imaging application, this is reconstructing the three dimensional brain using two dimensional raman scattering data [119]. For lithography, this is calculating the required source and mask given a target image. The Hadamard definition of a well-posed problem is one in which the solution is unique and depends continuously on the input parameters [120]. In nonlinear optical systems, there exists degeneracy where several combinations of inputs produce the same output, causing its inverse problem to be an ill-posed problem and thus one difficult to solve.

SMO represents the simultaneous adjustment of lithographic mask and source parameters in order to optimize the image quality. Gau *et al.* proposed the archel method, which divides the source into regions with the same collected diffraction orders, and then selects the source regions based on an imaging quality metric [121]. Rosenbluth *et al.* utilized this method to solve for both an ideal source and mask [97]. Their global optimization algorithm varied the amplitude of these regions and compared it to the desired aerial image. After determining the ideal amplitude of diffraction orders, the algorithm would calculate mask shapes to produce these diffraction orders. A major advantage of their optimization method is that it does not require initial conditions. Any constraints or starting points limit the solution space that an optimizer sees, so by eliminating the need for initial conditions, the solution can be considered more of a global optimum than a local optimum.

The solutions were evaluated by calculating the process window as the integrated area under the curve of depth of focus versus exposure latitude, measured in %-µm. Figure 15 shows the resulting mask shapes with the target layout of a capacitor pattern [97]. Rectangles (130 nm x 247 nm) have a 260 nm horizontal period and a 390 nm vertical period. Mask pattern is chromeless: black represents a 0º phase shift and white represents an 180º phase shift, where there is a transmission of 1 through every feature. Note that this unintuitive solution contains closed mask shapes corresponding to the locations between closed target features, indicating that an edge-adjusting OPC routine could not converge to this pattern. The optimized source pattern and aerial image simulation are shown in Figure 15c and d, where the dotted regions indicate high intensity.

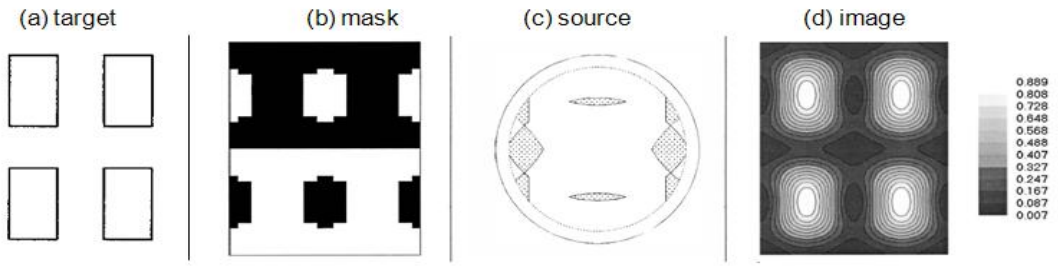

Figure 15: (a) Target layout (b) Optimized mask features in chromeless PSM (black represents 180º phase shift) (c) Optimized source map where dotted regions indicate bright fields. (d) Aerial image in PROLITH™

The simulated process window from their global optimization was 45%-µm, versus only a 7%-µm for conventional optimization (annular illumination and OPC). Source and mask solutions were experimentally verified revealing a clear advantage by the global optimization to increase process latitude. Their algorithm was also applied to alternate technologies, such as AltPSM and grey scale sources [122].

The method to solve the inverse problem in lithography can also mean solving the direct problem iteratively, such as exploring the parameter space with a heuristic search algorithm. For example, inverse lithography and optical proximity correction calculate the image after each pixel flip/edge movement [123], [124]. The objective function is re-calculated during each iteration in order to drive the simulated image towards the target image [125]. Pixilated inverse lithography is used to insert model-based SRAFs [126]–[131]. Iterative solutions like this depend strongly on the initial conditions and can be computationally expensive. Socha *et al.* developed the interfering mapping lithography (IML) method which introduces model-based assist features in order to improve contact hole imaging. The IML method can be described with coherent light as building a Fresnel lens on the mask, and the assist features are placed where the electric field amplitude of a small contact hole is greater than 0, in order to provide constructive interference. The assist feature placement for partially coherent illumination was determined by convolving the mask with a series of kernels and finding the areas with a maximum in electric field. This method of optimization is a series of calculations, thus is not iterative, so can be computationally fast [132]. In another method, the mask is optimized in the frequency domain then converted into a CPL mask, resulting in double the contrast of an AttPSM [133]. Poonawala and Milanfar reduced the mask optimization problem to the steepest descent search of a continuous analytic gradient function [134]. The limitations to this inverse problem formulation include the inability to employ complex models, such as mask topography, since the algorithm requires an analytic representation of the problem.

1.3 Problem statement and approach

As features are pushed below the exposure wavelength, phase errors shift the best focus of each pitch differently. The resulting range in BF, or ΔBF shown in Figure 16, can degrade the UDOF over many pitches. Mask optimization controls the amplitude of diffraction orders and source optimization controls the placement of diffraction orders in the lens pupil, but there is inadequate control over phase.

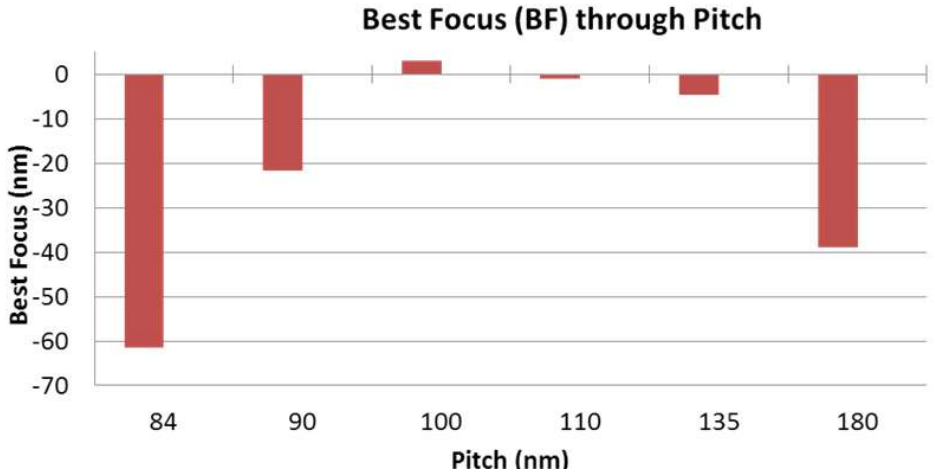

Figure 16: Experimental BF of 45 nm line through pitch for 1% TaSiON AttPSM has a ΔBF of 64 nm

Simulations shown in Figure 17 and 18 illustrate the attempt of mask and source parameters to correct this ΔBF. The sigma settings, σ_C and σ_R, of a quadrupole illuminator are varied while simultaneously adjusting the mask biases to print both the 84 nm and 135 nm pitch. At each illuminator combination, the DOF and BF of each pitch is measured in order to calculate ΔBF and the UDOF. Increasing the σ_R and/or the σ_C does decrease the ΔBF, but with a detrimental effect on individual DOF, which results in a degraded UDOF.

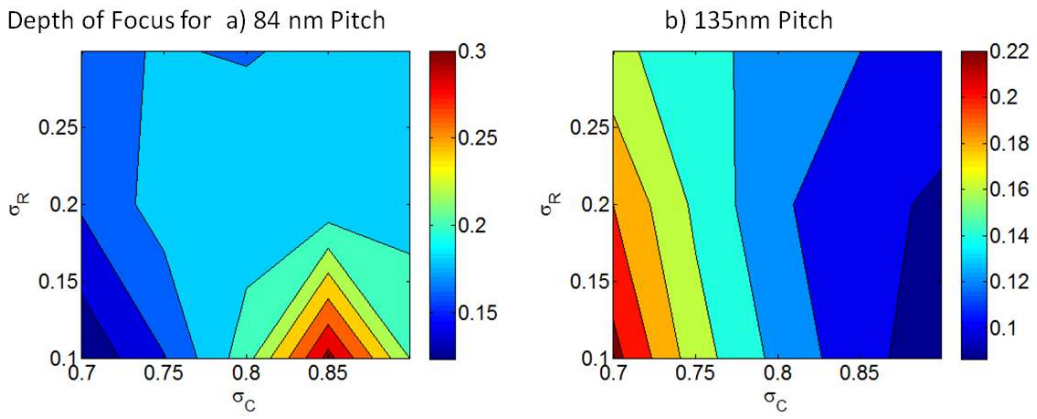

Figure 17: Simulated depth of focus for a) 84 nm pitch and b) 90 nm pitch as a function of illuminator sigma settings

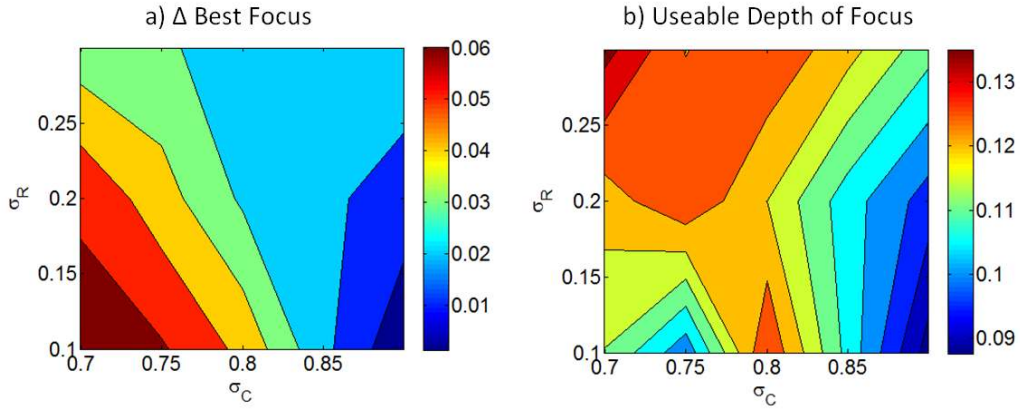

Figure 18: Simulated a) ΔBF and b) UDOF between 84 and 135 nm pitches as a function of the illuminator sigma settings. The σ_C/σ_R values with the lowest ΔBF don't result in the highest UDOF due to degraded individual DOF

A method to decrease the ΔBF while maintaining the individual DOF is needed to obtain the optimal UDOF. Since mask and source parameters are unable to provide the desired phase manipulation, optimization parameters in an alternate domain must be explored in order to truly extend the capability of a lithography system. This correction can be carried out in a conjugate plane of the mask, namely the objective lens pupil of a Köhler illumination projection system. Although the concept of pupil wavefront control has been deliberated for decades [135]–[137], benefits have not yet been able to outweigh detrimental effects to imaging [138]. Recent advances in mechanical actuation and measurement allows for the fine control of the pupil wavefront on the order of a few

milliwaves [139]. Earlier work has shown process window improvement for one directional AttPSM patterns in simulation [140], [141] and experiment [142], [143] by using pupil phase filtering. The work presented here extends this work of one directional patterns to more complex two directional features as well as to thicker phase shift masks on several mask types.

2. BACKGROUND

Here, the fundamental imaging equations are presented in order to understand the impact of the lens pupil domain. A description of each aberration and their effect on the image is included. Ray-intercept, wavefront expressions and a mathematical formulation for aberrations are introduced. Finally, a review of pupil filtering is presented.

2.1 Image formation

2.1.1 Imaging equations

In 1690, Christiaan Huygens published a method of optical analysis which assumes each point in a wavefront becomes the source of a propagating spherical wave [144]. In 1816, Augustin-Jean Fresnel combined the Huygens theory with his own theory of interference to explain diffraction; the phenomena that occurs when light encounters an obstacle [145]. The intensity distribution due to diffraction is dependent on several factors, including the shape of the obstacle, the wavelength of light, its coherence, and the propagation distance. At large propagation distances, Fresnel's diffraction equations can be simplified into Fraunhofer diffraction, named in honor of Joseph von Fraunhofer [146]. The Fraunhofer diffraction integral represents the amplitude through a circular aperture of radius $\sqrt{(u^2+v^2)}$ observed at a distance z.

$$A(x,y) \propto \iint_{Aperture} A(u,v) e^{-i\frac{2\pi}{\lambda z}(ux+vy)} du dv \tag{8}$$

This integral can be formulated as a Fourier transform, defined in Equation 9.

$$A(x) = \int_{-\infty}^{\infty} F(u) e^{-2\pi i u x} du \tag{9}$$

The image through a lithography system can be approximated using the Kirchhoff assumption, where the amplitude at a binary mask is simply a periodic step function [147]. Using Gaskill's notation for this 1D example, a rect(x) function is defined as an even rectangular pulse [148].

$$rect\left(\frac{x}{b}\right) = \begin{cases} 1, & \frac{-b}{2} \leq x \leq \frac{b}{2} \\ 0, & else \end{cases} \tag{10}$$

In order to produce a periodic chain, the comb(x) function is used, which is defined as a train of delta dirac (δ) functions.

$$comb\left(\frac{x}{b}\right) = |b| \sum_{n=-\infty}^{\infty} \delta(x - nb) \tag{11}$$

$$\delta(x - x_0) = \begin{cases} \infty, & x = x_0 \\ 0, & else \end{cases} \tag{12}$$

The mask definition, with space s and pitch p, is the convolution (*) of the rect and comb functions.

$$m(x) = rect\left(\frac{x}{s}\right) * \frac{1}{p} comb\left(\frac{x}{p}\right) \tag{13}$$

The diffraction pattern, or the distribution in the frequency domain, is calculated as the Fourier Transform of the mask, where sinc(x)=sin(πx)/πx.

$$M(u) = \mathcal{F}\{m(x)\} = s \cdot sinc(su)comb(pu) = \frac{s}{p} sinc(su) \sum_{n=-\infty}^{\infty} \delta(u - \frac{n}{p}) \tag{14}$$

The objective lens, $P(u)$ acts as a low pass filter, which collects only those diffraction orders with a frequency smaller than the size of the lens; NA=$n$sinθ, or NA/λ in the frequency domain. For a perfect objective lens with no defocus, the transmission is unity and the phase is a constant.

$$P(u) = \begin{cases} 1, & |u| \leq \frac{NA}{\lambda} \\ 0, & else \end{cases} \tag{15}$$

For a numerical aperture that collects only the zero and ±first orders, the distribution in the objective lens is:

$$M(u)P(u) = \frac{s}{p} sinc(su) \sum_{n=-1}^{1} \delta\left(u - \frac{n}{p}\right)$$

$$= \frac{s}{p} sinc(su) \left(\delta\left(u + \frac{1}{p}\right) + \delta(u) + \delta\left(u - \frac{1}{p}\right) \right)$$

$$= \frac{s}{p}\delta(u) + \frac{s}{p} sinc\left(\frac{s}{p}\right) \left(\delta\left(u + \frac{1}{p}\right) + \delta\left(u - \frac{1}{p}\right) \right) \tag{16}$$

The electric field amplitude at the image is calculated as the inverse Fourier Transform of the distribution in the objective lens. The aerial image intensity is defined as the square of the amplitude.

$$A(x) = \mathcal{F}^{-1}\{M(u)P(u)\} \tag{17}$$

$$I(x) = A(x)^2 = \left|\frac{s}{p} + \frac{s}{p} sinc\left(\frac{s}{p}\right) 2\cos\left(2\pi\frac{x}{p}\right)\right|^2 \quad (18)$$

The mask definition and diffraction pattern for an AttPSM, where $\sqrt{T}$ is the background transmittance, is:

$$m(x) = (1 + \sqrt{T}) rect\left(\frac{x}{s}\right) * \frac{1}{p} comb\left(\frac{x}{p}\right) - \sqrt{T} \quad (19)$$

$$M(u) = (1 + \sqrt{T}) s \cdot sinc(su) comb(pu) - \sqrt{T}\delta(u) \quad (20)$$

The mask definition and diffraction pattern for an AltPSM, where *s* is the width of the unetched space and *l=p-s,* is:

$$m(x) = rect\left(\frac{x}{s}\right) * \frac{1}{2p} comb\left(\frac{x}{2p}\right) + rect\left(\frac{x}{l}\right) * \frac{1}{2p} comb\left(\frac{x}{2p}\right) - 1 \quad (21)$$

$$M(u) = s \cdot sinc(su) comb(2pu) + l \cdot sinc(lu) comb(2pu) - \delta(u) \quad (22)$$

The previous formulation assumes spatially coherent imaging that results from an infinitesimally small source point on axis, which provides a plane wave normal to the mask. However, a nonzero source size is more typical for lithography, and it will illuminate the mask at multiple angles. Several models for partial coherent imaging have been used, such as the sum of coherent systems (SOCS) approximation where the source is pixilated into multiple coherent source points. The aerial image becomes the incoherent sum of the coherent images from each source point [149]–[156]. The aerial image calculation can be calculated in either the spatial domain (sparse) or the frequency domain (dense) [157]. The Abbe method operates in the spatial domain; it formulates the overall intensity by calculating the intensity from each source point at a time, and then

summing [158]. In the Hopkin's method, the integration is carried out at the source in the frequency domain. The Hopkins partially coherent imaging equation incorporates a mutual intensity function, $J(u,v)$, which can be physically approximated by the intensity distribution at the condenser aperture. In this formulation, Equation 18 becomes:

$$I(x,y) = \iint \iint T(u',v',u,\mathrm{v})M(u',v')M^*(u,\mathrm{v}) \times e^{2\pi i[(u'-u)\mathrm{x}+(\mathrm{v}'-\mathrm{v}'')y]}du'dv'du''dv'' \quad (23)$$

where the transmission cross coefficient (TCC) is defined by a two dimensional integration of the product of source, pupil and conjugate pupil [159]:

$$T(u',v',u,\mathrm{v}) = \iint J(u,v)P(u+u',v+v')P^*(u+u'',v+v'')dudv \quad (24)$$

The advantage of using this formulation is that for a fixed optical system with a given illumination shape, numerical aperture, and aberration signature, the TCC needs to be calculated only once, and then can be used in multiple calculations with different masks [146]. In this Hopkins model, a small variation of incidence angles allows the polarization, intensity, and phase of diffraction spectrum to be independent of illumination direction. This assumption breaks down for a large variation of incident angles, a high aspect ratio mask features [160] and at high NA [161], [162]. Extending to higher numerical apertures requires vector imaging, which incorporates polarization and thin film interference effects [163]–[166]. For transverse magnetic (TM) polarization, the modulation decreases as the cosine of twice the angle in the resist, which leads to no modulation when the angle in resist is 45º, or an NA of 1.2 with n_{PR}=1.7 [167]. In order to maintain modulation, transverse electric (TE) polarization is used, which is also defined as Y-polarized for vertically oriented features.

2.1.2 Formulation of aberrations

Geometrical or ray optics can be used to design and analyze lens systems by tracing rays governed by Snell's Law. The index of refraction of the media multiplied by the propagation angle is an invariant:

$$n_i sin\theta_i = n_t sin\theta_t \tag{25}$$

Since the transmitted ray is refracted proportional to the sine of the incident ray, the angle of the transmitted ray does not vary linearly with the angle of the incident ray. This means that perfect reconstruction of an object cannot occur by a single spherical surface, and it gets worse as the angles increase. Paraxial quantities, or those close to the optical axis, can be calculated using a small angle approximation that $sin\theta \approx \theta$ [15]. The rays that are calculated with Snell's Law rather than the small angle approximation may not intersect the paraxial focal plane at the paraxial focus point. This distance between the imaged point and paraxial focus point is quantified as an aberration.

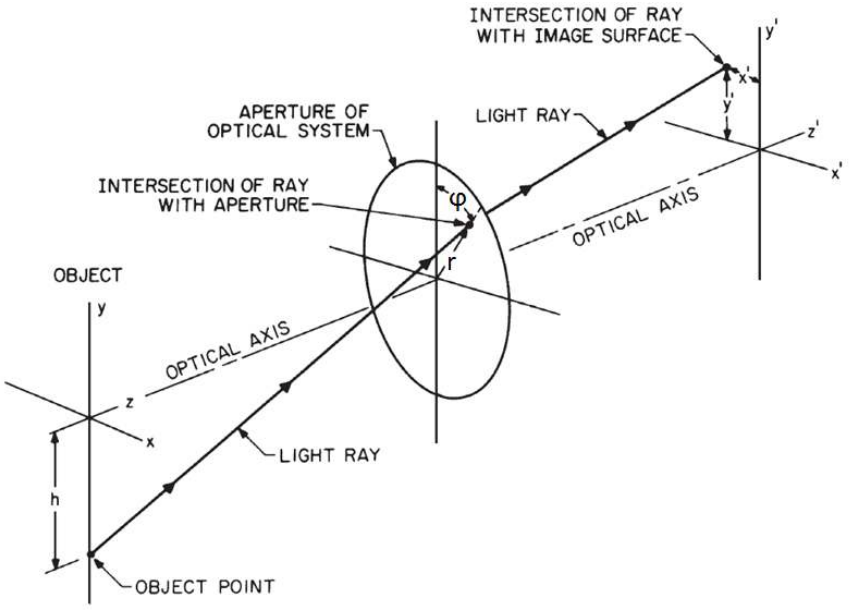

Figure 19: A ray from object point (0,*h*) passes through lens aperture at point with polar coordinates (*r*,*φ*) and intersects image plane at point (x',y')

Assuming an axially symmetric system, the image coordinates can be written in terms of object and aperture coordinates up to the third order, where (r,φ) lies on the aperture with radius $r=\sqrt{(u^2+v^2)}$, and h represents the object height, as depicted in Figure 19 [168].

$$y' = A_1 r\,cos\varphi + A_2 h + B_1 r^3\,cos\varphi + B_2 r^2 h(2 + cos2\varphi)$$

$$+(3B_3 + B_4) r h^2\,cos\varphi + B_5 h^3 \quad (26)$$

$$x' = A_1 r\,sin\varphi + B_1 r^3\,sin\varphi + B_2 r^2 h\,sin2\varphi + (B_3 + B_4) r h^2\,sin\varphi \quad (27)$$

The powers of r and h in the terms with an A coefficient add up to 1, and those with a B coefficient have exponents which add up to 3. These are the 1st order and 3rd order aberrations, respectively. There are no even order terms due to the axial symmetry of the system. The 1st order coefficients are straightforward to decipher; A_1 represents the longitudinal distance between the paraxial focal point and the measured image plane, or defocus, and A_2 represents the magnification. Philipp Ludwig von Seidel solved for the coefficients of the five 3rd order "primary" aberrations as a function of system parameters such as radii, index, and thicknesses. These Seidel aberrations are also referred to as spherical aberration, coma, astigmatism, Petzval, and distortion [169]. The first three of those aberrations are each reviewed in the following discussion as if it were the only aberration present; however, note that in reality a combination of aberrations will likely be present.

2.1.3 Primary aberrations

Spherical aberration, B_1, depends only on the aperture coordinates, not the object coordinate. It can be described as the variation in focal point as a function of aperture. Higher diffraction orders pass through the aperture at higher radius values, resulting in a

spatial frequency dependent focal point. As the radius in the aperture increases, the deviation between focal point and paraxial image plane increases. An exaggerated diagram is shown in Figure 20. Spherical aberration can be measured along the propagation axis (AB in the Figure 20), called longitudinal spherical aberration. Transverse aberration is measured in the vertical direction, from the optical axis to the intersection of the ray (AC in Figure 20). Positive spherical aberration, depicted in Figure 20, results in a focal point before the paraxial image point, whereas negative spherical aberration results in a focal point after the paraxial image point [168].

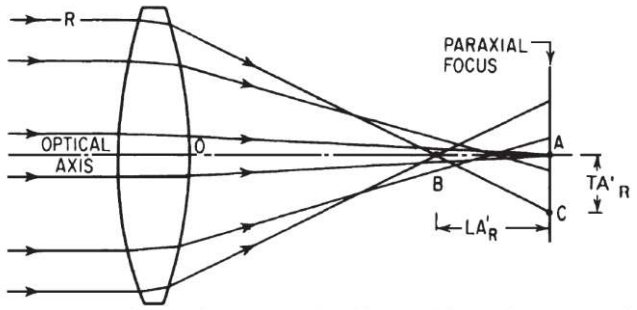

Figure 20: Diagram representing positive spherical aberration; rays at a large radius in the aperture focus before the paraxial image point. Longitudinal spherical aberration of ray R is depicted by AB, and transverse spherical aberration is depicted by AC.

Coma can be described as the variation of magnification as a function of aperture. An optical system suffering from coma will focus the rays coming through the edge of the aperture at a higher height than those closer to the optical axis, as shown in Figure 21 [168]. The differing ray height is proportional to the object height, thus an on-axis point (h= 0) experiences no coma. This phenomenon results in a point source being imaged as a comet, thus the namesake of the aberration.

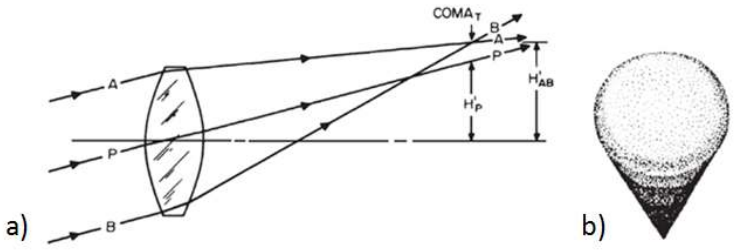

Figure 21: (a) Transverse coma is measured as the difference in ray height from rays through the edge of the aperture versus a ray through the center of the aperture for an off-axis object point. (b) The shape of a point source is imaged as a comet.

Astigmatism can be described as the difference in focal point for tangential and sagittal rays. For an off-axis object point along the y axis, the tangential fan is those rays that are parallel to the y axis. The sagittal fan is those rays that are perpendicular to the y axis which also includes the ray which goes through the center of the aperture. In a system with astigmatism, the focal point of the tangential rays is different than the focal point of the sagittal fan, as shown in Figure 22 [168]. Instead of a point, the image of a point source for each ray fan becomes a line image which lies in the perpendicular plane. In between these two foci, the image of the point source becomes elliptical. Similar to coma, due to the symmetry along the optical axis, there is no astigmatism for an on-axis object point. As the height of the off-axis object increases, the astigmatism increases.

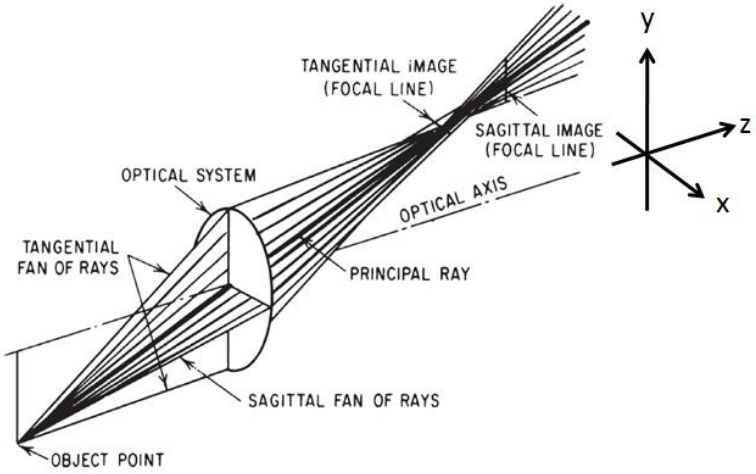

Figure 22: Astigmatism is caused by the variation between a tangential and sagittal fan of rays.

2.1.4 Zernike polynomials

The previous discussion has quantified aberrations using their measured ray heights at the paraxial image plane. Another way to quantify aberrations is to measure the difference between the wavefront leaving the optical system and the ideal spherical wavefront centered on the paraxial focal point, as shown in Figure 23 [168]. This optical path difference (OPD) is defined as the geometrical distance multiplied by the refractive index of the media. The OPD can be measured at each aperture radius to construct a three dimensional (3D) wavefront deformation. The OPD is related to the transverse aberration by a derivative; the OPD for a given ray is the area under the ray intercept plot between the center point and the ray.

$$y' = TA_y = \frac{z_2}{n}\frac{\partial OPD}{\partial y} \tag{28}$$

The OPD wavefront polynomial, shown below, is found by integrating Equation 26 and using the relationship $\partial s/\partial y \propto \cos\varphi$ [168].

$$OPD = A'_1 r^2 + A'_2 rh\cos\varphi + B'_1 r^4 + B'_2 r^3 h\cos\varphi$$

$$+B'_3 r^2 h^2 \cos^2\varphi + B'_4 r^2 h^2 \tag{29}$$

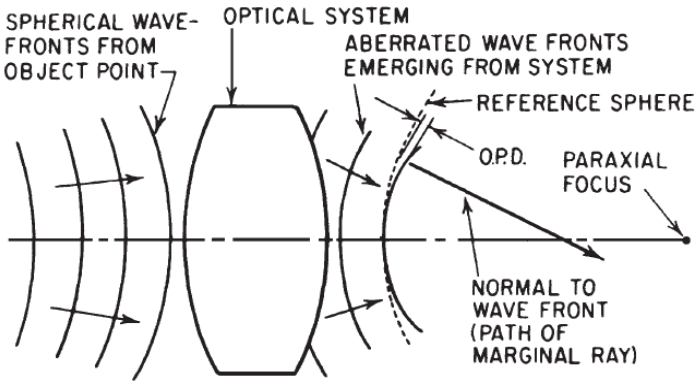

Figure 23: OPD of a wavefront can be calculated as the difference between the path lengths of the marginal and axial ray between the object and image point.

A common representation of the wavefront OPD uses the Zernike polynomials [170]. The Zernike polynomials mathematically describe 3D wavefronts, but since they are defined to be orthogonal over the unit circle, they do not have a 1:1 correspondence to the optically-derived Seidel polynomials. Their orthogonality allows easy decomposition from measured wavefront data. Another advantage of using orthonormal polynomials is that each coefficient represents the standard deviation of its aberration term, and the coefficients are not affected by the addition of other terms, such as a defocus aberration [170]. Zernike polynomials represent balanced aberrations such that an aberration of a certain order is balanced with aberrations of lower order to minimize its variance [170]. The Zernike coefficients of Equation 30 are in terms of the aperture radius, r, and the azimuthal angle, φ [171]. The first 21 Zernike polynomials are depicted in Figure 24 [172].

$$\mathrm{A_{nm}} = Z_n^m(r,\varphi) = \begin{cases} R_n^m(r)\cos m\varphi; & m \geq 0 \\ R_n^m(r)\sin m\varphi; & m < 0 \end{cases} \tag{30}$$

The radial function is defined as

$$R_n^m(r) = \sum_{k=0}^{(n-m)/2} \frac{(-1)^k (n-k)!}{k!\left(\frac{n+m}{2}-k\right)!\left(\frac{n-m}{2}-k\right)!} r^{n-2k} \tag{31}$$

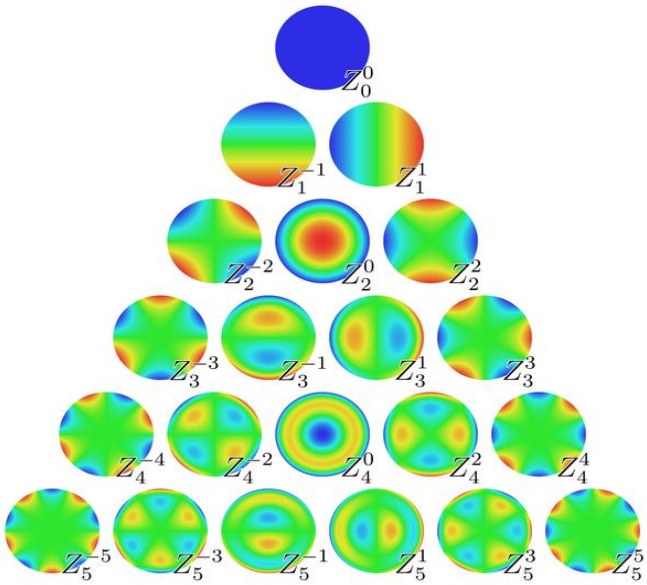

Figure 24: Z_n^m /A_{nm} Zernike polynomials can be combined to mathematically represent an aberrated wavefront

A power series representation of an aberrated wavefront can thus be written in polar coordinates in either the Seidel (S_{kl}) and the Zernike formulation, shown below.

$$\Phi(r,\varphi) = S_{kl}\left(\frac{r}{R}\right)^k \cos^l \varphi \tag{32}$$

$$\Phi(r,\varphi) = A_{00} + \sum_{n=1}^{\infty}\sum_{m=0}^{n} \frac{A_{nm}\left(\frac{r}{R},\varphi\right)}{\sqrt{(1+\delta_{m0})}} \quad n \geq m, \;\; n-m = even \tag{33}$$

The Zernike polynomials can be converted into Seidel polynomials using a mathematical matrix derived by Tyson [171].

$$\mathrm{S_{kl}} = \sum_{n=0}^{\infty}\sum_{m=0}^{n} a_{klnm} A_{nm} \tag{34}$$

If the following conditions are not met: k-l = even, n-m = even, n-k = even, m-l = even, k-m = even, and $n \geq k \geq m \geq$ l, then a_{klnm}= 0. If those conditions are met then a_{klnm} is defined by:

$$a_{klnm} = \begin{cases} 1, \ n,k,m,l = 1 \\ \dfrac{(-1)^{\frac{n-k}{2}}\left(\frac{n+k}{2}\right)!}{\sqrt{(1+\delta_{m0})}\left(\frac{n-k}{2}\right)!\left(\frac{k+m}{2}\right)!\left(\frac{k-m}{2}\right)!} \dfrac{(-1)^{\frac{m-l}{2}}2^l m\left(\frac{m+l}{2}-1\right)!}{(m-l)\left(\frac{m-l}{2}-1\right)!\, l!}, & m = l \\ \dfrac{(-1)^{\frac{n-k}{2}}\left(\frac{n+k}{2}\right)!}{\sqrt{(1+\delta_{m0})}\left(\frac{n-k}{2}\right)!\left(\frac{k+m}{2}\right)!\left(\frac{k-m}{2}\right)!} \dfrac{(-1)^{\frac{m-l}{2}}2^l m\left(\frac{m+l}{2}-1\right)!}{(m-l)\left(\frac{m-l}{2}-1\right)!\, l!}, & m \neq l \end{cases} \quad (35)$$

Figure 25 shows representations of the difference between the ideal wavefront and the measured wavefront due to a particular aberration, or the 3D OPD [173]. The spherical aberration shown in Figure 25b has a negative r^2 term in it that balances the aberration with defocus as well as piston (a constant value which represents the mean phase of the wavefront). Including the defocus term redefines the image plane to be halfway between the paraxial and marginal focus planes, in order to minimize the OPD variance and resulting spot size.

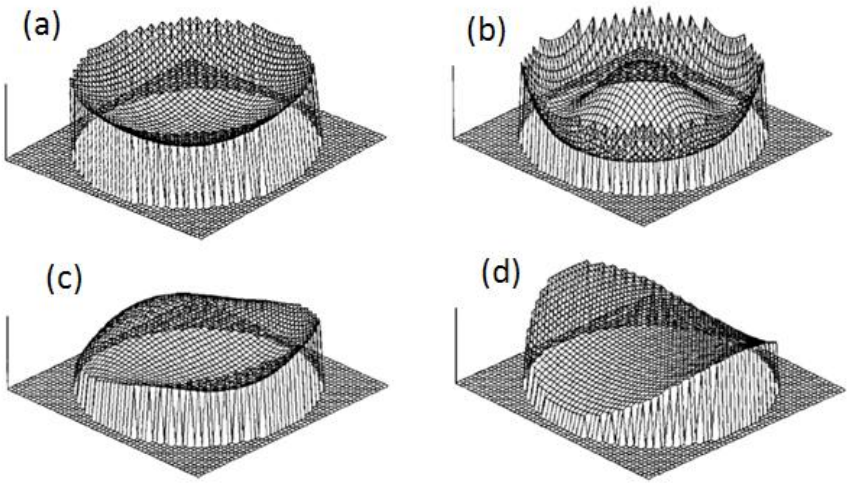

Figure 25: 3D OPD due to (a) defocus (b) balanced spherical (c) coma and (d) astigmatism

Several methods of normalization exist. Fringe Zernike polynomials are normalized to the edge of the aperture, so that at r=1, the polynomial is 1. Thus, for a coefficient of z_n=1, the phase at the edge of the pupil would be 2π radians or 360°. Wavefront polynomials for several aberrations with their corresponding Fringe Zernike

coefficients are tabulated in Table 1 [173], which is the convention that will be used in this dissertation. To model the effect from an aberration, the phase of the pupil function contains the wavefront aberration function, thus Equation 15 becomes

$$P(r,\varphi) = \begin{cases} e^{i\frac{2\pi}{\lambda}W(r,\varphi)}, & |r| \le \frac{NA}{\lambda} \\ 0, & else \end{cases} \tag{36}$$

Table 1: Wavefront aberrations and Fringe Zernike coefficient

Aberration	**Zernike Coefficient (z_n)**	**W(r,φ)**
Defocus	z_4	$2r^2-1$
Primary Astigmatism	z_5	$r^2\cos 2\varphi$
Primary Coma	z_8	$(3r^3-2r)\cos\varphi$
Primary Spherical	z_9	$6r^4-6r^2+1$
Secondary Spherical	z_{16}	$20r^6-30r^4+12r^2-1$
Tertiary Spherical	z_{25}	$70r^8-140r^6+90r^4-20r^2+1$

2.1.5 Aberration control

In order for projection lithography to be diffraction limited, the accepted convention is that the optical system must not produce more than one quarter-wavelength (λ/4) wavefront OPD, known as the Rayleigh rule [173]. As the wavelength of light has scaled, this rule has placed more stringent demands on the optical elements and overall system design. Methods have been developed in order to limit and control aberrations, such as aspheric elements and advances in lens manufacturing that use phase measurement interferometry to dictate lens polishing and positioning [174]. Optical designs have turned to catadioptric systems, which use mirrors to reduce the inherent aberrations in refractive elements. Often, lens aberrations are measured as phase error in the pupil plane [175], and then fit to Zernike coefficients to allow decomposition into components that can be used for analysis and correction [176]. Pupil plane engineering

techniques have also been proposed, such as modulating the illumination by a phase plate with periodic steps [177], using a grey-level amplitude filter to compensate for transmission errors [178], or pneumatic actuation of a deformable pupil mirror [179].

2.2 Pupil filtering

Since aberrations have a significant impact on image quality, it follows that the phase of the pupil plane could be used as an additional optimization parameter to enhance imaging [180]. Pupil filtering was first proposed by Tsujiuchi in 1957, who wrote "If *w(x)* is the aberration function that represents the departure of the wave front from the Gaussian reference sphere, the ideal compensation procedure might be to place in the exit pupil a phase plate having complex amplitude transmittance *exp[-jw(x)]"* [181]. Since then, many variations of amplitude and phase pupil filters have been developed to enhance particular imaging scenarios.

2.2.1 Amplitude pupil filtering

Fukuda *et al.* achieved improved resolution and DOF by incorporating an amplitude filter at the lens pupil. The pupil transmission function was found to be proportional to $\cos(r^2)e^{2\pi i r2}$ by considering an amplitude superposition of images with shifted focal planes [135]. Fukuda *et al.* also proposed a pupil filter to be used with annular illumination which has 60% transmission from the center to the edge of the annulus, and 100% transmission outside the annulus. This allows the zero and first orders to have similar amplitudes at low spatial frequencies, and it decreases the relative amplitude of the zero order for high spatial frequencies [136]. Horiuchi *et al.* achieved enhanced resolution with a similar amplitude pupil filter for oblique illumination but with three optimized levels of transmittance [182]. An apodization pupil function that

increases DOF was derived by maximizing the area under the PSF's central peak in both the radial and axial (out of focus) directions. The tradeoff becomes the resolution; either the width of the PSF increases or the sidelobe energy increases [183]. Kang *et al.* has shown that spatial frequency filtering can be achieved in the pellicle plane, which is sufficiently far enough from the mask to be within the Fraunhofer region [184]. It has also been proposed to incorporate the pellicle plane filter into the mask making process [185].

Smith *et al.* found that a square illumination source and a circular objective pupil leads to improved resolution, since a square illumination source allows for more of the first orders to be collected than from a circular illumination source with the same width [186]. A square annulus illuminator allows a larger area of overlap between the zero and first orders, also resulting in improved DOF [187]. A square aperture can also result in improved DOF, since the first minima of the square pupil's sinc-shaped PSF is less than the first minima of the circular pupil's bessel-shaped PSF. The change in the modulation transfer function (MTF), which represents the achievable modulation as a function of spatial frequency, is shown in Figure 26, where the spatial frequency is normalized to the coherent cutoff frequency. The cutoff frequency for the square aperture is smaller, shown as the x-intercept of the 'In focus' (blue) series at 26, due to the smaller size of the square aperture inscribed in the circular pupil. However, the square aperture provides higher modulation for certain spatial frequencies when out of focus by $\delta = \lambda$ nm, shown as the higher y-value at a frequency of 1 in the 'Defocus 193nm' (red) series.

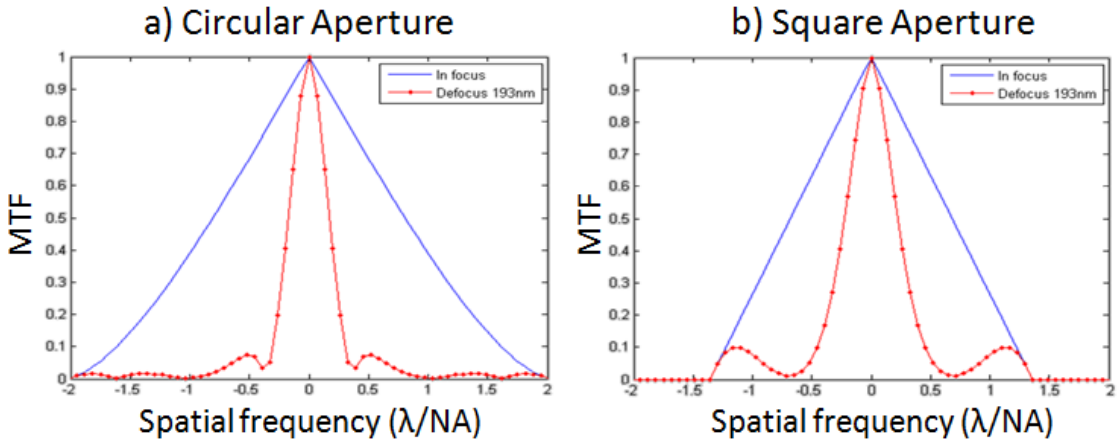

Figure 26: Modulation transfer function (MTF) for a) circular aperture and b) square aperture, which achieves improved modulation out of focus

A pupil filter used with a binary mask can achieve a similar image as a phase shift mask that was shown in Figure 7. The 0^{th} diffraction order can be removed through either an aperture with a center transmission of 0% [188], or deflection [189]. This transforms the frequency spectrum into that of a chromeless phase shift mask, and thus achieves frequency doubling. Instead of resolving each mask feature, each mask edge is printed.

2.2.2 Phase pupil filtering

Von Bünau *et al.* used non-radially symmetric phase pupil filters to image specific parts of a mask, such as horizontal or vertical edges [137]. Phase pupil filters with cubic [190] and quartic [191] radial functions have been proposed to enhance DOF. Phase pupil filtering has also been used in the field of microscopy, specifically phase contrast microscopy, where a phase plate is placed after the back-focal plane of the objective lens to induces a 180º shift on the zero order, which allows very thin objects to be imaged [192]–[196].

This dissertation proposes that phase pupil filtering could be used to compensate for the pitch dependent mask topography effect, as shown in Figure 16. Phase pupil filtering has yet to be used in high volume manufacturing due to the issues associated

with user pupil access. With the current and future semiconductor technology having mask features on the order of the exposing wavelength, mask topography induced phase errors could justify the need for pupil filtering if adverse effects can be overcome. Experimental implementation of pupil filtering is carried out without user pupil access using the ASML Image Tuner application and FlexWave, but could likewise be carried out on a Nikon system using infrared radiation, electric-driven lenses, and deformable mirrors [179], [197], [198]. These systems have been successfully used for thermal aberration control [199]. The form of the compensation filter must be correlated to the subwavelength imaging phenomena, which is examined in the next section.

3. MASK TOPOGRAPHY EFFECTS

In addition to the pitch dependent best focus, additional phenomena have been attributed to mask topography effects, which are reviewed here. Next is a discussion of the rigorous simulation that has been required to predict these phenomena. Finally, pupil plane compensation techniques are reviewed and an effort is made to find the pupil phase fingerprint for successful mask topography compensation.

3.1 Mask topography induced phenomena

Several undesired phenomena have been observed and attributed to mask topography effects. A best focus (BF) offset between dense and isolated features has been observed experimentally [142], an example of which was given in Figure 16. An asymmetric absorber profile has been shown to result in a CD bias between edge features in 2-bar and 5-bar structures [143]. Mask topography effects have also been shown to contribute to a significant part of MEEF, even for binary masks [200]. A mask transmission loss with a thick mask absorber has been observed, due to coupling of the incident light with the electro-magnetic modes of the dielectric cavity. This manifests as an enhancement in the dose-to-size curve for a given pitch and given illumination angle, and can even result in negative MEEF [76]. Experimental data has also shown that thick masks can induce astigmatism, which results in a best focus deviation between horizontal and vertical features [201].

An experimental observation of AltPSMs revealed a CD variation between etched and nonetched spaces, which results in a placement error [202]. This can be attributed to

an intensity imbalance between the spaces since scattered light from the etched feature reduces its transmission [203], [204]. The intensity imbalance can also be explained by effective transmission and phase errors associated with the glass edges, which give rise to a non-zero 0^{th} diffraction order [205]. Another explanation is that residual light transmission through the absorber results in a phase shift between the zero and first diffraction orders [206].

3.2 Rigorous mask modeling

For relatively large mask features, the Kirchhoff approximation can be used, which assumes that each feature at a mask of infinitesimal thickness can be defined by one transmission and one phase value. In this case, no phase errors are induced thus pitch dependent best focus for AttPSM and intensity imbalance for AltPSM does not occur. In order to accurately predict mask topography phenomena, rigorous mask simulations that solve Maxwell's equations are required [207]. Maxwell's equations relate electric charges and currents to electric and magnetic fields. The parameters include the electric field $\vec{E}$, the magnetic field $\vec{H}$, the electric displacement $\vec{D}$, the magnetic induction $\vec{B}$, the current density $\vec{J}$, the electric charge density ρ, the permittivity ε, and the permeability μ [146].

$$\vec{\nabla} \times \vec{E} = -\mu_0 \frac{d\vec{H}}{dt} = -\frac{d\vec{B}}{dt} \tag{37}$$

$$\vec{\nabla} \times \vec{H} = \vec{J} + \frac{d\vec{D}}{dt} \tag{38}$$

$$\nabla \cdot \vec{D} = \rho \tag{39}$$

$$\nabla \cdot \vec{B} = 0 \tag{40}$$

For homogeneous and isotropic media, the relations $\vec{D} = \varepsilon\vec{E}$ and $\vec{B} = \mu\vec{H}$ are valid. Faraday's Law (Equation 37) reveals that a changing magnetic field creates an electric field and Ampere's Law (Equation 38) reveals that a changing electric field gives rise to a magnetic field, thus together they represent how an electromagnetic wave propagates. Gauss' Law, in Equation 39, governs how an electric field is generated from electric charges; from positive to negative charges. Gauss' Law for Magnetism, in Equation 40, reveals that magnetic fields are represented by dipoles that carry no net magnetic charge, rather than singular magnetic sources.

Within a medium where the material properties are a constant, the equations can be simplified to the wave equation. However, solving these coupled equations is particularly difficult at the interface between two media, such as at the absorber edge of the mask feature. Boundary conditions at each interface, shown in the below equations where $\hat{n}$ represents an orthogonal vector to the interface, must be satisfied. Vector imaging equations, such as those derived by Barouch and Yeung [208]–[210], are used to model the lithographic projection system. Multiple computational methods have been developed to simplify and solve these equations, which are reviewed here.

$$\hat{n} \times (\vec{E}_2 - \vec{E}_1) = 0 \tag{41}$$

$$\hat{n} \times (\vec{H}_2 - \vec{H}_1) = \vec{J} \tag{42}$$

$$\hat{n} \times (\vec{D}_2 - \vec{D}_1) = \rho \tag{43}$$

$$\hat{n} \times (\vec{B}_2 - \vec{B}_1) = 0 \tag{44}$$

3.2.1 Finite Difference Time Domain

The Finite Difference Time Domain (FDTD) method uses the Abbe approach to calculate intensity distributions from the incoherent superposition of coherent images obtained for each illumination point [211]. The electric and magnetic field components of Equations 37 and 38 are numerically integrated at staggered discrete space and time coordinates [212]. With the 3 fields for each spatial coordinate from both electric and magnetic fields, there are a total of 6 coupled field components. With an appropriate grid or mesh definition, the Equations 39 and 40 are guaranteed to be satisfied. For a mask feature definition constant in the y direction, the system of equations decouple into 2 cases depending on polarization, TE (E_y, H_x, H_z) and TM (H_y, E_x, E_z) [213]. For the TE case, the EMF components are defined by:

$$\frac{\partial H_x}{\partial t} = \frac{1}{\mu_0}\left(\frac{\partial E_y}{\partial z}\right) \tag{45}$$

$$\frac{\partial H_z}{\partial t} = -\frac{1}{\mu_0}\left(\frac{\partial E_y}{\partial x}\right) \tag{46}$$

$$\frac{\partial E_y}{\partial t} = \frac{1}{\varepsilon_0 \varepsilon}\left(\frac{\partial H_x}{\partial z} - \frac{\partial H_z}{\partial x} - J_y\right) \tag{47}$$

The spatial grid with discretization, Δx, is staggered between the electric and magnetic field components, shown in Figure 27. The discretization in time, Δt, is also staggered; the electric field is sampled at whole time intervals (n±1) and the magnetic field is sampled at half time intervals (n±1/2). With this sampling, the H_x from Equation 45 becomes dependent on H_x from the previous time and E_y from the staggered time and space positions, as shown in Equation 48. Note that the derivatives are replaced with a

simple difference, thus the "finite difference" namesake of the method. The fields are then calculated in an iterative manner.

$$H_x|_{i,j}^{n+\frac{1}{2}} = H_x|_{i,j}^{n-\frac{1}{2}} + \frac{\Delta t}{\mu_0 \Delta x}(E_y|_{i,j+1}^{n} - E_y|_{i,j}^{n}) \tag{48}$$

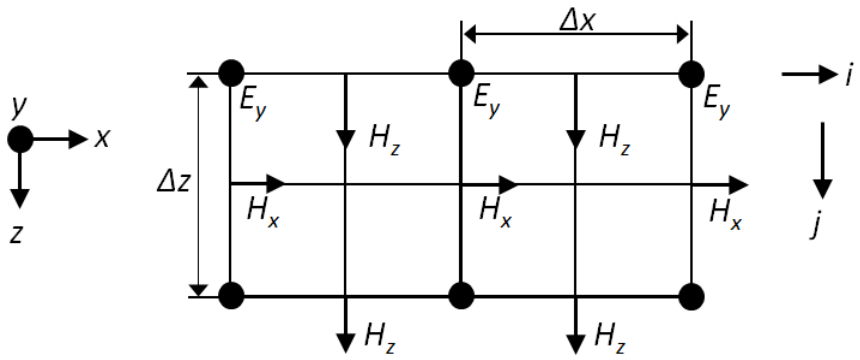

Figure 27: Grid definition and position of TE field vectors for FDTD method

The accuracy of the FDTD solution increases with a decreasing Δx, since the approximation essentially replaces the function with its slope. The accepted convention of more than 15 spatial sampling points per wavelength and a time discretization $\Delta t < \Delta x/c$, where c is the vacuum velocity of light [214]. Since each grid point is dependent on adjacent grid points, the computation of field components at the edge of the staggered grid requires certain boundary conditions to be met. Reflecting boundary conditions set all field components outside the grid to be zero, which is numerically the simplest but may not represent the physical situation. Transparent boundary conditions contain artificially constructed perfectly matched layers which absorb the light and give no back reflection. Periodic boundary conditions connects the edge of the grid on one side to the edge of the grid on the other, which is useful for modeling periodic structures [215].

The FDTD method has a limitation in that it is only stable for a positive permittivity, thus it can fail for materials with a strong absorption. By including additional field quantities, the method can converge for absorbing materials, but it requires more memory and computation time. Methods have been developed to reduce computation time, such as domain decomposition where the fields are calculated in first the vertical then horizontal directions, then summing. The degradation in accuracy of high frequency components are filtered out by the projection optics, giving a good match at the wafer plane [216].

In the Hopkins imaging formulation, diffraction efficiencies are independent of illumination angle. However, this assumption breaks down for subwavelength features, high aspect ratio features and at high NA [160]–[162]. A high Shadow Ratio, the product of the aspect ratio and the sine of the incidence angle, indicates that mask topography effects play a role [217]. In extending FDTD theory to oblique incidence, an assumption of a $2\pi m$ phase difference between left and right boundary points requires no modifications to the field equations. Thus the illumination angles that satisfy $m\lambda = d\sin\theta$, where d is the width of the computation window, can be used [218]. The diffraction spectra is calculated for those points on the grid, and a weighting system can then be used to determine the diffraction efficiencies for all source points [219].

3.2.2 Modal methods

Rigorous coupled-wave analysis (RCWA), which operates in the frequency domain, is based on the approximation of the permittivity function by a truncated Fourier Series. This reduces the mask transmission problem into the solution of an eigenfunction

in discrete Fourier Space [215]. The eigenvalues belong to slices along the full pitch of the computing window, thus the interface boundary conditions are treated approximately due to the truncated Fourier Series. The accuracy of the method increases with the number of terms kept in the Fourier Expansion [220].

The Waveguide method, like RCWA, is based on the expansion of the electric field into a generalized Fourier Series [221]. However, in the Waveguide method, the geometry is divided into thin rectangular slabs with a constant material, thus the permittivity function is exact [222]. Maxwell's equations are first solved within each discrete slab, which is treated as an individual waveguide thus reduces the problem from 3 dimensions to 2, then the fields are matched across the boundaries [223].

3.2.3 Other simulation methods

Although FDTD and RCWA are the most well known, many other solvers have been developed that may be tuned to specific applications. The accuracy of each simulation method has been thoroughly investigated [220], [224], [225]. The Finite Element Method (FEM) is based on eliminating the spatial derivatives from a partial differential equation by approximating the physical geometries with simpler, often triangular, elements in space [226]. The boundary layer model adds an imaginary shape to each feature edge on the thin mask model, where the transmission and width of the shape are tuned to replicate the FDTD spectra obtained from various types and sizes of openings [227]. Another fast mask topography model was developed using a pupil lens aberration to emulate the difference between Kirchhoff and the spectra obtained from the waveguide method [228]. Vector potential model assumes a time-independent system and defines the magnetic field in terms of a vector potential and the electric field in terms of a scalar potential in

order to simplify the problem from a three variable equation into many smaller two-variable equations [229].

The surface integral method represents the scattered fields within each media in terms of unknown currents, J_E and J_H, flowing on the surface enclosing that region. Barouch *et. al.* extends this formulation to the single integral method, where all interior currents due to the electric and magnetic fields are combined into a single effective surface current, J_{EFF} [209]. The single integral equation is shown in Equation 49, where H_{inc} represents the incident magnetic field, r represents the field point, and $A_e^{(1)}$, $A_m^{(1)}$ and $\Phi_m^{(1)}$ represent the external vector and scalar potentials as a function of the effective current, J_{EFF}. This single integral equation can be solved for J_{EFF} using the method of moments [209].

$$0 = H_{inc}(r) + \frac{1}{\mu_0}\nabla \times A_e^{(1)}(r) + j\omega A_m^{(1)}(r) - \nabla\Phi_m^{(1)}(r) \tag{49}$$

3.3 Mask topography phase errors

A rigorous simulation study was completed in order to evaluate the dependence of the mask induced phase error on the absorber parameters *n, k*, and thickness, *t*. The mask induced phase errors were quantified as the ΔBF over 6 pitches; {84, 90, 100, 110, 135}nm with a 1:1 duty ratio so that the amplitude of the first diffraction order was constant through pitch. The AttPSM was illuminated with an XY polarized C-Quad made up of 4 coherent points at σ=0.76 so that the mask was illuminated from only one angle, decreasing the effects of partial coherence. In Figure 28, the ΔBF is plotted as a function

of n and k with a constant transmission, T, defined by Beer's Law. Note that the phase of the light through the absorber is dependent on n and thickness, t.

$$T = e^{\frac{-4\pi tk}{\lambda}} \tag{50}$$

$$Phase\ shift\ (\text{rad}) = t(n-1)\frac{2\pi}{\lambda} \tag{51}$$

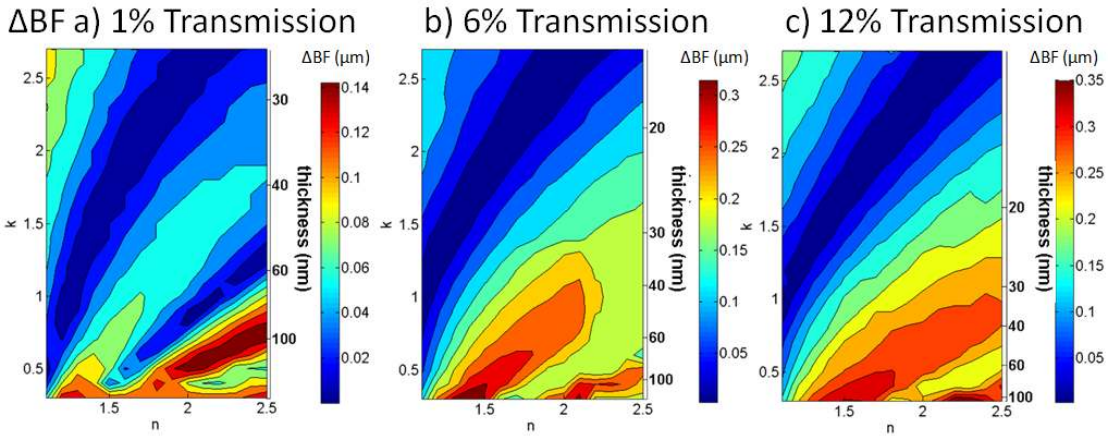

Figure 28: ΔBF as a function of n and k with a transmission of a) 1% b) 6% and c) 12%

The ΔBF tends to be lower with a higher k, which is correlated to a smaller thickness. This agrees with the fact that an ideal Kirchhoff absorber that results in a ΔBF of zero has an infinitesimal thickness. Note the parameters for a MoSi 6% AttPSM are n=2.422 and k=0.586. For a given thickness, the ΔBF tends to be higher for a higher transmission due to the increased background intensity used for interference. For example, with a thickness of 30 nm and an n of 2, the ΔBF for T=1% is 20 nm, and the ΔBF for T=6% is 175 nm, where as the ΔBF for T=12% is 250 nm.

It is evident that even when the amplitude of the diffraction orders are constant and the angle of incident illumination is constant, mask topography treats each pitch differently, resulting in a ΔBF. In the pupil plane, the difference between each pitch is the radial location of the nonzero diffraction orders. Thus, the mask topography effect

could be described as an aberration that varies along the radial component, or equivalently, a radially dependent pupil filter.

3.4 Mask topography compensation

Correction of mask topography by a compensating wavefront has been proposed in order to improve process latitudes [230]. Pupil filtering can now be implemented in semiconductor projection scanners through advancements in mechanical actuation and measurement, allowing for the introduction of small levels of Zernike polynomial aberrations up to z_{64} [139], [231]. Optimization methods have been implemented to iteratively converge on mask, source, and pupil parameters that result in reduced thick mask effects [140], [141]. Maximum Lateral Test Patterns, the inverse Fourier transform of the Zernike polynomials, could also be used to find areas in the layout with a high sensitivity to a certain aberration [232], [233].

In order to arrive at an optimum wavefront to reduce three dimensional (3D) mask topography effects, rigorous simulations were employed with several mask types and imaging conditions. Three masks were evaluated: one directional (1D) lines with a 1% transmitting tantalum silicon-oxi-nitride (TaSiON) layered AttPSM, 1D lines with a Cr film based AltPSM, and two directional (2D) contact holes with a 6% transmitting molybdenum silicon (MoSi) layered AttPSM, the details of which are given later. The illumination conditions were a cross-aligned four-pole (opposed dipoles) for the AttPSM cases and a small circular illuminator shape for the AltPSM case. In order to maximize modulation, all illuminators were XY polarized which allows for transverse electric (TE) interference for both vertical and horizontal orientations [164].

For each case, diffracted fields from the masks for multiple pitches were calculated using the RCWA method, and the phase errors between the collected 0^{th} and 1^{st} diffraction orders were extracted. The phase error as a function of periodicity (pitch) was used as a response output, where the pitch was then correlated to the lens pupil radius. This phase error across the pupil was used to weight individual Zernike polynomial terms and then summed in order to quantify the similarity between each aberration and the thick mask induced phase errors. This quantified sensitivity represents the relative impact that these mask phase errors have on the wafer level metrics correlated to that aberration. For example, a high sensitivity to coma would signify that thick mask effects have a large impact on left-to-right linewidth variation, and a high sensitivity to astigmatism would represent a large impact on horizontal-to-vertical linewidth variation. The resulting sensitivities are shown in Figure 29 for the three cases.

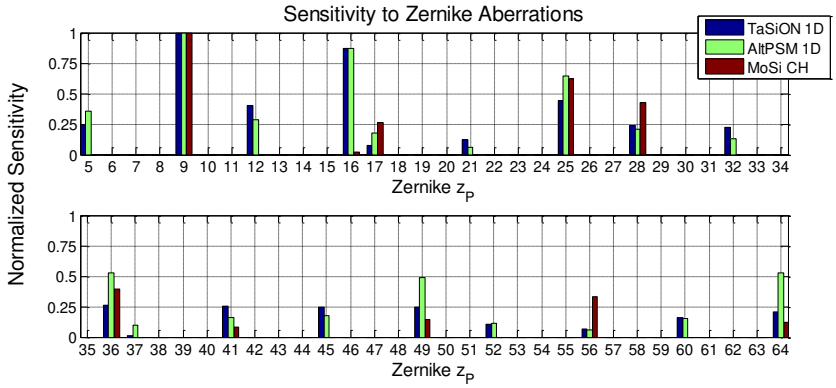

Figure 29: Rigorous mask pupil phase sensitivity to each Zernike aberration for 1D lines on a 1% TaSiON AttPSM, 1D lines on an AltPSM, and contact holes on a 6% MoSi AttPSM. Highest sensitivities are from spherical aberration (z_9, z_{16}, z_{25}, z_{36}, z_{49}, z_{64}).

From these results, it was determined that the 1D lines are sensitive to asymmetrical aberrations such as astigmatism (z_5, z_{12}, z_{21}, z_{32}, z_{45}, z_{60}) since the diffraction orders are distributed only along one axis. Thus, when the mask induced phase error is multiplied by the asymmetric polynomial, there is no sampling along the other

axis. All features are sensitive to X-oriented Tetrafoil (z_{17}, z_{28}, z_{41}, and z_{56}) which is symmetric about the X and Y axis, but has opposite lobes along the 45° axis where the diffraction orders are less distributed. The illumination settings were a Cartesian aligned four pole illuminator (a cross-quadrupole C-Quad design) for the 1D and 2D AttPSM, and a circular small σ illuminator for the AltPSM. If annular illumination was used rather than the C-Quad for the contact holes, the expected sensitivities of non-rotationally symmetric aberrations would be less since the diffraction orders would probe all azimuthal angles.

This exercise revealed spherical aberrations (Fringe Zernike terms z_9, z_{16}, z_{25}, z_{36}, z_{49}, z_{64}) to have the highest sensitivity, with primary spherical aberration (z_9) the most sensitive. It was found that the rigorous mask topography phase errors from the left and right illumination poles of a symmetric source are identical, thus a good fit to the radially dependent and rotationally symmetric form of spherical aberration, shown in Figure 30. As discussed in section 2.1.3, spherical aberration provides an aperture dependent focal point, which justifies why it may be well suited for the compensation of mask induced pitch dependent best focus. Since spherical aberration is the most promising, a study of its impact on a lithographic system is presented in the next section.

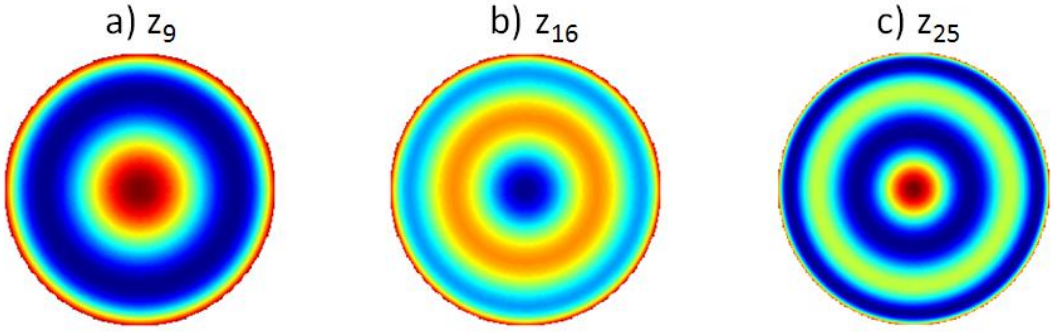

Figure 30: Pupil wavefront fingerprint of a) primary b) secondary and c) tertiary spherical aberration

4. SPHERICAL ABERRATION STUDIES

Phase differences between the diffraction orders can cause undesired phenomena, such as the asymmetry in the FEM that is deemed tilt [234]. This tilt can be caused by the spherical aberration induced by the resist [235], the mask topography, or the lens system. The following study was conducted in order to gain an understanding of FEM tilt's dependencies on mask, source, and lens parameters. First, the influence of imaging into resist is reviewed. Second, rigorously simulated aerial images of a small pitch are evaluated in order to study mask topography induced FEM tilt. Finally, the effect of lens induced spherical aberration on a large pitch imaged into air is studied and modeled.

4.1 Spherical aberration caused by resist

Imaging into resist has been modeled and found to lead to a pitch dependent best focus [236], [237], which is characteristic of spherical aberration [238]. This is because a planar interface between two media leads to an angular dependent focal point, as shown in Figure 31. According to Snell's law (Equation 25), for a converging beam that would have focused at a depth of t, the depth due to the interface for paraxial rays ($\theta_1 \sim 0$) becomes $d = t \cdot n_2/n_1$. The rays of light with a larger angle focus at a larger depth than for the paraxial angle. These differences will be noticeable if the radius of the converging beam, r, is large.

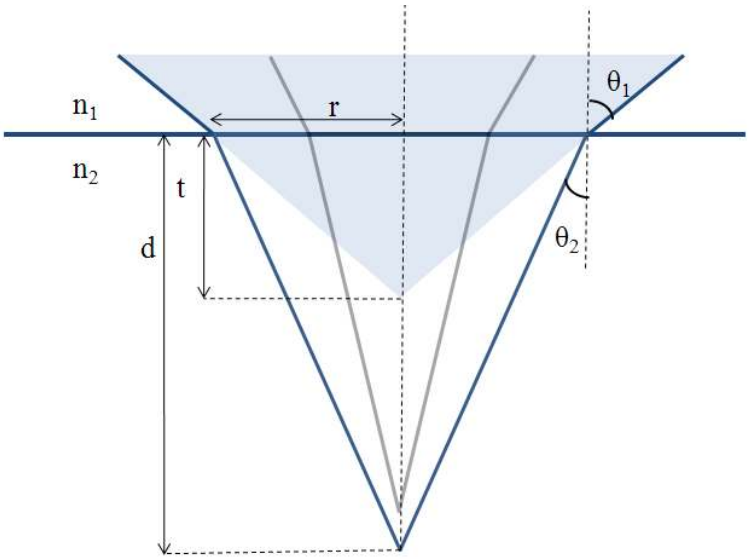

Figure 31: A planar interface between two media causes an angular dependent focal point.

The depth, d, that results from an incident angle θ_1 can be calculated with:

$$d = \frac{t \tan(\theta_1)}{\tan(\theta_2)} = \frac{t \tan(\theta_1)}{\tan(sin^{-1}(n_1/n_2 \sin(\theta_1))} \tag{52}$$

This new depth increases as a function of incident angle, as shown in Figure 32. The incident angle was converted to a pitch using the diffraction equation for the 1st order; $p=\lambda/\sin\theta$. This plot represents the longitudinal spherical aberration (LA); the displaced focal point along the optical axis for each incident angle. Note that the spherical aberration of resist dictated by Snell's law is defined as negative, the opposite of that depicted in Figure 20.

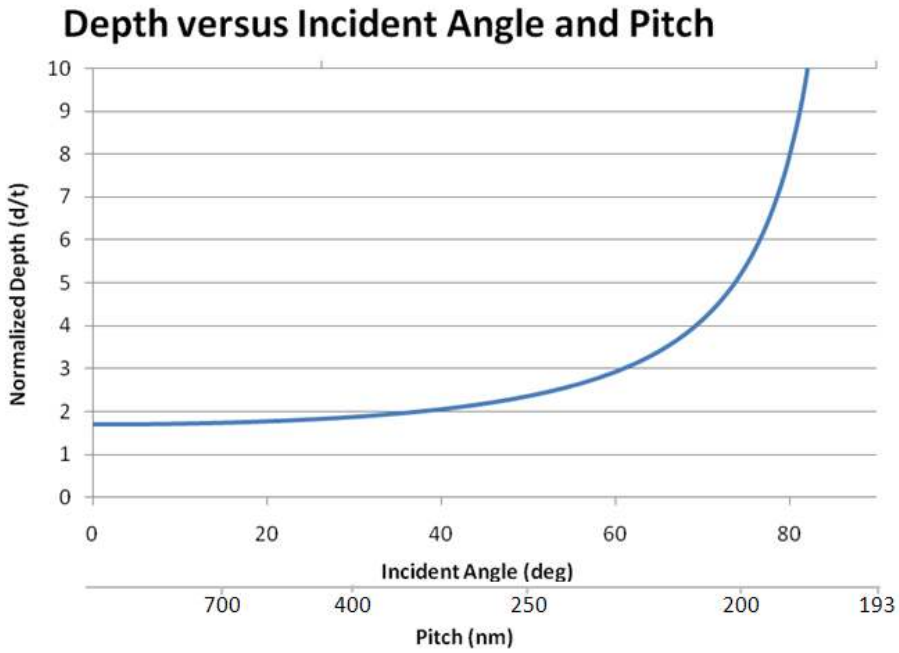

Figure 32: Depth of focal point versus incident angle and corresponding pitch, calculated for an air to resist interface with n_2=1.7 at λ=193 nm

The focal point for paraxial rays is located at $d=t\cdot n_2/n_1$ below the interface, thus this plane is defined as the paraxial image plane. Since rays with higher incident angles do not intersect the paraxial image plane at the optical axis, a plot of the height of each ray will represent the induced transverse aberration (TA). Taking a cutline at the paraxial image plane, the height of each ray is calculated as the transverse deviation from the optical axis. For a wavefront with no aberration, the ray height would be zero for all incident angles, indicating that all rays come to a focus at that point. The calculated transverse ray height versus NA for the planar interface at the paraxial image plane follows the relationship below:

$$TA = -LA\frac{r}{d} = \left(\frac{n_2}{n_1}\cdot t - d\right)\cdot\frac{r}{d} \tag{53}$$

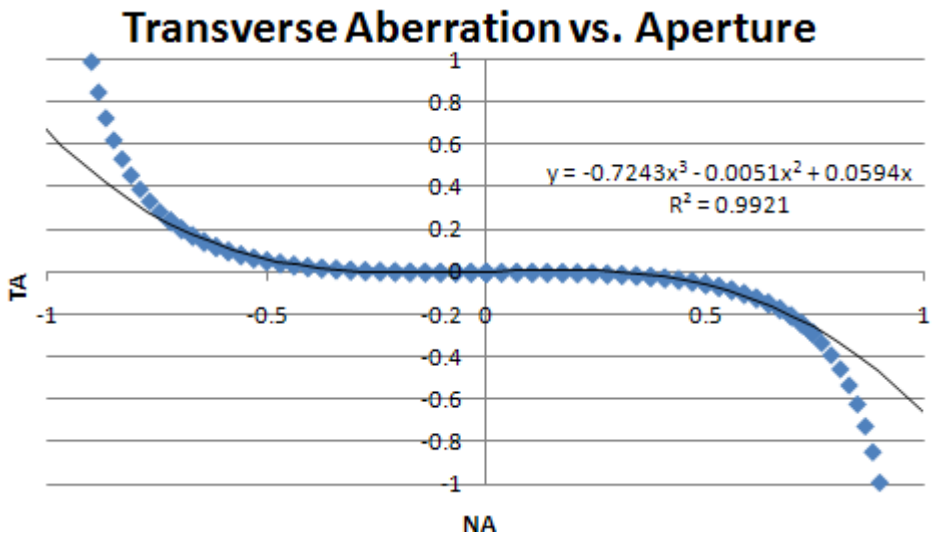

Figure 33: Plot of ray height versus angle at paraxial image plane using t=1, n_1=1 and n_2=1.7.

The plot in Figure 33 represents the transverse spherical aberration; the ray height as it intersects the paraxial image plane. Numerical aperture, $NA = r/\sqrt{(r^2 + z_2^2)}$, is plotted on the x axis instead of the aperture radius in order to keep the distance between the lens and the wafer, z_2, arbitrary. The fitted third order polynomial fits the ray height very well, with an R^2 value of 0.9921 for NA<0.72, which shows that the ray height clearly has r^3 dependence, representative of spherical aberration as defined in Equation 26. In order to accurately describe the polynomial at higher NA values, the polynomial would have to include the higher order spherical terms, r^5 and r^7. The first order dependence of the fitted polynomial in Figure 33 indicates a defocus term, which would be expected since spherical aberration induces a focus shift.

The induced aberration can also be expressed in terms of the OPD, or the integral of the transverse aberration as mentioned in section 2.1.4. Thus, the OPD follows an r^4 and r^2 dependence, representative of spherical aberration and defocus as listed in Table 1. This could be normalized to the primary spherical aberration Zernike polynomial. Again,

this would balance the image plane between the focal planes for paraxial and marginal rays in order to have the smallest spot size.

Since resist induces this spherical shaped aberration, a resist image calculated with an un-aberrated wavefront would be closely approximated by an aerial image calculated with this OPD wavefront in the pupil plane. It also suggests that spherical aberration induced in the pupil plane with a value the opposite of that induced by the resist could be used for compensation. Theoretically, resist induces negative spherical aberration since the marginal focal plane is deeper than the paraxial focal plane, thus a small positive amount of spherical aberration in the lens would be expected for compensation.

Simulations using the Kirchhoff approximation, shown in Figure 34, were completed with both an AltPSM and an AttPSM and with both a 1:1 duty ratio and a constant 45 nm line through pitch. A lumped parameters model (LPM) was used to represent the resist, with n=1.7. The best focus was found for multiple pitches between 90 and 300, and the ΔBF was calculated as the range. The coefficient of primary spherical aberration induced in the pupil plane (z_9) was varied from -0.1 to 0.1, in units of waves. In all cases, the ΔBF was reduced with a small positive amount of spherical aberration, as expected. The ΔBF could be reduced further by also inducing higher order spherical aberration, z_{16} and z_{25} in the lens. Lens induced spherical aberration is discussed further in section 4.3.

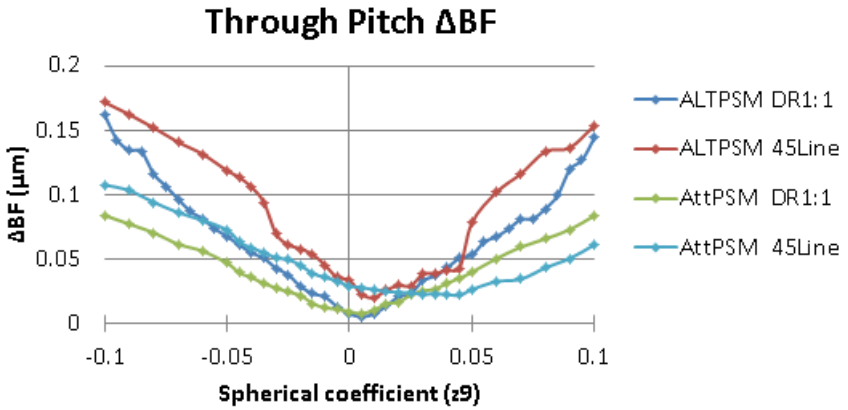

Figure 34: Pupil plane induced spherical aberration can compensate for that induced by the resist, seen as the reduction of the ΔBF with a positive amount of z_9

Coherency was found to have a compensating effect on FEM tilt. Figure 35a shows the simulation of a binary 600 nm line in a 1200 nm pitch with a σ= 0.3 λ= 365 nm 0.5NA system, revealing asymmetry due to the resist. However, if a coherent source is used, σ= 0, then the asymmetry of the FEM is drastically reduced, shown in Figure 35b. This coherency effect is discussed further in section 4.4.

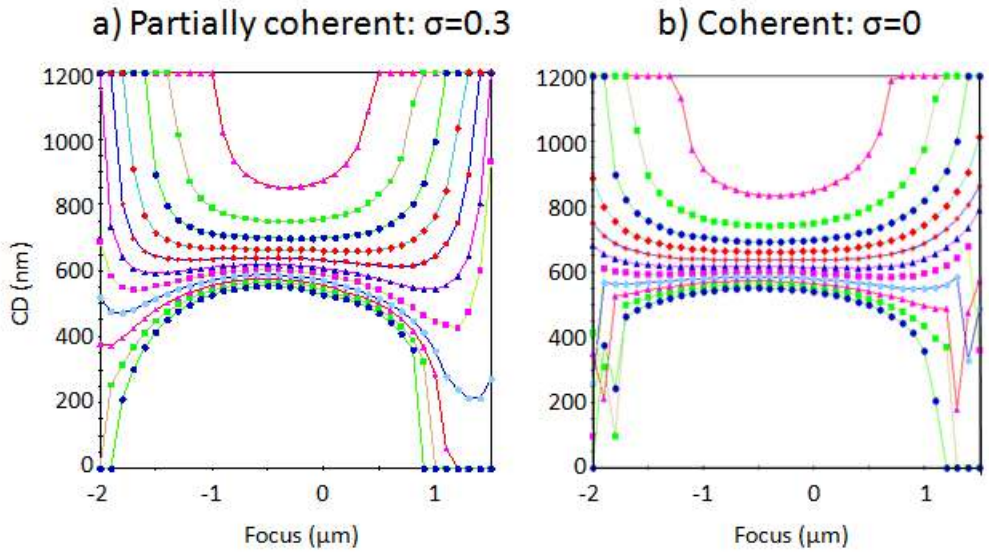

Figure 35: FEM for *p*=1200 nm λ=365 (a) σ= 0.3 shows asymmetry and (b) σ= 0 improved symmetry

4.2 Spherical aberration caused by mask topography

When the mask features are on the order of illuminating wavelength, the topography of the mask can induce aberrations which increase the tilt of the FEM, especially for strong phase shift masks [239] and AttPSM illuminated with TE polarization [240]. To illustrate this phenomenon, a chromium oxide on fused silica AltPSM with 90 nm pitch, 45 nm line, and a λ= 193 nm σ= 0.3 1.35NA system was studied. An aerial image simulation performed with the Kirchhoff approximation is shown in Figure 36a, which shows a symmetric FEM about a best focus of 0 µm. Using a ±10% CD specification around the 45 nm target and a 3% exposure latitude requirement, the DOF is 200 nm. However, for the same input parameters except using the rigorous Maxwell model to represent the three dimensional (3D) topography of the mask, the FEM is asymmetric with a nonzero tilt, shown in Figure 36b. The 3D mask effects reduce the DOF to only 120 nm.

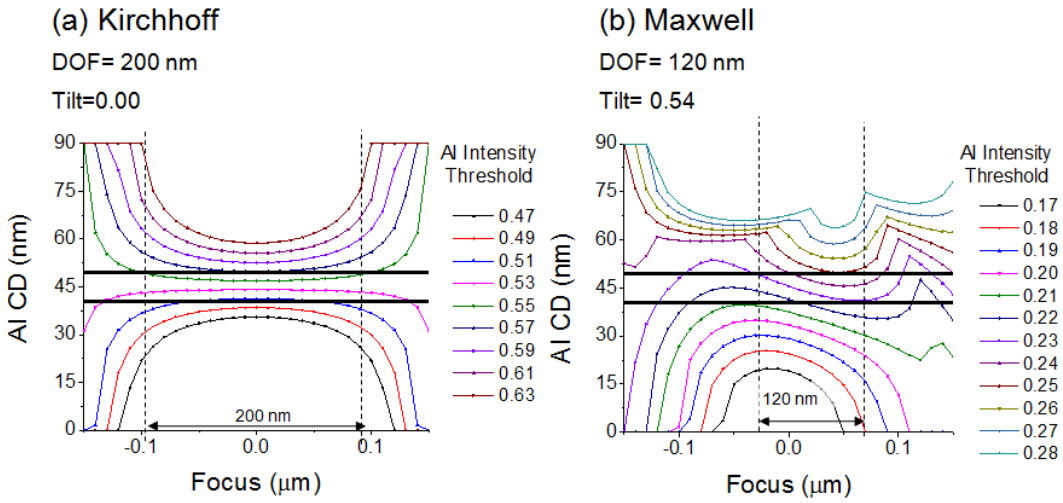

Figure 36: Aerial Image line FEM for an AltPSM p= 90 nm, σ= 0.3 with (a) Kirchhoff approximation and (b) rigorous Maxwell model.

The FEM tilt is dependent on the source distribution, correlated to the number of beams contributing to interference. When the pitch is larger than λ/NA, an on-axis source point can resolve the features, thus three-beam interference creates the image. In this argument, the induced aberration of the mask topography is assumed to be proportional to the Fringe Zernike primary spherical aberration: $\Phi = z_9(6r^4-6r^2+1)$. Since the 0^{th} order is in the center of the pupil, $r=0$, and the $\pm1^{st}$ orders are at some radius r_0, the induced phase due to the spherical aberration for the $\pm1^{st}$ orders is different than that of the 0^{th} order. This induced phase affects the image, causing FEM tilt, which can be seen in Figure 37a.

However, when two beam imaging is used such that the diffraction orders are perfectly symmetric in the pupil, the induced phase of each order is identical thus can be considered a constant and the image is not affected. This occurs with dipole illumination where $\sigma_R = 0$, calibrated so that the zero and first orders are symmetric in the pupil. An FEM from a dipole illuminated binary mask which maintains its symmetry is shown in Figure 37b. If this calibrated dipole is used with an alternate pitch, the orders will no longer be symmetric in the pupil, and asymmetry can again be observed in the FEM.

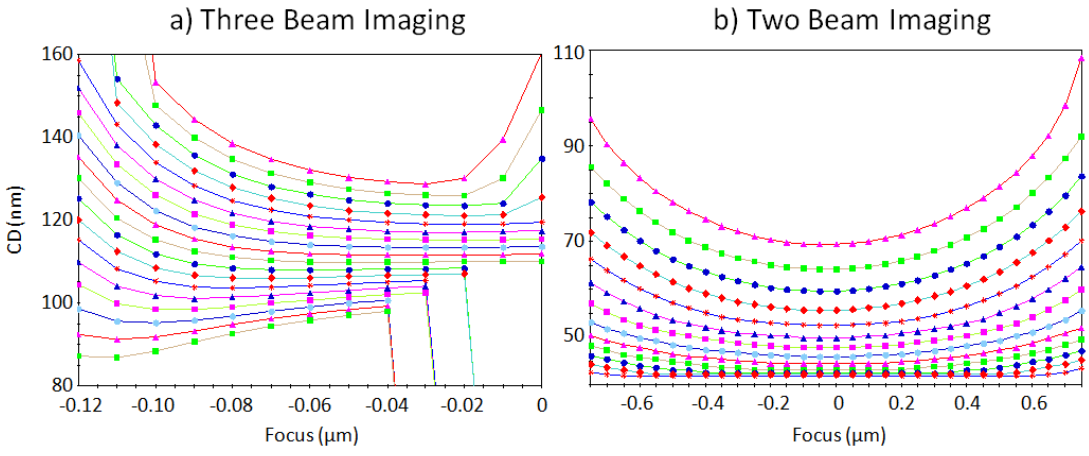

Figure 37: Rigorous binary FEM of 1:1 features for (a) three beam imaging of p=240 nm and (b) two beam imaging of p=120 nm.

Again, coherency can have a compensating effect on FEM tilt, revealing the similarities between the aberration induced by resist and that induced by the mask. Figure 38 shows the AI FEM and AI through focus for both a coherent source and a partially coherent σ= 0.3 source. With the partially coherent illumination, the FEM contains a negative tilt, and the AI through focus does not contain an isofocal point. With coherent illumination, the FEM is symmetric and the AI through focus does contain an isofocal point. This relationship reveals the same trend as the relationship between resist induced spherical aberration and coherency, which suggests that a lens induced spherical aberration could be used for mask topography compensation.

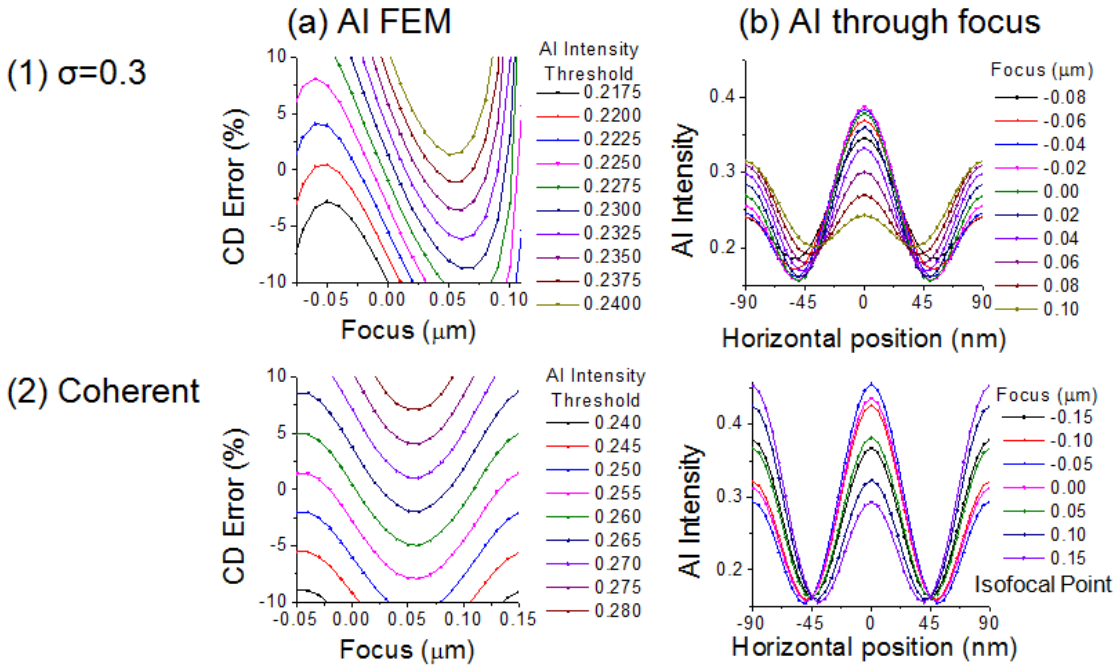

Figure 38: AltPSM (a) aerial image line FEM and (b) AI through focus for (1) a σ= 0.3 source shows asymmetry and no isofocal point and (2) coherent source shows symmetry and isofocal point

4.3 Spherical aberration induced by lens

The tendencies of lens induced spherical aberration are studied here with an aerial image of a 1200 nm pitch in order to exclude resist and mask topography effects.

Simulations show that an incoming wavefront with spherical aberration causes a pitch dependent best focus. The Normalized Image Log Slope (NILS) is proportional to the exposure latitude, thus the best focus occurs where the NILS is a maximum. In Figure 39, with an applied lens spherical aberration of z_9=+0.3, the focus with the maximum NILS is a function of k_1, which is defined as $k_1 = \frac{NA}{\lambda} hp_{min}$. The lens induced spherical aberration also causes the FEM to tilt according to the sign of the coefficient, shown in Figure 40. The best focus is shifted to -2.5 µm with z_9= -0.3 and to +2.0 µm with z_9=+0.3, showing spherical aberration's tendency to shift the best focus.

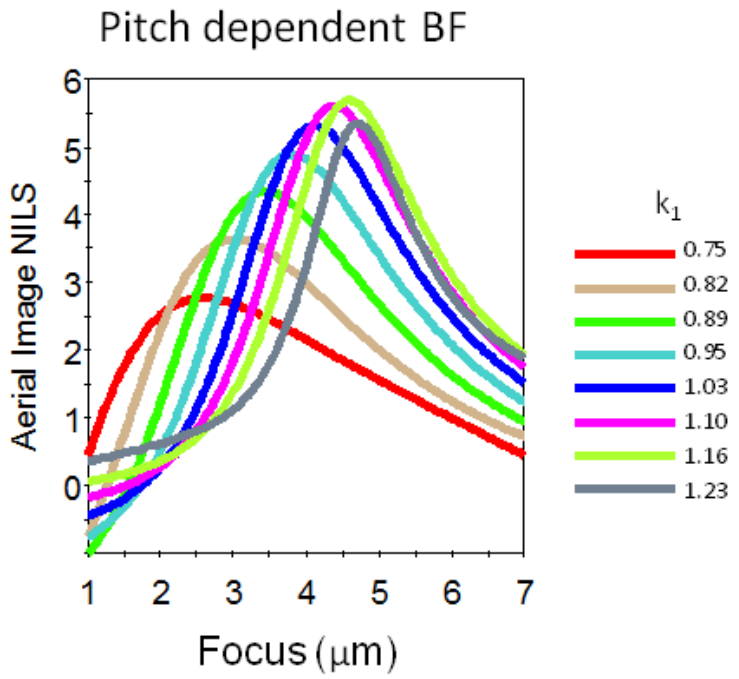

Figure 39: With z_9=+0.3, shift in maximum NILS as a function of k_1 corresponds to a pitch dependent best focus shift

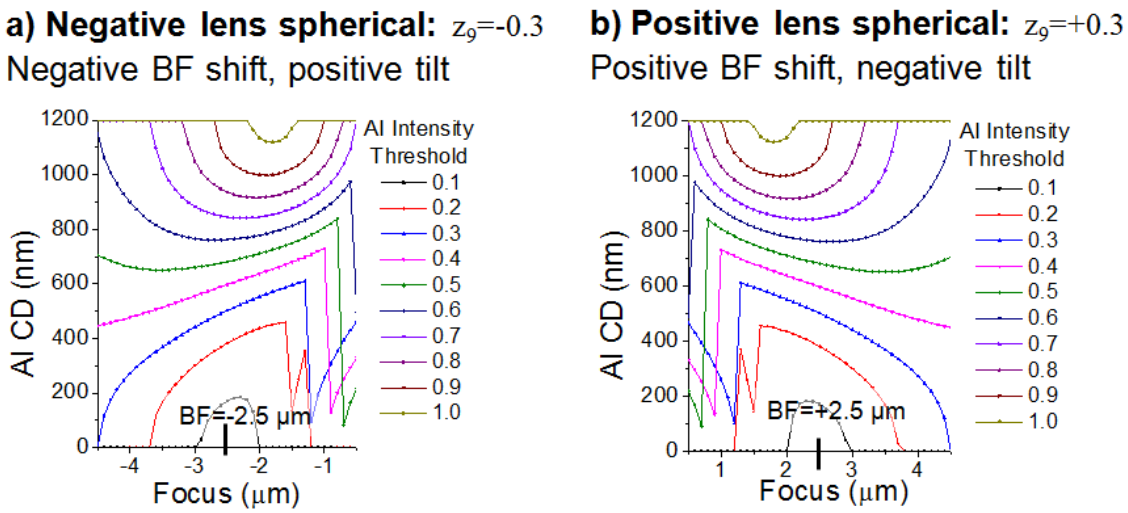

Figure 40: (a) FEM due to negative induced spherical has a negative BF shift and a positive tilt. (b) FEM due to positive induced spherical has a positive BF shift and a negative tilt.

The aerial image through focus due to the positive lens induced spherical aberration is shown in Figure 41, with the corresponding tilted FEM in Figure 40b. The spherical aberration causes the aerial image to no longer contain an isofocal point, meaning there is no exposure that will allow the CD to be constant through focus. Instead, the CD changes with focus, giving the tilted appearance to the FEM.

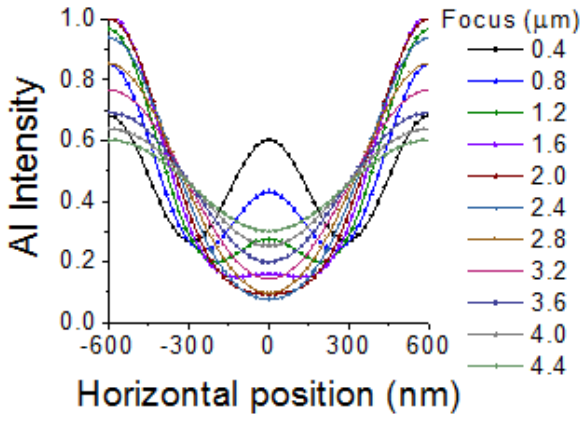

Figure 41: Aerial image through focus due to spherical aberration z_9=+0.3 for p=1200 nm on binary mask with NA=0.5, σ=0.3, λ=365 system (corresponding FEM shown in Figure 40b)

Lens induced spherical aberration also depends strongly on the coherency of the source. For a coherent source, an isofocal point is observed in the aerial image even with

z_9=+0.3 waves of spherical aberration, as shown in Figure 42a. Its corresponding symmetric FEM is shown in Figure 43a. However the induced spherical aberration does induce a large best focus shift, as expected. The isofocal point is removed by using a two-point dipole source with σ_C= 0.2 σ_R= 0, shown in Figure 42b with the corresponding tilted FEM in 43b. This reveals that FEM tilt is not caused only by the numerous directions of plane waves from an incoherent source; it can be induced by one off-axis plane wave, mirrored for source symmetry.

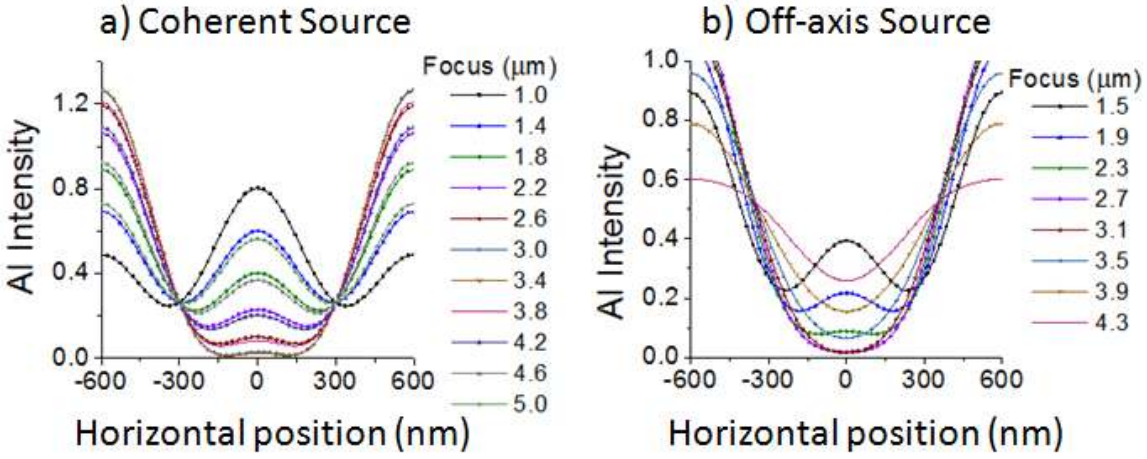

Figure 42: Aerial image due to z_9=+0.3 waves of spherical aberration with (a) a coherent source has an isofocal point and (b) σ_C= 0.1 σ_R= 0 λ= 365 dipole source does not have an isofocal point

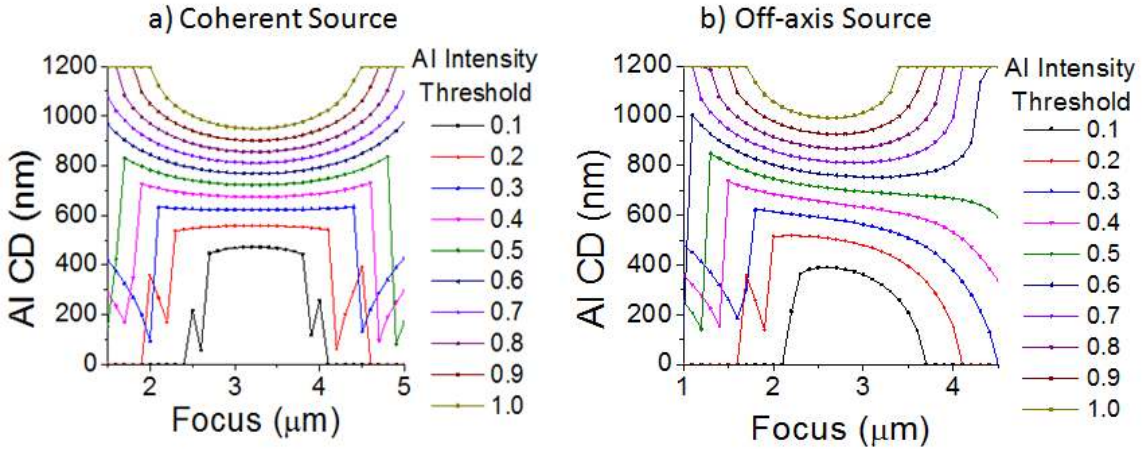

Figure 43: Aerial image FEM due to spherical aberration z_9=+0.3 with (a) a coherent source is symmetric and (b) σ_C= 0.1 σ_R= 0 λ= 365 dipole source is asymmetric

4.4 Modeling effects of spherical aberration

In order to develop an understanding of the coherence dependence on lens induced spherical aberration, an aerial image was analytically studied. With the intention of evaluating the effects of off-axis illumination while maintaining source symmetry, the model uses a dipole point source, which samples the two outer edges of a conventional source; thus the right source point is at a positive σ location and the left source point is at negative σ location. The pitch is scaled such that the zero, positive first, and negative first diffraction orders from both the right and left source points are collected. The diffraction pattern is the Fourier Transform of a rectangular mask with pitch *p* and space *s*, resulting in radial locations defined by the diffraction equation, and amplitudes from Equation 18.

$$r_0 = \sigma \tag{54}$$

$$r_{\pm 1} = \sigma \pm \frac{\lambda}{NA \cdot p} \tag{55}$$

$$r_{0\_LEFT} = -\sigma \tag{56}$$

$$r_{\pm 1\_LEFT} = -\sigma \pm \frac{\lambda}{NA \cdot p} \tag{57}$$

$$A_0 = \frac{s}{p} \tag{58}$$

$$A_{\pm 1} = \frac{s}{p}\mathrm{sinc}\frac{s}{p} \tag{59}$$

The induced phase on each diffraction order is the sum of that due to both defocus and spherical aberration, where z_4 is the defocus coefficient, and z_9 is the primary spherical coefficient.

$$\theta(r) = z_4(2r^2 - 1) + z_9(6r^4 - 6r^2 + 1) \quad (60)$$

The electric field is the inverse Fourier Transform of each order and is a function of the amplitude, radial location, and induced phase, where the horizontal position is denoted by x.

$$E_0 = A_0 e^{-i2\pi r_0 x \frac{NA}{\lambda}} e^{i\theta_0} \quad (61)$$

$$E_{\pm 1} = A_{\pm 1} e^{-i2\pi r_{\pm 1} x \frac{NA}{\lambda}} e^{i\theta_{\pm 1}} \quad (62)$$

The aerial image intensity is the sum of aerial images from the right and left poles:

$$I = |E_0 + E_{+1} + E_{-1}|^2 + \left|E_{0\_LEFT} + E_{+1\_LEFT} + E_{-1\_LEFT}\right|^2 \quad (63)$$

The aerial image intensity with an applied spherical coefficient of z_9 of +0.3 is graphed in Figure 44 for both coherent illumination, σ=0, and off-axis source points at σ=0.2. The coherent aerial image contains an isofocal point, which results in a symmetric FEM. For the on-axis source point in Figure 44a, the aerial image intensity profile is symmetric about a defocus of 0; the profile at z_4 of -0.25p is identical to the profile at z_4 of +0.25p. However, with the off-axis illumination shown in Figure 44b, even though the mask is illuminated with only one plane wave at a relatively low σ, there is no isofocal point leading to a tilted and asymmetric FEM. These trends are identical to those found through rigorous simulation shown in Figure 42 [230].

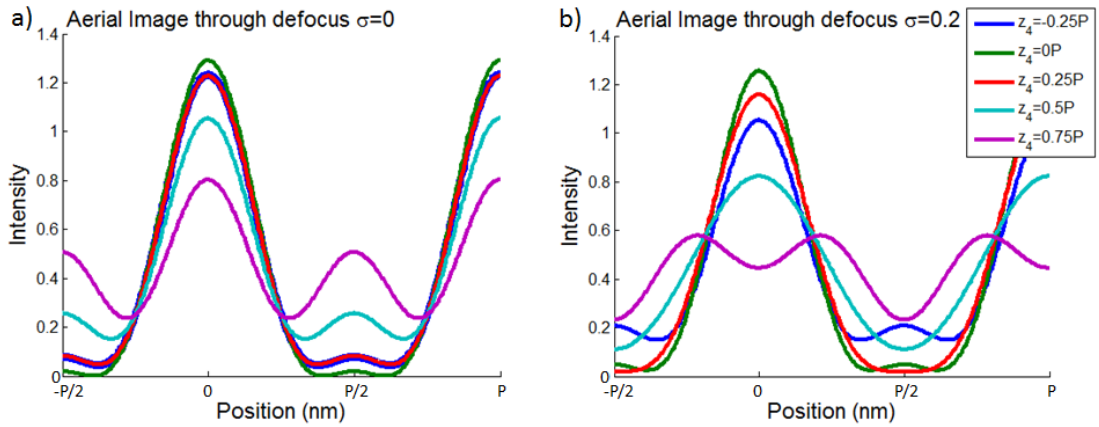

Figure 44: Aerial image through defocus with z_9 of +0.3 for a) coherent illumination has an isofocal point and b) σ = 0.2 source points has no isofocal point so leads to an asymmetric FEM.

Another way to view this trend is depicted in Figure 45, where the intensity is plotted as a function of defocus for multiple horizontal positions. With the coherent illumination shown in Figure 45a, the intensity is constant through defocus at a horizontal position x of *p*/4, which represents the isofocal point and leads to a symmetric FEM. For the σ= 0.2 off-axis source points, there is no horizontal position that maintains a constant intensity, thus it leads to a tilted FEM. Also, the graphs reveal that for the coherent illumination, the best focus is constant through horizontal position. This is observed by the defocus z_4 of 0 that has both a maximum in intensity for the space (blue) and a minimum in intensity for the line (red). However, for the off-axis illumination, the maximum intensity for the space (blue) occurs at a defocus z_4 of 0, which differs from the best focus z_4 of *p*/8 for the line (red).

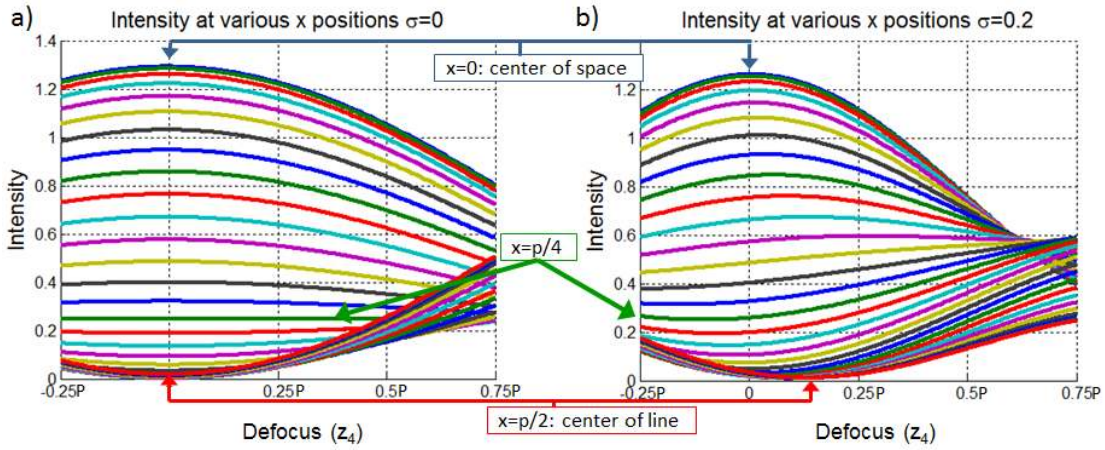

Figure 45: Aerial intensity with z_9 of +0.3 as a function of defocus at multiple horizontal positions for a) coherent illumination and b) σ=0.2 source points. For coherent illumination, the intensity is constant through defocus at a horizontal position of x=*p*/4, which represents an isofocal point and leads to a symmetric FEM.

The dependency of the isofocal point on the partial coherence of the illumination can be explained with a simple diagram, depicted in Figure 46. A lens induced primary spherical aberration is shown in blue, using the Fringe Zernike normalization shown in Table 1. The radial locations of diffraction orders are shown for both an on-axis and an off-axis point source. The induced phases of the diffraction orders from an on-axis point source can lie on a quadratic function, which represents paraxial defocus, shown as green in Figure 46a. Thus, even in the presence of spherical aberration, the phases can be modeled and perceived as a defocus aberration. This results in symmetric aerial image intensity profiles about best focus, which leads to a symmetric FEM. However, for an off-axis source point, the shifted diffraction orders are no longer symmetric in the pupil thus cannot be modeled by an axially symmetric quadratic function. The quadratic function that fits the 0^{th} and positive 1^{st} orders (solid green) is different than the function that fits the 0^{th} and negative 1^{st} orders (dashed green), shown in Figure 46b. Thus, the effect on the image is no longer a shift in best focus, leading to the disappearance of the isofocal point and a tilted FEM.

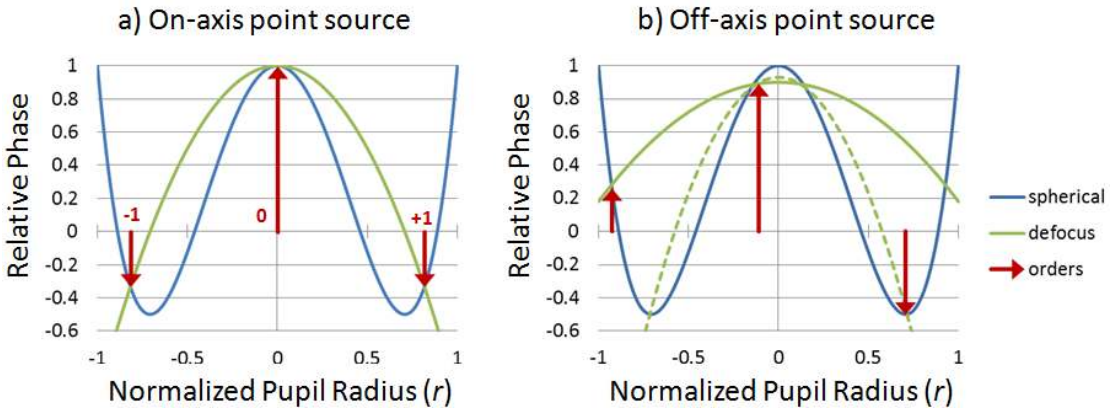

Figure 46: Phases induced by diffraction orders due to spherical aberration are shown as arrows. The phases for (a) an on-axis point source can be modeled as defocus, shown as dashed, (b) but for an off-axis point source cannot.

5. SIMULATION AND OPTIMIZATION

5.1 Simulation parameters

Simulations with thick mask stacks were performed in order to find wavefront solutions which compensate for mask topography effects. The 4x optical reduction 193 nm lithographic scanner was simulated with PROLITH™, a commercial lithography simulator, by solving Maxwell's equations using the RCWA algorithm [241]. The accuracy of PROLITH™ has been extensively studied [242]–[246]. The simulations were integrated with Matlab, a numerical computing environment and programming language, in order to utilize data manipulation capabilities [247].

To extract the BF and UDOF, a simulation with varying exposure and focus values was performed. In order to ensure that the simulation was robust through a large focal range, a test was done to identify issues such as image inversion and placement error. First, an FEM with a large range in values and a small step size was performed in order to estimate the appropriate range in values that should be used, without a long runtime. Then a second FEM was performed with the smaller range and step size so that the BF and DOF was as accurate as possible. PRODATA™ was used to calculate the UDOF over multiple features. A schematic of the calculation method is depicted in Figure 47. An example Matlab script that connects to PROLITH™ and performs an FEM is shown in Appendix A.

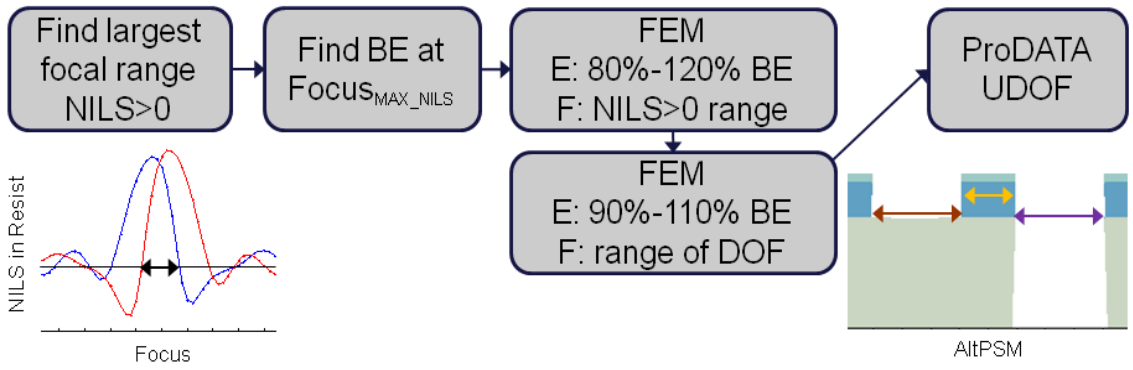

Figure 47: Simulation method to calculate UDOF over multiple features on an AltPSM

Three mask types were evaluated in a 1.35NA system: 1D lines on a strong AltPSM, 1D lines on a 1% AttPSM, and contact holes on a 6% AttPSM. The AltPSM was modeled with a 171 nm substrate phase etch and the 73 nm Cr/CrO absorber from a binary mask, and the illumination was an XY polarized conventional source with a partial coherence of 0.3. The 45 nm lines through pitch on the thick 1% AttPSM and the 45 nm contact holes through pitch on the 6% AttPSM were biased to print at the same exposure. The 1% AttPSM stack contained 34 nm of Ta under 113.5 nm of SiON, and 6% AttPSM stack utilized a 68 nm layer of a molybdenum oxide – silicon oxide (MoO_3-SiO_2 or MoSi) composite film. The optical constants of constituent materials are shown in Table 2.

The illumination for the AttPSMs was an XY polarized C-Quad with inner and outer σ values of 0.86 and 0.66, at a 30° opening angle. The diffraction pattern was calculated at multiple incident angles corresponding to the illumination source. The measured data of the applied illuminator on the tool was used as the source. A full physical resist model was used for the 1D lines, and a lumped parameter model was used to model a negative tone contact hole process. Focus response values were extracted to tolerate for exposure variations (or exposure latitude) of 10%.

Table 2: Mask stack parameters for rigorous simulations

Mask	Layer	n	k	t
Substrate	Qz	1.56312	0	-
Binary	Cr	1.477	1.762	55
	CrO	1.965	1.201	18
thin AttPSM	MoSi	2.343	0.586	68
thick AttPSM	Ta	2.07	1.74	34
	SiON	1.86	0.01	113.5

5.2 Optimization algorithm

5.2.1 Genetic algorithms

In optimizing multiple spherical aberration Zernike coefficients, the vast parameter space coupled with the computational complexity of Maxwell's rigorous calculations require a smart optimization algorithm. In this project, a genetic algorithm was employed, which is fundamentally a smart sampling method. A genetic algorithm can be considered a global heuristic-search method, and can be considered self-adaptive, since each generation of sampling depends on the success of the parent generation [248]. They require little knowledge of the system, so analytic formulations of the objective functions are not required [249]. The merit function can be composed for a particular process and needs only to be able to be computed at each iteration. They also can be adapted to almost any task and have had success with many nonlinear problems, such as optimizing circuit speed, control dynamics of an induction motor, and control of a permanent magnet motor [250]–[252].

Genetic algorithms mimic the evolutional process first identified by Darwin [253]. Functions to represent selection, mutation, and recombination are defined. After an

initial sample of “individuals” the next generation of sample points is calculated as the combination of pairs of the parent generation. The algorithm proceeds in four major steps [254]. First, initialization of the candidates is performed according to the desired population. Second, an evaluation of each candidate's fitness value is performed with a specified merit function. At this point, if the fitness values meet the termination criteria, the algorithm terminates. Third, the selection process pairs the candidates according to predetermined selection criteria. Fourth, in the recombination step, new candidates are generated by mixing the characteristics of the parent pair. New candidates can also be altered by a mutation, which is a random change. Finally, the evaluation, selection, and recombination processes are repeated until the termination criteria is reached.

The termination criteria can be defined as a number of generations or a target fitness value. Additional parameters can be employed to model other phenomena, such as migration and niching (restricting the selection criteria to promote higher diversity). In migration, the determination of which points will be selected is essentially modeled as a probability function. Those with low fitness values will be rarely but not never selected. After recombination, the children would likely contain similar characteristics to those individuals in the parent generation with the highest fitness values. Mutation is an important phenomenon that prevents convergence towards local optima, but also limits convergence. A high mutation rate would cause the algorithm to act as a random sampling algorithm without the knowledge of selection and recombination.

Genetic algorithms have been used with lithography systems in order to optimize rectangular mask shapes [254]. Genetic algorithms were also used as a heuristic search algorithm in order to solve for the mask and illumination layouts which provide the

highest process latitude [255]. They have even been used to perform OPC [256] and calibrate resist models [257].

5.2.2 MKS Algorithm

A mutation-only genetic algorithm was developed that utilizes both exploration (broad search) and exploitation (local search) to optimize the process latitude over multiple feature densities. The algorithm was named MKS, simply the initials of the author. A Matlab script for maximization is shown in Appendix B. All initialized and modified candidates were defined on a Cartesian grid with a step of 0.01, which represents the desired precision and prevents unnecessarily close computations. In order to limit the number of computations, a "Tabu" search was implemented, which ensures that each candidate was only calculated once, regardless of whether it was selected for a future generation. Each candidate represented values of three coefficients of spherical aberration, such as z_9, z_{16}, and z_{25}. The coefficient was represented in units of waves. For example, a coefficient of 0.1 represents an aberration with its maximum value at $0.1\lambda = 0.1 \cdot 193$ nm = 19.3 nm.

The MKS algorithm contained four stages; Initialization, Assessment, Selection, and Modification. In the Initialization stage, 27 candidates were defined on a 3x3x3 Cartesian grid where each coefficient z_n had the values {-0.1, 0, 0.1}. To reach the desired population of 40, 13 additional candidates were defined randomly. In the Assessment stage, each candidate was graded based on a merit function of either UDOF or ΔBF, using the rigorous lithography simulator. If UDOF was the merit function, then the algorithm operated to maximize, and if ΔBF was the merit function, the algorithm operated to minimize. Then for each of the 10 iterations, the Selection, Modification, and

Assessment stages repeated. In the Selection stage, the 5 best candidates were selected to be parents. In the Modification stage, 8 children were created from each parent. In order to exploit the local region, children adjacent to the parents were generated with the highest priority (deemed a hill climbing algorithm). Then when all neighbors were calculated, the child was generated by adding a random value in three dimensions to the parent, which allowed the parameter region to be explored.

A two dimensional illustration of the MKS algorithm in depicted in Figure 48, where only the upper quadrant is shown. The candidates are initialized on the z_n vs z_m grid, as both Cartesian points (blue solid) and random points (blue hollow). After the first assessment procedure, P1 has the highest merit function so is one of the parents for the first generation. During the first modification procedure, the 4 corners around P1 are generated as children (red). The second assessment procedure finds P2 as the parent for the second generation. During the second modification procedure, the 4 corners around P2 are generated as children (pink) except for the top right corner that is P1 so has already been assessed. Instead, a candidate to the side of P2 is generated (green). The third modification procedure finds that P2 is still the candidate with the highest merit, so children are generated from it for the 3rd generation. The remaining three adjacent candidates (yellow) are generated, as well as a random (orange) since all neighbors are already calculated. Note that the illustration only generates children for the top parent, whereas in the actual MKS algorithm, the 5 best parents are all generating children.

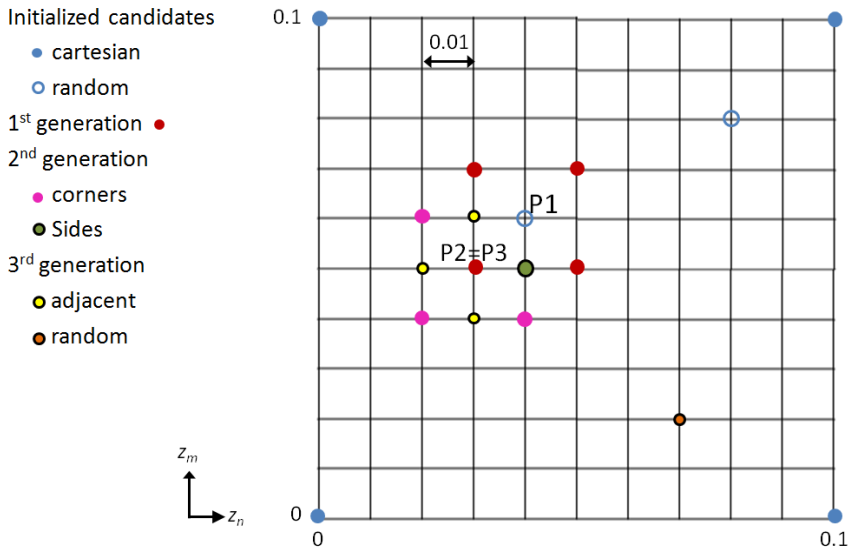

Figure 48: Two dimensional illustration of MKS genetic algorithm where the top parent generates 4 children in each subsequent generation.

For the 1D TaSiON case, with no applied offsets, the rigorous simulation revealed a UDOF of 74 and a ΔBF of 70 nm. An optimized amount of primary spherical aberration, z_9=+0.08, increased the UDOF to 129 nm, but was still limited by the DOF of the 180 nm pitch, shown as green in Figure 49a. The solution found by the MKS algorithm with a merit of maximum UDOF also utilized secondary spherical aberration; z_9=+0.05 and z_{16}=+0.08 reduced the ΔBF to 4 nm, shown in Figure 49b.

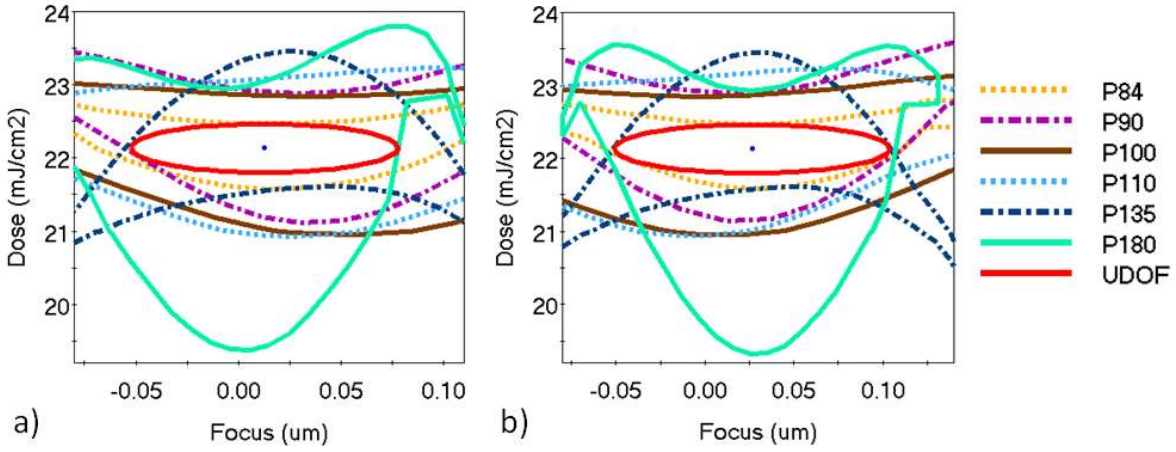

Figure 49: Simulated process windows of 1D lines from a 1% TaSiON a) with z_9=0.08 and z_{16}=0 has UDOF of 129 nm and c) with z_9=0.05 and z_{16}=0.08 has UDOF of 154 nm

For the 2D MoSi contact hole case, with no applied offsets, the rigorous simulation revealed a UDOF of 81 nm and a ΔBF of 53 nm, which is shown in Figure 65a. With a merit of maximum UDOF, multiple solutions were found in which the UDOF was limited by the pitch with the smallest DOF, shown in Figure 50a. A merit of minimum ΔBF led to a solution (z_9= -0.05 and z_{16}= -0.12) where all process windows were aligned, thus the aberrations induced by mask topography were better compensated, shown in Figure 50b.

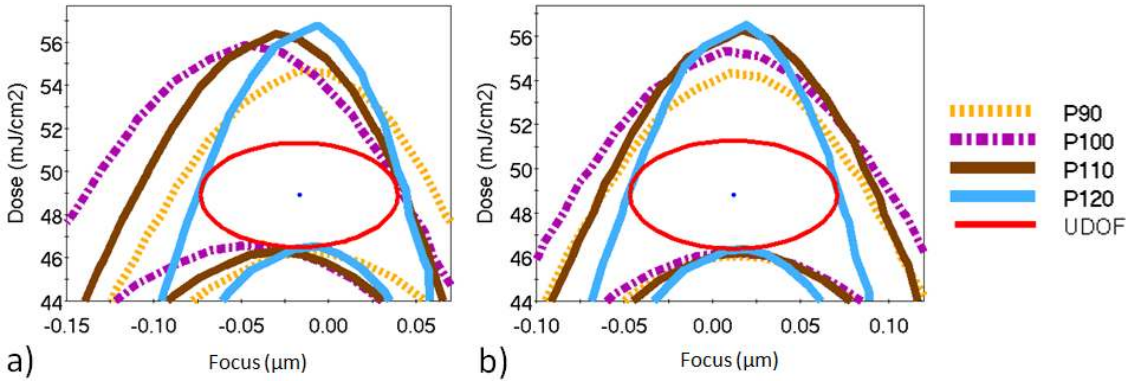

Figure 50: Simulated process windows of contact holes from a 6% MoSi AttPSM both have a UDOF of 115 nm. a) UDOF merit function's solution z_9= -0.05 and z_{16}=0 has a ΔBF of 35 nm, and b) ΔBF merit function's solution z_9= -0.05 and z_{16}= -0.12 has a ΔBF of 2 nm.

Analysis of the results from the genetic algorithm revealed that BF as a function of spherical coefficient is linear. Also, the BF as a function of primary spherical for a given pitch has the same slope regardless of what higher order spherical coefficients are applied. In Figure 51, the best focus versus primary spherical is plotted for various values of z_{16} and z_{25} for both a 90 nm and a 120 nm pitch. This reveals that the BF vs z_n slope, defined as $\delta BF/\delta z_n$, is independent of another applied Zernike, z_m, due to the additive nature of the Zernike polynomials.

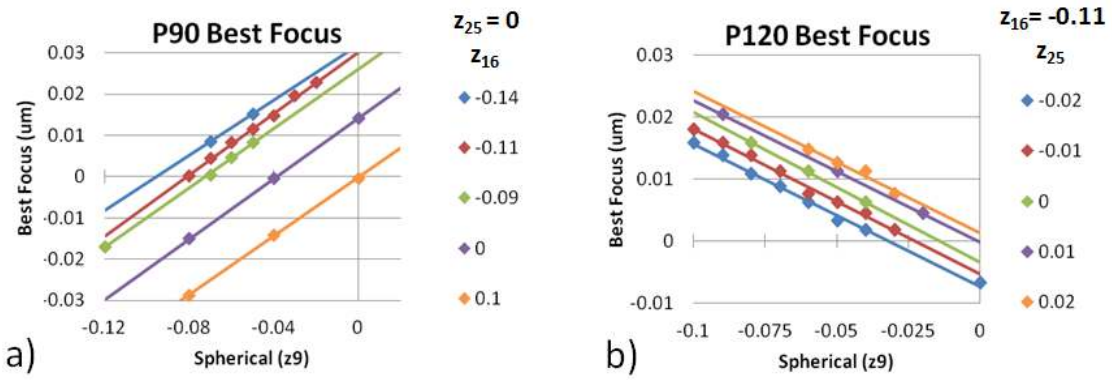

Figure 51: Simulated BF of contact holes versus z_9 coefficient for a) 90 nm pitch with z_{25}=0 at multiple z_{16} coefficients and b) 120 nm pitch with z_{16}= -0.11 at multiple z_{25} coefficients. Graphs reveal that for a given pitch, the slope of BF versus z_9 is independent of z_{16} and z_{25} coefficients.

5.3 Analytical spherical effect

The effect on BF due to spherical aberration is important to understand when predicting pupil wavefront compensation. An aerial image model with a dipole source was used to analytically derive the spherical slope independency. A high σ was used which resolves pitches below the coherent resolution limit, where only one of the first diffraction orders are captured. The location of the orders is similar to those defined in the previous section: r_0 and r_1 from Equations 54 and 55. For a partially coherent illumination source, the average σ value is used: σ_C. When multiple points are used to model the width of the illumination source, an identical trend is found due to the averaging.

$$r_0 = \sigma_C \tag{64}$$

$$r_1 = \sigma_C - \frac{\lambda}{NA \cdot p} \tag{65}$$

The phase induced on each diffraction order is defined by the linear combination of each spherical Zernike polynomial, as defined in Table 1.

$$\Phi_{spherical}(r) = z_9(1 - 6r^2 + 6r^4) + z_{16}(-1 + 12r^2 - 30r^4 + 20r^6)$$

$$+z_{25}(1 - 20r^2 + 90r^4 - 140r^6 + 70r^8) \quad (66)$$

Since the image for a given pitch is created by interfering the plane waves from the 0th and 1st diffraction orders, the phases induced on these orders determine the resulting shift in BF. Thus, the BF due to spherical for a given pitch can be estimated by fitting a quadratic to those phases, where the quadratic coefficient is proportional to the defocus shift, as shown in Figure 52. When the applied spherical z_9 is doubled as shown in Figure 52b, the fitted quadratic coefficient, z_4, also doubles, revealing the linear relationship.

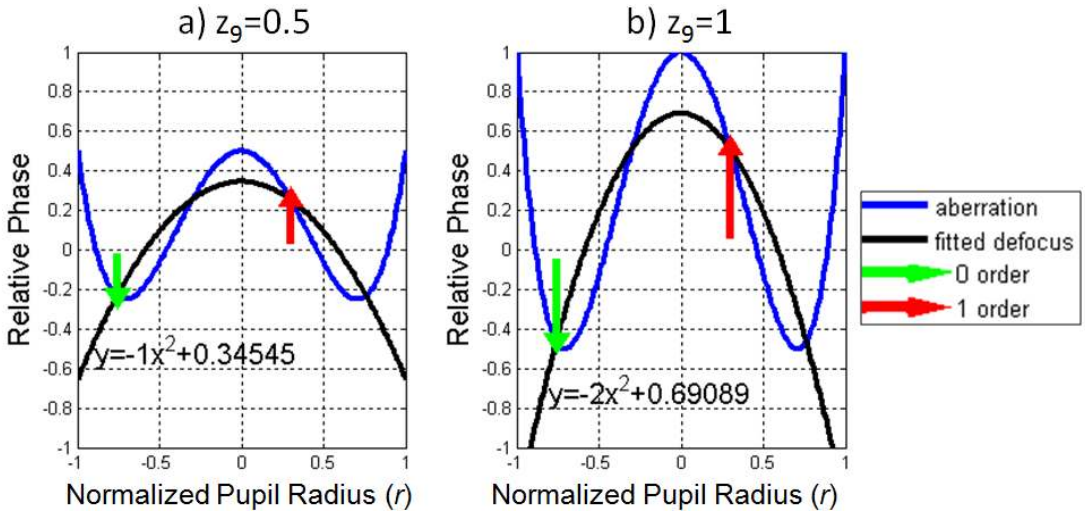

Figure 52: The BF shift due to primary spherical aberration is proportional to the z_4 coefficient of a quadratic fitted to the phases of the 0th and 1st diffraction orders. In this example, a pitch of 135 nm is illuminated by an off-axis pole of σ= 0.76. With a) z_9=0.5, the z_4= -1 and b) with doubled z_9 =1, the z_4= -2, revealing a linear relationship

The defocus coefficient for a given pitch and applied aberration can be found by fitting the diffraction orders to a quadratic equation, $y=ax^2+b$, where the a coefficient represents z_4, according to the Zernike definition of defocus:

$$\Phi_{defocus}(r) = z_4(2r^2 - 1) \quad (67)$$

The two (x,y) points on the quadratic that are known are (r_0, $\Phi_{spherical}(r_0)$) and (r_1, $\Phi_{spherical}(r_1)$), which gives two equations with two unknown quantities: z_4 and b.

$$\Phi_{spherical}(r_0) = z_4 {r_0}^2 + b \tag{68}$$

$$\Phi_{spherical}(r_1) = z_4 {r_1}^2 + b \tag{69}$$

Subtracting those two equations and solving for z_4 gives an expression for the defocus coefficient, which is proportional to the BF shift due to spherical.

$$\Phi_{spherical}(r_0) - \Phi_{spherical}(r_1) = z_4({r_0}^2 - {r_1}^2) \tag{70}$$

$$z_4 = \frac{\Phi_{spherical}(r_0) - \Phi_{spherical}(r_1)}{{r_0}^2 - {r_1}^2} \propto BF \tag{71}$$

In order to verify the linearity seen in Figure 51, the slope of BF as a function of z_9 is found by evaluating the BF at two separate values, z_{9_1} and z_{9_2}.

$$\frac{\delta \mathrm{BF}}{\delta z_9} = \frac{\mathrm{BF}(z_{9_2}) - \mathrm{BF}(z_{9_1})}{z_{9_2} - z_{9_1}} \tag{72}$$

Substituting Equation 71 into the BF of Equation 72 gives

$$\frac{\delta \mathrm{BF}}{\delta z_9} \propto \frac{1}{(z_{9_2} - z_{9_1})} \left\{ \left(\frac{\Phi_{spherical}(r_0) - \Phi_{spherical}(r_1)}{({r_0}^2 - {r_1}^2)} \right) |^{z_{9_2}} - \left(\frac{\Phi_{spherical}(r_0) - \Phi_{spherical}(r_1)}{({r_0}^2 - {r_1}^2)} \right) |^{z_{9_1}} \right\} \tag{73}$$

Then the phase of spherical from Equation 65 is substituted.

$$\frac{\delta \mathrm{BF}}{\delta z_9} \propto \frac{1}{(z_{9_2} - z_{9_1})} \left\{ \right. \tag{74}$$

$$\left(\frac{\mathbf{z_{9_2}}(1 - 6{r_0}^2 + 6{r_0}^4) + z_{16}(-1 + 12{r_0}^2 - 30{r_0}^4 + 20{r_0}^6) + z_{25}(1 - 20{r_0}^2 + 90{r_0}^4 - 140{r_0}^6 + 70{r_0}^8)}{({r_0}^2 - {r_1}^2)} \right.$$

$$-\frac{\boldsymbol{z_{9_2}}(1-6{r_1}^2+6{r_1}^4)+z_{16}(-1+12{r_1}^2-30{r_1}^4+20{r_1}^6)+z_{25}(1-20{r_1}^2+90{r_1}^4-140{r_1}^6+70{r_1}^8)}{({r_0}^2-{r_1}^2)}\Bigg)$$

$$-\Bigg(\frac{\boldsymbol{z_{9_1}}(1-6{r_0}^2+6{r_0}^4)+z_{16}(-1+12{r_0}^2-30{r_0}^4+20{r_0}^6)+z_{25}(1-20{r_0}^2+90{r_0}^4-140{r_0}^6+70{r_0}^8)}{({r_0}^2-{r_1}^2)}$$

$$-\frac{\boldsymbol{z_{9_1}}(1-6{r_1}^2+6{r_1}^4)+z_{16}(-1+12{r_1}^2-30{r_1}^4+20{r_1}^6)+z_{25}(1-20{r_1}^2+90{r_1}^4-140{r_1}^6+70{r_1}^8)}{({r_0}^2-{r_1}^2)}\Bigg)\Bigg\}$$

Since z_{16} and z_{25} are independent of z_{9_1} and z_{9_2}, those terms drop out.

$$\frac{\delta BF}{\delta z_9} \propto \frac{1}{\left(z_{9_2}-z_{9_1}\right)}\Bigg\{\frac{\boldsymbol{z_{9_2}}(1-6{r_0}^2+6{r_0}^4)-\boldsymbol{z_{9_2}}(1-6{r_1}^2+6{r_1}^4)}{({r_0}^2-{r_1}^2)}$$

$$-\Bigg(\frac{\boldsymbol{z_{9_1}}(1-6{r_0}^2+6{r_0}^4)-\boldsymbol{z_{9_1}}(1-6{r_1}^2+6{r_1}^4)}{({r_0}^2-{r_1}^2)}\Bigg)\Bigg\} \qquad (75)$$

After factoring out $z_{9_2}$and z_{9_1}, the ($z_{9_2}-z_{9_1}$) terms cancel out, leaving the following analytical expression:

$$\frac{\delta BF}{\delta z_9} = C\,\frac{(1-6{r_0}^2+6{r_0}^4)-(1-6{r_1}^2+6{r_1}^4)}{({r_0}^2-{r_1}^2)} \qquad (76)$$

where *C* represents the proportionality constant. This analytical expression is plotted for several pitches as a function of the σ_C values that result in a collected first diffraction order in Figure 53. Note that at a large σ_C of 0.95, the sign of $\delta BF/\delta z_9$ switches twice as pitch increases; it has a positive coefficient for dense pitches, a negative coefficient for pitches above 120 nm, and then a positive coefficient again for pitches above 220 nm. When calculating $\delta BF/\delta z_{16}$, the terms with z_9 and z_{25} drop out, and when calculating $\delta BF/\delta z_{25}$, the terms with z_9 and z_{16} drop out [258].

$$\frac{\delta BF}{\delta z_{16}} = C\,\frac{(-1+12{r_0}^2-30{r_0}^4+20{r_0}^6)-(-1+12{r_1}^2-30{r_1}^4+20{r_1}^6)}{({r_0}^2-{r_1}^2)} \qquad (77)$$

$$\frac{\delta \mathrm{BF}}{\delta z_{25}} = C\,\frac{(1-20{r_0}^2+90{r_0}^4-140{r_0}^6+70{r_0}^8)-(1-20{r_1}^2+90{r_1}^4-140{r_1}^6+70{r_1}^8)}{({r_0}^2-{r_1}^2)} \quad (78)$$

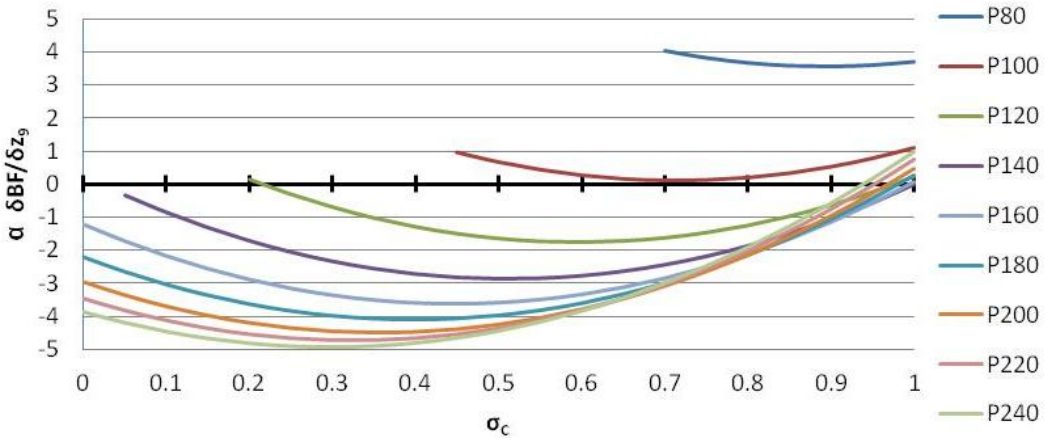

Figure 53: Analytical expression as a function of σ_C for various pitches

This calculation reveals that due to the additive nature of each spherical polynomial, the BF as a function of a certain spherical coefficient has the same slope, regardless of other applied spherical coefficients. The trends due to the analytical expression, shown in Figure 54, match well with those from the rigorous simulator in Figure 51.

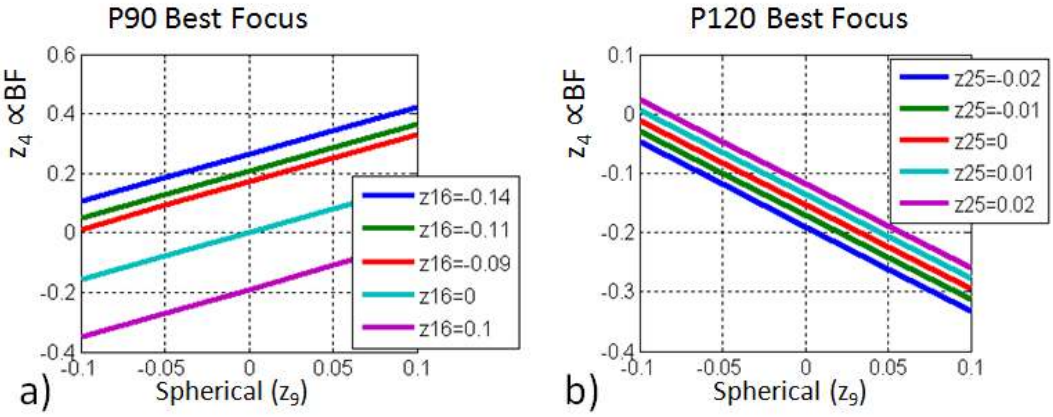

Figure 54: Calculated defocus coefficient, proportional to best focus, is plotted as a function of primary spherical for a) 90 nm pitch and b) 120 nm pitch. The expression's BF has the same slope regardless of higher order applied spherical, similar to the rigorous output shown in Figure 51.

The finding of slope independency suggests that in order to determine the best focus of a given pitch due to spherical coefficients, only two rigorous mask 3D calculations need to be performed. The first rigorous calculation provides the BF offset with no applied wavefront, the second rigorous calculation provides the proportionality constant, then the analytical expression provides the trend of BF as a function of each spherical coefficient. The proportionality constant is equivalent for other pitches, thus requiring only one no-applied-wavefront rigorous calculation for each additional pitch. This procedure is done in section 7.4 in order to find those spherical coefficients which minimize ΔBF over multiple pitches.

6. EXPERIMENTAL

Lithographic exposures were carried out in order to validate process window enhancement by pupil wavefront manipulation. These exposures were completed on a full field immersion scanner equipped with a 193 nm excimer laser source and a 1.35NA projection lens [259]. The test structures were chosen to be one directional (1D) lines, line ends, and aligned contact holes, which are consistent with the industry's expected gridded design rules for the upcoming technology nodes [260].

For the 1D lines, a standard positive-tone resist and development process was used. The resist stack contained 105 nm of a chemically amplified resist comprised of a lactone base polymer, alicyclic protective group, and a fluorosulfonic acid type photo acid generator, above a 95 nm bottom anti-reflective coating with n and k values of 1.82 and 0.34, respectively [261]. The exposed resist was developed with an aqueous tetramethylammonium hydroxide (TMAH) developer without surfactant [262]. Negative tone development (NTD) was used for dots on a 6% AttPSM to print contact holes. The NTD positive-tone resist was comprised of methacrylate copolymers and a triarylsulfonium type photo acid generator [263]. The image reversal during the development step relies on the polarity change at the de-protection reaction, where the unexposed protected polymer with large hydrophobicity is dissolved during development with an organic solvent [263].

The first set of exposures were on an ASML TWINSCAN XT 1900i equipped with the Image Tuner application, which uses lens actuators to apply phase in the pupil

plane according to low order Zernike polynomials [264]. Two masks were exposed: a 6% AttPSM with a 68 nm stack of MoSi, and a binary mask with a 73 nm stack of Cr and CrO. A Y-polarized X-oriented Dipole source with 0.928/0.595 σ settings and a 40° opening angle was used. This illuminator allowed the applied spherical aberration to be sampled within the pupil plane uniquely for different features depending on the orientation of the through-pitch lines, as shown in Figure 55. For vertical features, the diffraction orders sample the pupil radius, and for horizontal features, the diffraction orders sample the pupil edge.

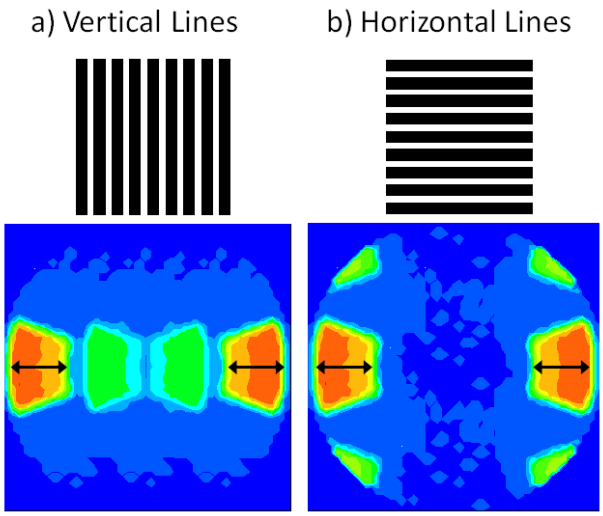

Figure 55: Diffraction pattern from a Y-polarized X-oriented 0.928/0.595/40° dipole source shows the 0th diffraction order in red and the 1st diffraction order in green. Black arrows represent the polarization orientation. For a) vertical lines the diffraction orders are distributed along the radius of the pupil, and for b) horizontal features the diffraction orders are distributed along the edge.

The first wafer was exposed as a focus exposure matrix (FEM) with a wide range of focus and exposure values in order to determine reasonable start and step values. The 6% AttPSM's field size was 32mm x 64mm, so in order to increase the number of dies on the wafer, only the half of the field with the scatterometry modules was exposed. With the notch of the wafer faced down, the exposure was varied along the x axis, increasing

from left to right, and the focus was varied along the y axis, increasing from top to bottom. The center exposure value was $E_{CENTER} = 28$ mJ/cm^2 with a step of $E_{STEP} = 1$ mJ/cm^2. The center focus value was $F_{CENTER} = -40$ nm with a step of $F_{STEP} = 10$ nm. In order create a smooth FEM, each series with a constant focus value was exposed with the same scan direction. This was done by ensuring that as the exposure continued from one row to the next, there was always an odd number difference between columns. An example is shown in Figure 56; when the exposure moves from the first row to the second, the column changes from 6 to 7 which is a difference of one (an odd number), ensuring that all die in the 6th column are exposed with the same scan direction. All following exposures were performed with the same FEM orientation and scan direction aware recipes.

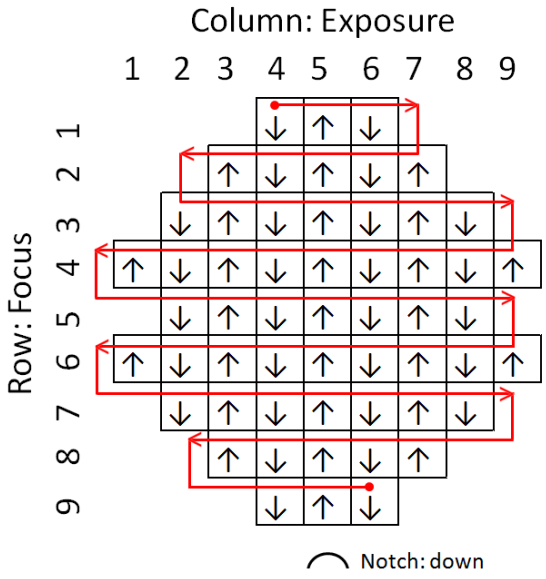

Figure 56: Scan direction aware recipe; exposure order is depicted by the red arrow and scan direction is depicted with black arrows

The center dose and focus values for the next exposures were found by a scanning electron microscope (SEM) observation of a sparse pitch, which tends to have a smaller

DOF since the source was optimized for dense pitches. Using a pitch of 400 nm and a linewidth of 100 nm, an approximate best exposure (BE) of 28 mJ/cm^2 and best focus (BF) of -35 nm were found. An SEM evaluation was also used to select biases for each of the lines through pitch to print at 50 nm with an exposure value of 28 mJ/cm^2, tabulated in Table 3. The next exposures were done on 5 wafers, with FEM parameters of E_{CENTER} = 28 mJ/cm^2, E_{STEP} = 0.4 mJ/cm^2, F_{CENTER} = -35 nm and F_{STEP} = 5 nm. A unique offset of primary spherical aberration was induced on each wafer by the Image Tuner application. This was done by building aberration subrecipes which were attached to the scanner FEM recipe. The 5 exposed FEMs had primary spherical aberration offsets of {-5, -2.5, 0, 2.5, 5}nm, where the offsets are given in units of nm. The converted Zernike coefficients in units of waves are found by dividing by the wavelength; z_9={-0.025, -0.013, 0, 0.013, 0.025}. A unique subrecipe was written for each combination of illumination settings and Zernike coefficients, an example is shown in Figure 57.

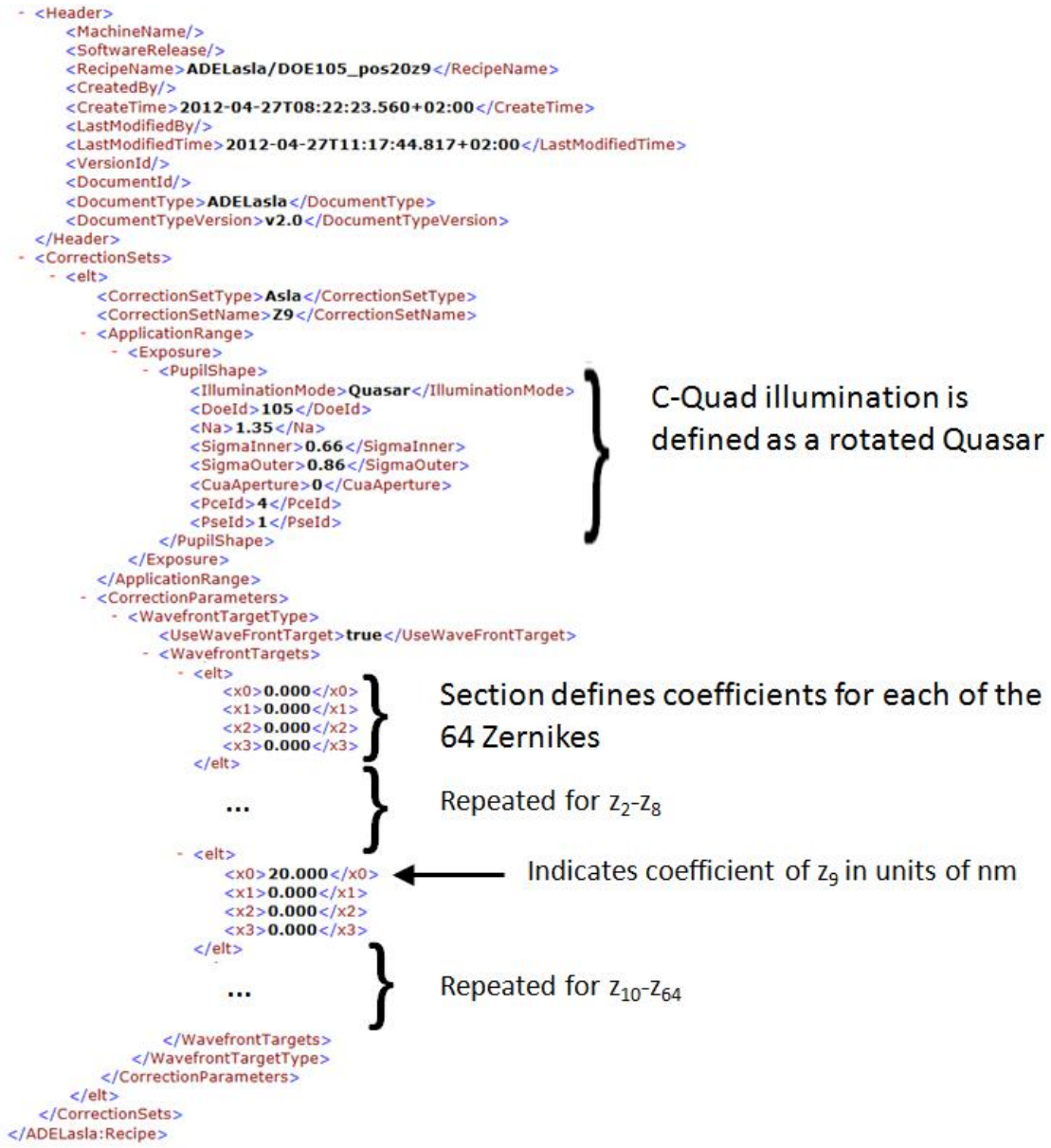

Figure 57: Scanner subrecipe for the application of Zernike offsets, specified in nm

To verify the applied offsets, measurements were completed by the Integrated Lens Interferometer at Scanner (ILIAS) system, which has been previously characterized [265], [266]. The test was completed on dummy wafers during an exposure with constant dose and focus. It measured an aberration fingerprint before and after each wafer in a lot of at least 3 wafers, immediately following the reticle alignment procedure. The measurement recipe, called the Lens Heating ILIAS Qualification (LHIQ), applies the

specified subrecipes and then scans at 7 points in the slit to extract Zernikes, which are reported in units of nm. The actual offsets were measured to be {-4.97, -2.20, 0, 2.34, 4.74}nm.

The scatterometry modules of the mask were exposed to allow fast metrology measurements using YieldStar^{TM} S-200, which has shown good correlation to measurements on an SEM [267]. Scatterometry modules are larger than SEM modules, usually 40 μm x 40 μm, to allow a large region for the incident light. The YieldStar recipe requires knowledge of the geometry of the features, such as approximate pitch, linewidth, height, and sidewall angle, then measures the amplitude of the scattered light from the module to determine accurate duty ratio and thus linewidth values. For the 6% AttPSM line end measurements, only every other column on the FEM was measured since the YieldStar is much slower on 2D structures than on 1D structures.

A similar procedure was followed for the binary mask, where the first exposure was completed with E_{CENTER} = 28 mJ/cm^2, E_{STEP} = 1 mJ/cm^2, F_{CENTER} = -40 nm and F_{STEP} = 20 nm. The SEM inspection of sparse 400 nm pitch at both horizontal and vertical orientations, determined an approximate BE of 22 mJ/cm^2 and a BF of -40 nm. In order to print close to the target of 50 nm lines, the largest available biases on the mask were selected, which are tabulated in Table 3. The next exposures were completed on 5 wafers with subrecipes z_9={-0.025, -0.013, 0, 0.013, 0.025} and FEM settings of E_{CENTER} = 22 mJ/cm^2, E_{STEP} = 0.5 mJ/cm^2, F_{CENTER} = -40 nm and F_{STEP} = 10 nm. Metrology was completed on the scatterometry modules by the Yieldstar.

Table 3: Mask biases through pitch

Binary		Thin MoSi AttPSM						ThickTaSiON AttPSM				AltPSM	
1D Lines		1D Lines		Line Ends		2D Dots		1D Lines		Line Ends		1D Lines	
Pitch	Mask LW	Pitch	Mask LW	Pitch	Mask LW	Pitch	Mask Diameter	Pitch	Mask LW	Pitch	Mask LW	Pitch	Mask LW
170V	71	160V	72	250	90	90	58	84	25.5	100	38	115	59
220V	89	240V	90	300	100	100	64	90	30.5	120	50	125	59
280V	98	280V	96	350	100	110	72	100	35.5	140	59	150	59
320V	103	320V	98			120	78	110	40.5	160	65	200	59
350V	105	360V	100					135	51	180	75		
240H	93	220H	98					180	85				
260H	90	240H	98										
280H	89	260H	96										
300H	91	280H	94										
400H	94	300H	92										

The second set of exposures were completed with an ASML TWINSCAN XT 1950i, equipped with FlexWave, a high resolution wavefront manipulator. FlexWave is comprised of an optical element near the pupil plane containing a grid of conductive and resistive structures, as shown in Figure 58 [139]. These structures can be locally heated to create unique aberration fingerprints up to the 64th Zernike polynomial. In these experiments, only primary and secondary spherical aberration offsets were applied, based on the MKS algorithm results that converged to small values of z_{25} and z_{36}. The capabilities of Flexwave allowed the magnitude of the applied aberration to be 4x the amount applied by Image Tuner in the previous round of exposures. Three masks were exposed: aligned dots on a 6% 68 nm MoSi AttPSM, a 1% AttPSM with a mask absorber made up of 34 nm Ta under 113.5 nm SiON, and an AltPSM with a 73 nm Cr/CrO absorber and a 171 nm etch into the amorphous fused silica substrate. An XY polarized C-Quad source with 0.86/0.66 σ settings and a 30° opening angle was used with the AttPSMs. An XY polarized conventional source with a 0.3 σ was used with the AltPSM. All metrology was completed on a SEM due to no availability of scatterometry modules on the masks.

The first wafer exposed with the 1% TaSiON AttPSM was completed with FEM parameters of E_{CENTER} = 28 mJ/cm^2, E_{STEP} = 1 mJ/cm^2, F_{CENTER} = 0 nm and F_{STEP} = 10 nm. SEM evaluation of a sparse pitch found an approximate BE of 28 and BF of -30 nm, so the following exposures were completed with FEM parameters of E_{CENTER} = 28 mJ/cm^2, E_{STEP} = 0.5 mJ/cm^2, F_{CENTER} = -30 nm and F_{STEP} = 15 nm. The lines through pitch on the TaSiON mask were biased, as shown in Table 3, so that they would print as 45 nm at the same best exposure, except for the 180 nm pitch that had a linewidth target of 90 nm. Since experimental BF as a function of primary spherical coefficient was observed to be linear in the previous round of exposures, only 3 wafers through z_9 were exposed: z_9={-0.1, 0, 0.1}. An additional wafer with a positive amount of secondary spherical aberration was exposed in order to quantify the BF shifts as a function of z_{16}. This wafer had applied offsets of z_9= +0.05 and z_{16}= +0.06. A final "solution" wafer with the applied offsets to maximize UDOF was exposed: z_9=0.02 and z_{16}=0.06. The method used to determine the necessary applied wavefront correction will be discussed in the next section.

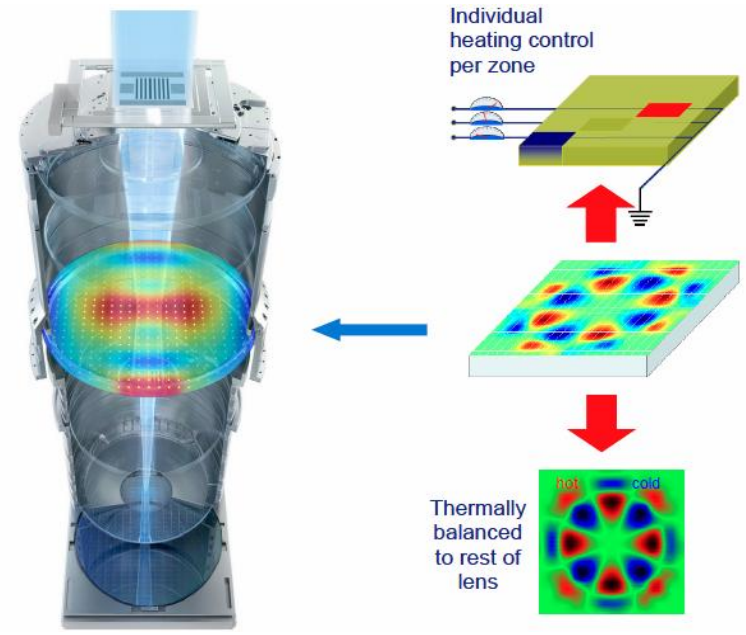

Figure 58: Schematic of FlexWave, a high resolution wavefront manipulator

The estimation of BE and BF for the line ends on the 1% TaSiON AttPSM was completed on the same wafer exposed for the 1D lines. The BE was found to be around 30 mJ/cm^2, so the next exposures were performed with E_{CENTER} = 30 mJ/cm^2, E_{STEP} = 1 mJ/cm^2, F_{CENTER} = -10 nm and F_{STEP} = 15 nm. The module with no serifs were measured, where the gap was the smallest that would print without bridging. These gaps were 45 nm for pitches of 100 and 120 nm, and a gap of 42.5 nm for pitches of 140, 160, and 180 nm. The gap and CD were measured from the same screen capture using the CD2D measurement algorithm on the SEM. The gap was measured by fitting a parabola to each line end to define each end point, and then calculating the distance between end points only along one axis, as shown in Figure 59. Exposures with a FlexWave astigmatism application of offsets z_5= -0.1 and z_5=+0.05 were completed on two separate wafers.

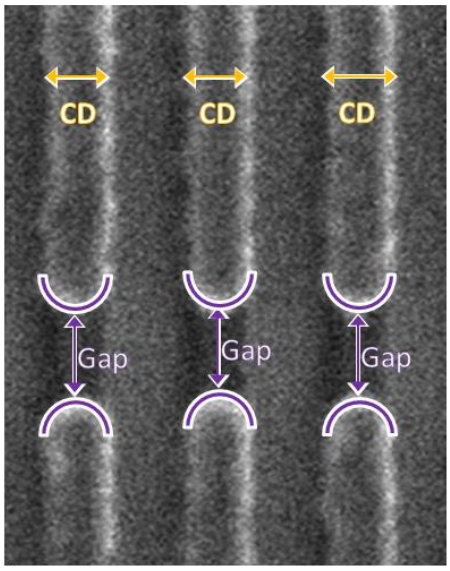

Figure 59: Line end measurement procedure of CD and gap

The first wafer exposed with the contact holes on the 6% MoSi AttPSM was completed with FEM parameters of $E_{CENTER} = 31$ mJ/cm^2, $E_{STEP} = 0.5$ mJ/cm^2, $F_{CENTER} = -30$ nm and $F_{STEP} = 15$ nm. The BE was found to be around 31 mJ/cm^2 and the BF close to -30 nm, so the next exposures were performed with the same FEM settings. Averaging is crucial for contact holes due to the variability in SEM contour measurements, thus two subfields kitty-corner across the exposure field were both included in the measurement. In order to characterize the BF shifts as a function of secondary spherical aberration, an additional wafer with offsets of $z_9 = -0.05$ and $z_{16} = -0.12$ was exposed. A final "solution" wafer with the applied offsets to maximize UDOF was exposed with offsets of $z_9 = -0.01$ and $z_{16} = -0.1$.

The AltPSM was fabricated by a dry etch C_2F_6 chemistry, which generally forms straight sidewalls in the fused silica substrate [268]. The features were biased 18 nm per Cr edge on mask, equivalent to a bias of 9 nm per line on wafer. The first wafer exposed with the AltPSM was completed with FEM parameters of $E_{CENTER} = 24$ mJ/cm^2,

E_{STEP} = 0.4 mJ/cm^2, F_{CENTER} = -30 nm and F_{STEP} = 15 nm. Inspection revealed a BE of around 24 mJ/cm^2 and a BF that was shifted negative, so subsequent wafers were exposed with FEM settings of E_{CENTER} = 24 mJ/cm^2, E_{STEP} = 0.5 mJ/cm^2, F_{CENTER} = -60 nm and F_{STEP} = 15 nm.

Since the measurement of the shifted spaces had to be separate from the measurement of the unshifted spaces, the metrology recipe was built accordingly. The mask's module comprised of 8 lines with the substrate un-etched in the center. The SEM alignment procedure first performed a pattern recognition at the ends of the lines, where the etched spaces connected to the unetched substrate resulting in a printing connection line, as shown in Figure 60. Then a vertical movement was performed so the measurement was done away from the connection lines. This procedure guaranteed that when the measurements were performed, the first CD from the left was a line, the second CD was a shifted space, and the fourth CD was an unshifted space, as depicted in Figure 61. Two exposures with subrecipes of z_9= -0.09 and both z_9= -0.08 and z_{16}=+0.1 were completed based on simulations that suggest a large amount of both primary and secondary aberration for compensation [269].

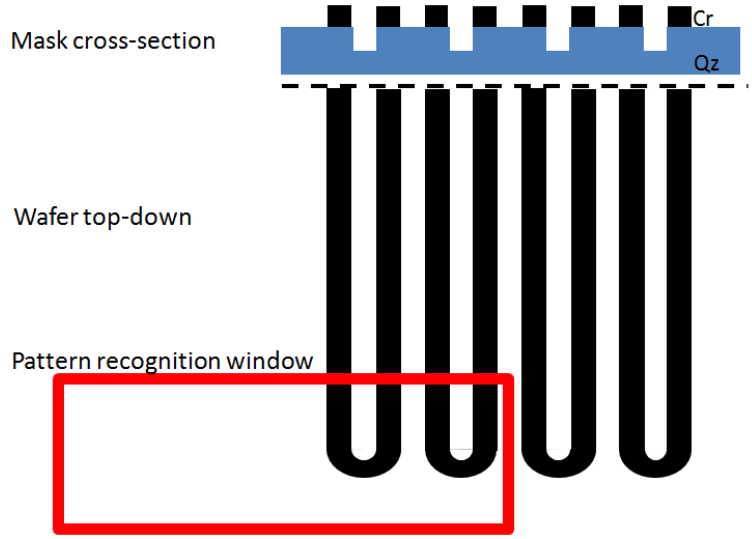

Figure 60: SEM alignment on AltPSM

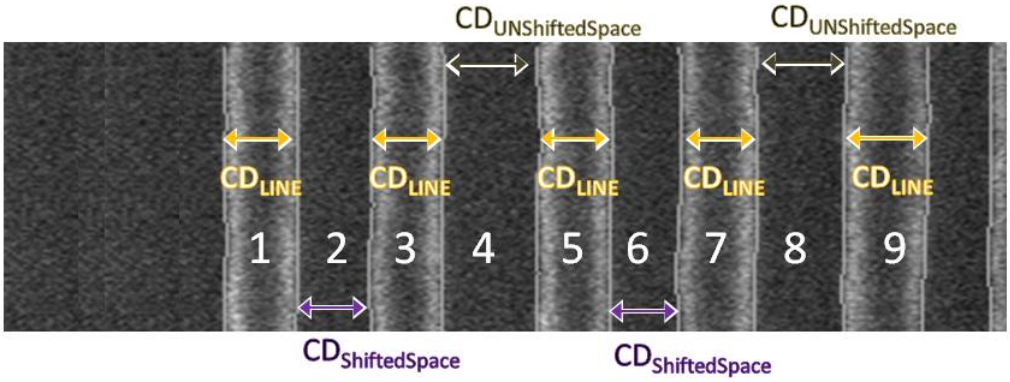

Figure 61: CD definitions on image from AltPSM. Metrology recipe guarantees that 2nd CD will be shifted space and 4th CD will be an unshifted space.

For each of the FlexWave applied subrecipes, a measurement was taken with the ILIAS system for validation. The measurements did not require a mask or a wafer to be in the scanner, were taken at 12 points through the slit, and were reported in units of nm as 'after - before' application for each of the 64 Zernikes. Repeatability was verified by performing three tests and extracting the average values from the center of the slit, 3 slit positions, and all slit positions. In Figure 62, the measured offsets have been converted to waves for a negative astigmatism application of z_5= -0.1. All higher order Zernikes were measured to be less than ±0.004 waves.

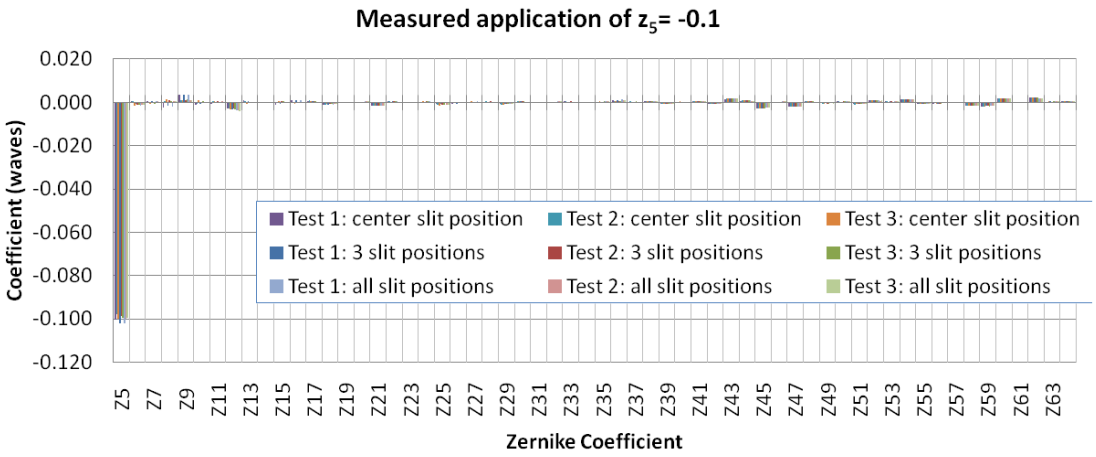

Figure 62: Measured FlexWave coefficients with an astigmatism application of z_5= -0.1 for multiple tests and at multiple slit locations

Flexwave was also successful in creating wavefronts with multiple applied Zernike offsets. The measured coefficients from the subrecipe of the TaSiON solution wafer with applied z_9 =+0.02 and z_{16} =+0.06 is shown in Figure 63. These values were averaged from 3 slit positions, and have all other order Zernikes within ±0.0033 waves.

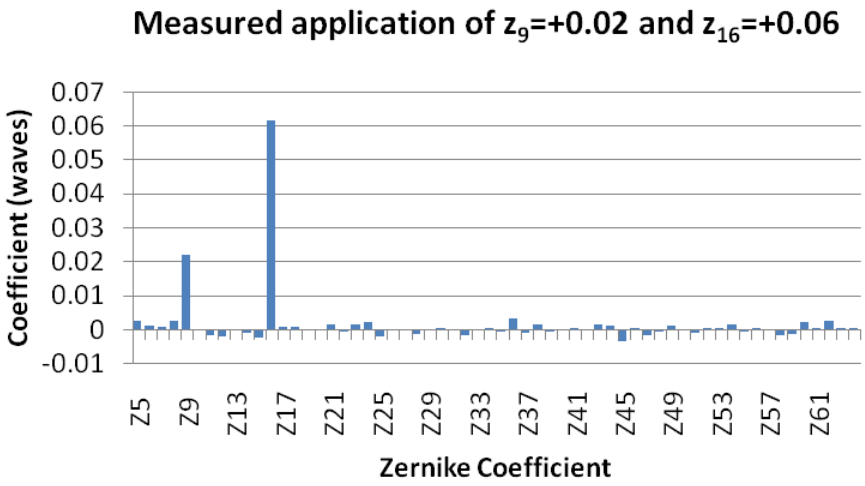

Figure 63: Measured FlexWave coefficients with an application of z_9=+0.02 and z_{16}=+0.06

The CD versus focus and exposure values were imported into KLA-Tencor PRODATA™ to extract the BF and DOF [270]. In Figure 64a, the FEM is plotted for a 110 nm pitch on the TaSiON mask. The process window without any data model is

shown in Figure 64b, with a CD specification of ±10%. In order to make the process windows appear smoother, a polynomial function data model was used on all the FEM. The FEM with the polynomial fit is shown in Figure 64c, and the corresponding process window is shown in Figure 64d. The polynomial data model reduces the effects from outliers and FEM variability. The BF and DOF are extracted from the Dose versus Focus plot as was discussed in Figure 3. An exposure latitude of 10% was used for all features, except 3% for the line ends, which had a limited DOF since the targets were set to as drawn on the mask. The difference between the process window with no data model and the process window with the polynomial fit can produce slight differences in the BF, such as the 10 nm difference seen in Figure 64c and d.

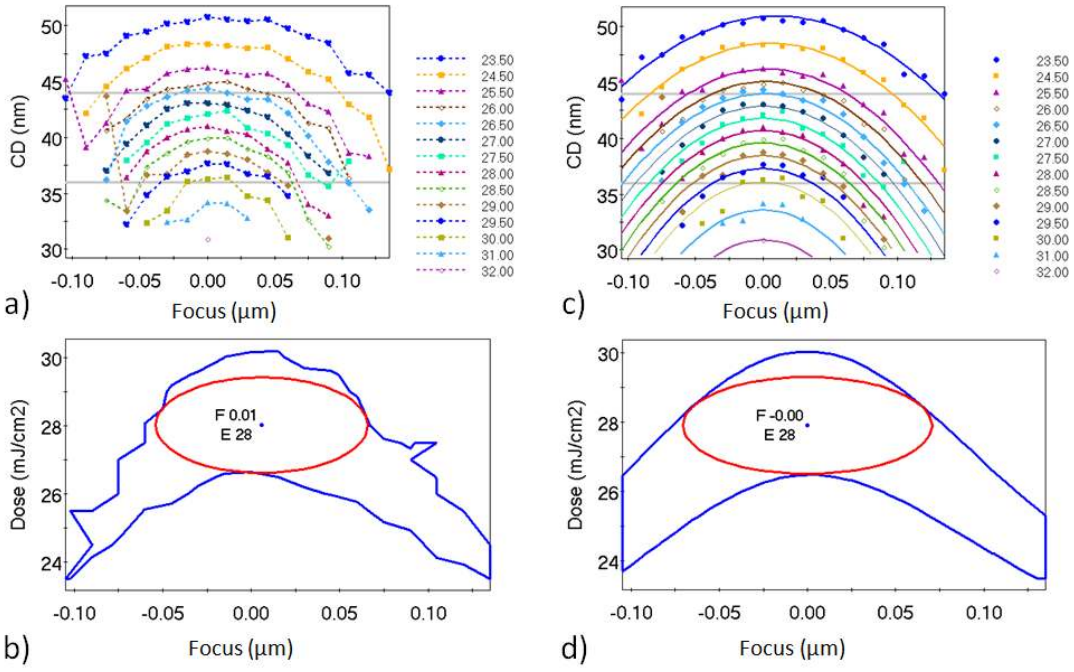

Figure 64: Process window calculation for a 110 nm pitch on 1% TaSiON AttPSM with applied z_9 = -0.1. No data model a) FEM and b) process window has BF=+10 nm. Polynomial function data model c) FEM and d) process window has BF= 0 nm.

The UDOF over multiple features was found by collecting multiple process windows and finding the overlapping area, also completed with the PRODATA^{TM}

software. Experimental process windows for the contact holes on a 6% MoSi AttPSM are shown in Figure 65, with good correlation to the rigorous simulation. The discrepancy in dose is due to the non-calibrated physical resist model.

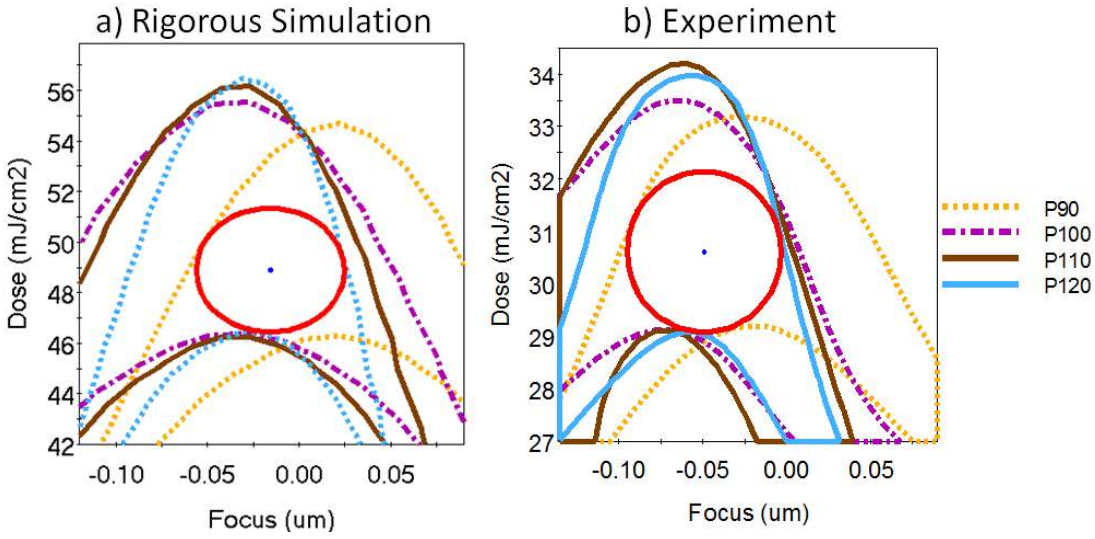

Figure 65: Process windows for contact holes through pitch on a 6% MoSi AttPSM with no applied wavefront in a) simulation and b) experiment

7. RESULTS AND DISCUSSION

7.1 Lines and spaces on a thin AttPSM

The influence of spherical aberration on the tilt of the FEM was observed in the data. For example, Figure 66a shows the process window for a vertical pitch of 160 nm on the 6% AttPSM at both a spherical aberration offset of -0.025 and +0.025. Note that the P160V in Figure 66a refers to a vertical pitch of 160 nm. The process window shows a larger linear tilt at the negative value when compared to the positive offset of spherical aberration. The FEM tilt was quantified by fitting a polynomial to the process window and extracting the linear coefficient as the tilt. Extracted tilt as a function of z_9 for several vertical pitches is shown to be pitch dependent in Figure 66b. The FEM tilt tends to be higher with a negative value of spherical aberration. For the large pitches of 280 and 400 nm, the FEM tilt remains low even with an offset of -0.025. This is due to the location of the diffraction orders in the pupil plane relative to the fingerprint of spherical aberration. For these pitches with the above mentioned dipole illumination, the zero and first orders lie symmetric about spherical aberration's minimum. The effect from spherical is reduced since similar phases are induced on the orders. For the 160 nm pitch, the first diffraction order is near the middle of the pupil, which is a maximum in spherical aberration's fingerprint, so it sees a higher phase value than the zero diffraction order, leading to a larger FEM tilt effect [269].

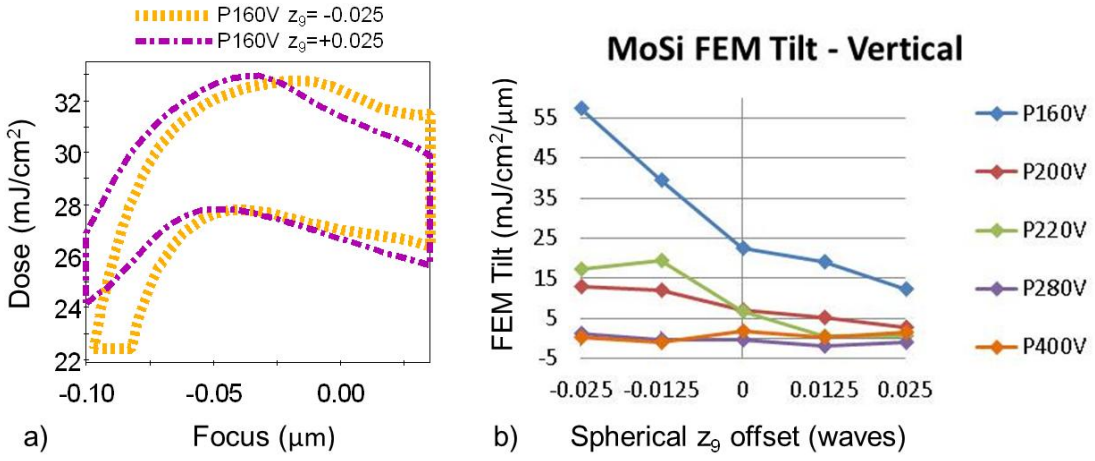

Figure 66: a) Experimental process window for vertical pitch of 160 nm at an applied spherical aberration offset of -0.025 is more tilted than that of +0.025. b) Extracted tilt for a variety of vertical pitches tends to be higher at a negative applied spherical offset.

Figure 67a shows the process window for a horizontal pitch of 170 nm at both a spherical offset of -0.025 and +0.025. The process window shows a higher tilt at the positive z_9 value compared to the negative z_9 value. Extracted tilt values for several horizontal pitches are shown in Figure 67b. The FEM tilt tends to be higher at a positive value of spherical aberration. The FEM tilt of horizontal pitches has the opposite relationship to spherical than vertical pitches due to the location of the diffraction orders in the pupil. For vertical pitches, the first diffraction orders lie along the radius of the pupil, whereas for horizontal pitches the first diffraction orders lie along the edge of the pupil. Spherical aberration has the opposite slope in these two regions, resulting in the opposite FEM tilt tendency. The FEM tilt trend for horizontal pitches is similar through pitch because the first diffraction order is always at a similar pupil radius as the zero diffraction order.

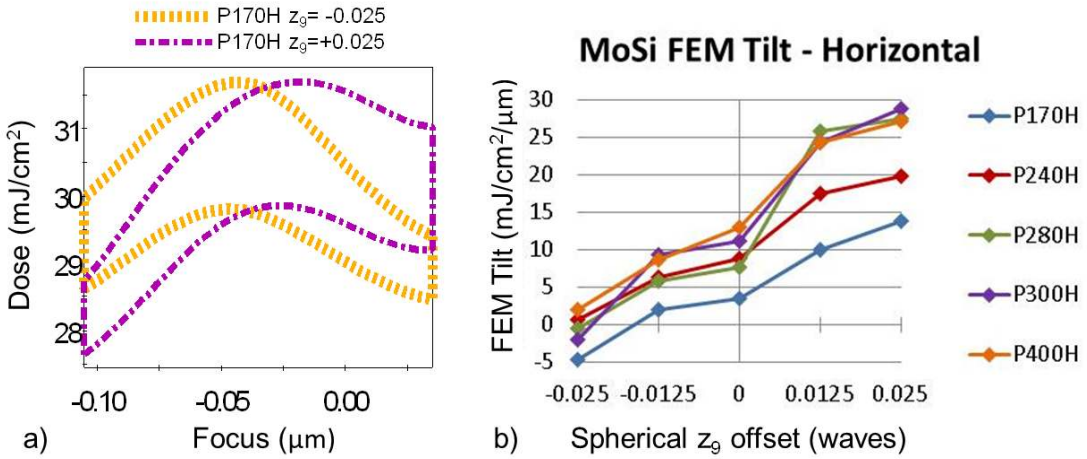

Figure 67: a) Experimental process window for horizontal pitch of 170 nm at an applied spherical aberration offset of +0.025 is more tilted than that of -0.025. b) Extracted tilt for a variety of pitches tends to be higher at a positive spherical aberration offset.

Applied spherical aberration results in a best focus shift, which depends on the pitch and orientation of the features. Figure 68a shows that the best focus for a vertical pitch of 280 nm shifts negative with a positive applied spherical aberration offset. Figure 68b shows that the best focus for a horizontal pitch of 280 nm shifts in the opposite direction. Again, this is due to the different regions of spherical that the first diffraction orders encounter, which have the opposite slope.

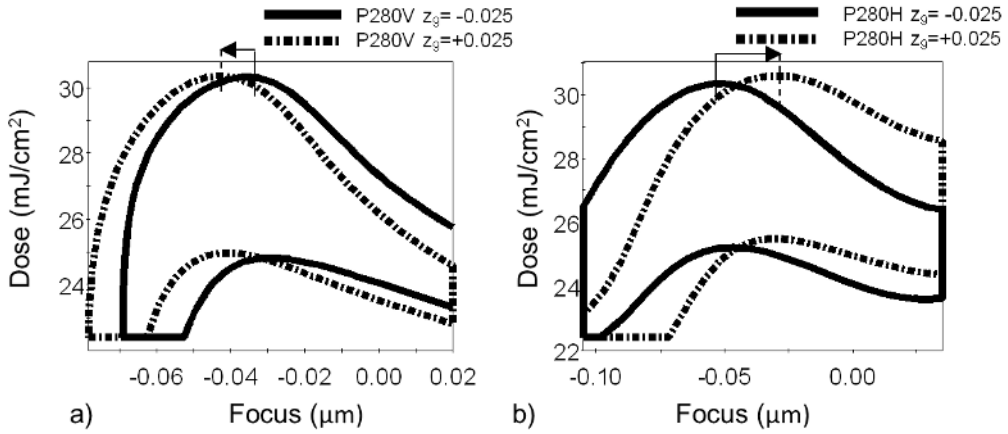

Figure 68: Process windows for a) vertical pitch of 280 nm shift negative in focus and for b) horizontal pitch of 280 nm shift positive in focus with an increasing spherical aberration offset.

The experimental best focus for several pitches is plotted with simulated values for both orientations in Figure 70. The simulation predicts a linear relationship between best focus and spherical. The experimental best focus is plotted together with linear regression for the vertical orientation in Figure 69. Note that the data for each offset of spherical aberration was taken on different wafers. Removing the data from the $z_9 = 0$ wafer increases the average trend line R^2 value from 0.73 to 0.95, suggesting that the $z_9 = 0$ wafer may be an outlier.

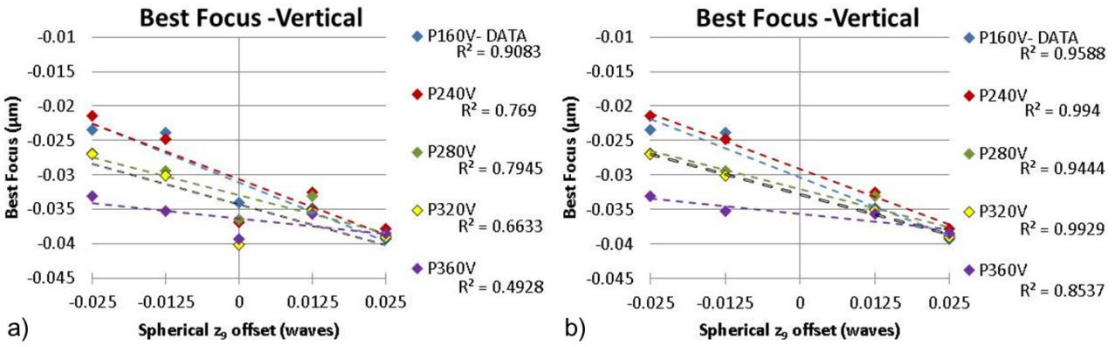

Figure 69: Experimental best focus (points) for vertical pitches is plotted with linear regression (dotted lines). a) The average R^2 value is 0.73 and b) without $z_9 = 0$ data the average R^2 value increased to 0.95.

In Figure 70, both the experimental best focus (points) and the rigorously simulated best focus (lines) are plotted as a function of spherical offset for vertical and horizontal features. The slope of BF as a function of the offset of spherical aberration, $\delta BF/\delta z_9$, was dependent on both pitch and orientation. For vertical pitches, the $\delta BF/\delta z_9$ slope is negative and pitch dependent, and the ΔBF is minimized by the positive offset of spherical that also minimized FEM tilt in Figure 66b. For horizontal pitches, the $\delta BF/\delta z_9$ slope is positive and constant through pitch, which leads to a constant ΔBF through pitch. This difference is due to the different radial locations of the diffraction orders and is predicted correctly by the analytical expression, shown in Figure 70b and d. For

horizontal pitches imaged with an X-oriented dipole, the diffraction orders are distributed along the edge of the pupil, rather than along the radius, so the radial locations become

$$r_{\pm 1} = \sqrt{\left(\frac{\lambda}{NA \cdot P}\right)^2 + \sigma^2} \tag{79}$$

and thus do not vary as much through pitch as those for the vertical pitches. This leads to a smaller effect of spherical aberration on horizontal pitches as compared to the vertical pitches. In fact, the relationship of BF to spherical coefficient looks more like defocus (constant through pitch) than spherical due to the limited radial sampling, shown in Figure 70c and d.

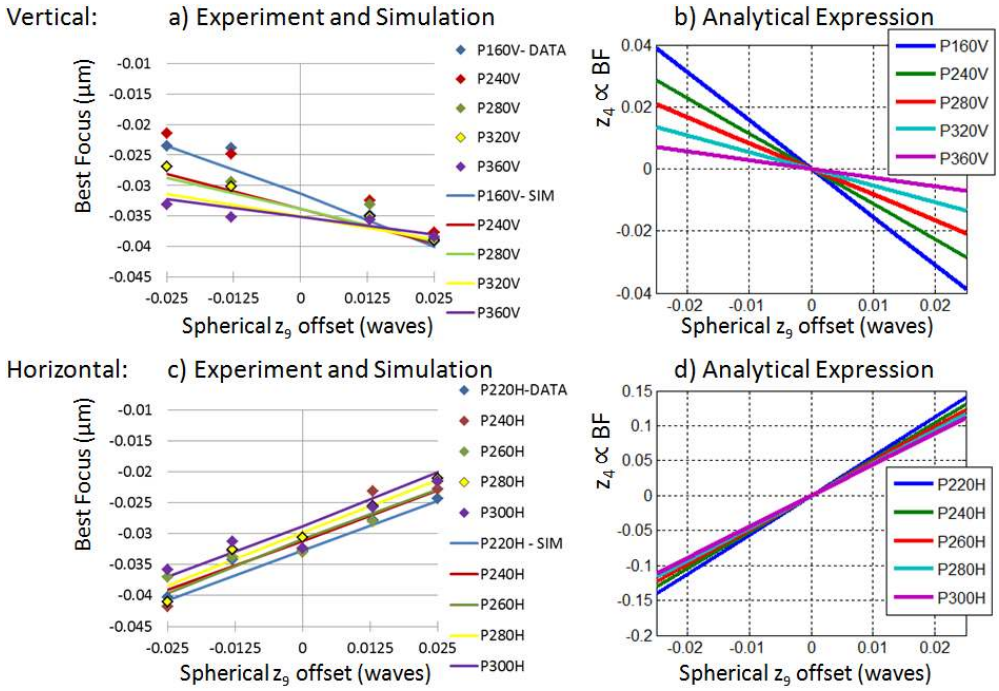

Figure 70: BF as a function of primary spherical offset for vertical lines in a) experiment and rigorous simulation and b) from the analytical expression, and for horizontal lines in c) experiment and rigorous simulation and d) from the analytical expression. The analytical expression correctly predicts the pitch and orientation dependent trends; spherical effect is minimal for horizontal lines due to limited radial sampling.

7.2 Lines and spaces on a thin binary mask

The experimental best focus for the exposures on a binary mask is plotted with rigorous simulation in Figure 71. The zero z_9 data for the vertical pitches was removed, increasing the average R^2 from a trend line from 0.39 to 0.92. The best focus through spherical slope is similar to the AttPSM; negative slope for vertical pitches and positive slope for horizontal pitches. The ΔBF for vertical pitches is minimized with a positive value of spherical and the horizontal pitches reveal less spherical effect due to limited radial sampling of the pupil.

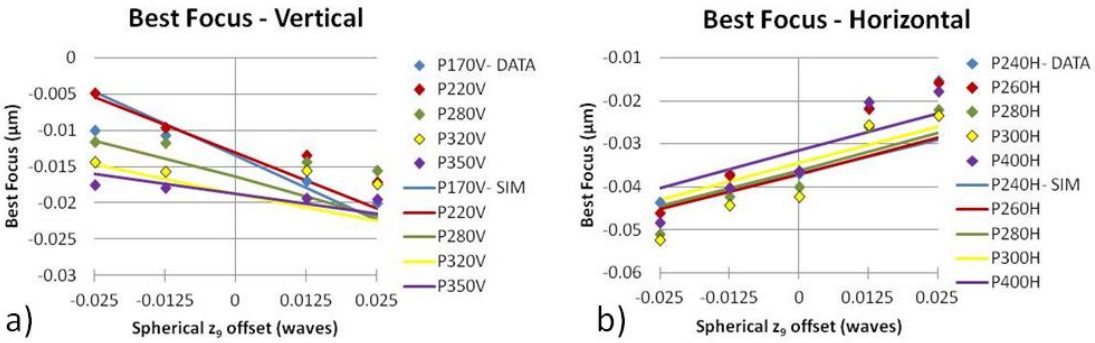

Figure 71: Experimental best focus of binary mask is plotted with simulated values for a) vertical pitches, where pitch dependent best focus characteristic of spherical is present and for b) horizontal pitches, where spherical effect is minimal due to less pupil radius values probed through pitch.

7.3 Line ends on a thin AttPSM

The best focus was measured for the CD and length of line end features on the 6% AttPSM, shown in Figure 72. The influence of spherical can be seen as the pitch dependent slope of BF. Similar to the 6% AttPSM vertical pitches, the ΔBF is reduced with a positive amount of spherical aberration. For both the binary and AttPSM masks, the UDOF is not degraded by mask topography effects since the small ΔBF allows the UDOF to be only limited by the feature with the smallest DOF. This demonstrates why industry has trended towards the use of these thin masks.

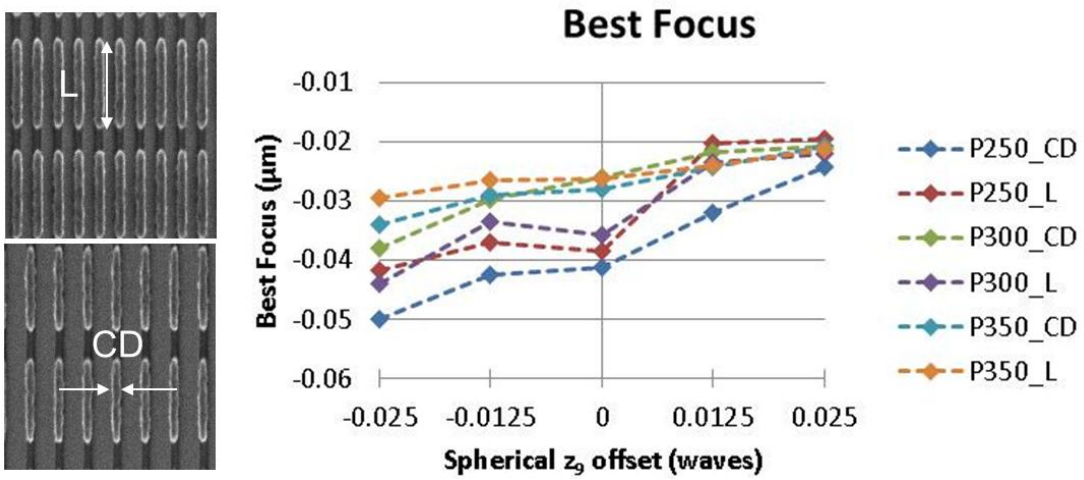

Figure 72: Experimental best focus for 6% MoSi AttPSM vertical line ends. Both the CD and length of the line ends are plotted.

7.4 Lines and spaces on a thick AttPSM

Simulated and experimental best focus as a function of z_9 for the 1% TaSiON AttPSM are plotted in Figure 73 [271]. The experimental BF with no applied offsets, BF_0, correspond to those charted in Figure 16. The ΔBF of 64 nm in experiment matches well with simulation. The simulation captures the decreasing $\delta BF/\delta z_9$ slope through pitch, as well as the unintuitive twist that occurs around a pitch of 110 nm; the slope switches sign.

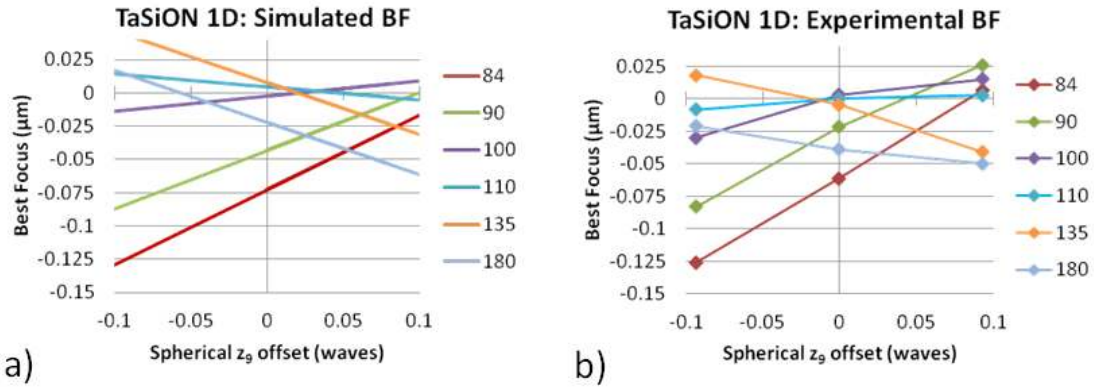

Figure 73: Best focus versus z_9 offset through pitch for 1D lines on a 1% transmitting TaSiON AttPSM in a) simulation and b) experiment

The analytical expression derived in section 5.3 can be used to understand why this switch in slope occurs. To reiterate, the BF shift is proportional to the coefficient of a

quadratic fitted to the phases induced on the diffraction orders due to spherical aberration [258]. The fitted defocus due to a positive applied spherical aberration is depicted in Figure 74 for pitches of 84 and 135 nm. Note that the P84 in Figure 74 refers to a pitch of 84 nm. Based on the different radial location of the 1st diffraction order, the fitted quadratic for the 84 nm pitch has a positive coefficient, whereas it has a negative coefficient for the 135 nm pitch, resulting in the opposite sign of $\delta BF/\delta z_9$ slope.

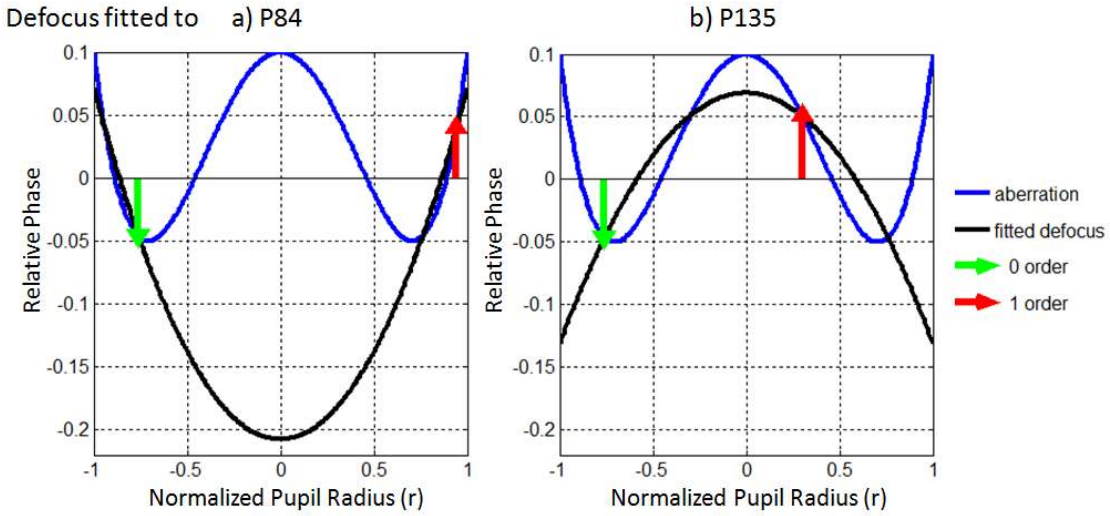

Figure 74: For a positive applied primary spherical, the coefficient of defocus fitted to a) a pitch of 84 nm is positive and to b) a pitch of 135 nm is negative, resulting in the opposite sign of $\delta BF/\delta z_9$

The $\delta BF/\delta z_{16}$ was extracted from the experimental data through z_{16} shown in Figure 75. The experimental slopes are tabulated with those calculated from Equations 76 and 77 in Table 4. The constant, *C* of Equations 76 and 77, was found by normalizing to the pitch which gave the smallest standard deviation between the expression and the simulation; 90 nm pitch for $\delta BF/\delta z_9$ and 100 nm pitch for $\delta BF/\delta z_{16}$.

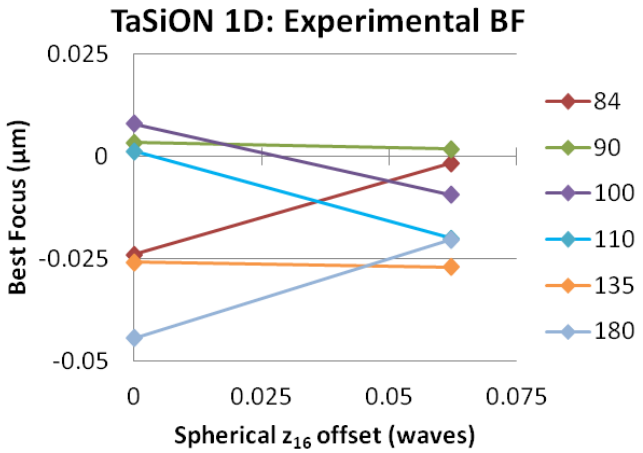

Figure 75: Experimental best focus versus z_{16} offset from which to calculate experimental $\delta BF/\delta z_{16}$. These experimental wafers also had an applied z_9= +0.05.

Table 4: Experimentally measured, rigorously simulated, and analytically calculated values for $\delta BF/\delta z_9$ and $\delta BF/\delta z_{16}$ through pitch

$\delta BF/\delta z_n$	Primary spherical (z_9)			Primary spherical (z_{16})		
Pitch	Experimental	Simulation	Model	Exp	Sim	Model
84	0.6369	0.5625	0.725920331	0.3667	0.35	0.579032523
90	0.5211	0.4375	0.4375	-0.0193	-0.07	-0.17292771
100	0.2123	0.1141	0.103729882	-0.2895	-0.5638	-0.5638
110	0.0579	-0.0984	-0.108612875	-0.3474	-0.5575	-0.510231538
135	-0.2895	-0.3891	-0.357402726	-0.0193	-0.095	-0.029870065
180	-0.1351	-0.392	-0.414514861	0.386	0.2264	0.431467141

The analytic expression for $\delta BF/\delta z_9$ is plotted with rigorous simulation and experiment in Figure 76. The analytical expression, shown as a solid line, represents the values through pitch at a σ_C of 0.76 shown in Figure 53. The good matching between the expression and simulation shows that the analytical expression provides fundamental understanding of the effect of spherical aberration, while only requiring two computationally expensive rigorous simulations which provide the proportionality constant. Note that the accuracy of the analytical expression breaks down at the smallest pitches, revealing that the small angle approximation used for first order defocus breaks down at high NA.

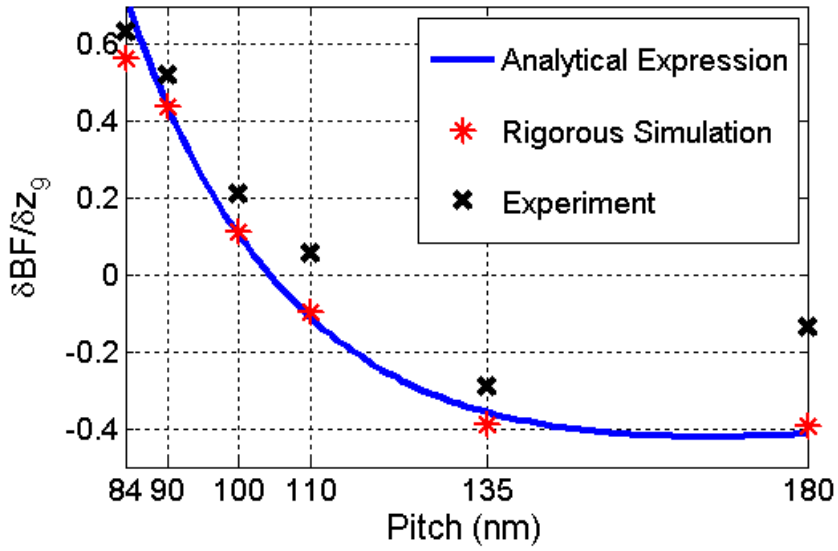

Figure 76: $\delta BF/\delta z_9$ slope through pitch matches well between the analytical expression and the rigorous simulation.

The significant trends between the experiment and the analytical expression match, such as the only pitches which have a positive $\delta BF/\delta z_{16}$ are 84 nm and 180 nm. However, the experimental slopes tend to be larger than the simulated and analytically calculated slopes. This discrepancy can be attributed to FEM measurement error since each experimental BF was taken from a single trial and was not repeated for averaging. Each FEM was exposed over one whole wafer, so edge effects may have an influence on the FEM and the resulting slopes. The simulation accuracy could be further improved by calibrating the resist model through z_9, similar to the way an OPC resist model is calibrated through defocus.

Not only is there a difference between experimental and simulated slopes, but there is also a difference between experimental and simulated BF with no applied offsets (BF_0). This means that the optimized simulated solution of z_9=+0.05 and z_{16}=+0.08 found by the MKS algorithm does not represent the best experimental compensating wavefront. Thus, the experimental solutions were found by interpolating for the minimum ΔBF using the experimental $\delta BF/\delta z_9$ and $\delta BF/\delta z_{16}$. The BF for a certain pitch as a function of the z_9

and z_{16} offsets can be defined in terms of the experimental BF_0 and the BF slopes for that pitch.

$$BF_{P84}(z_9, z_{16}) = BF_{0_{P84}} + \frac{\delta BF_{P84}}{\delta z_9} \cdot z_9 + \frac{\delta BF_{P84}}{\delta z_{16}} \cdot z_{16} \quad (80)$$

$$BF_{P90}(z_9, z_{16}) = BF_{0_{P90}} + \frac{\delta BF_{P90}}{\delta z_9} \cdot z_9 + \frac{\delta BF_{P90}}{\delta z_{16}} \cdot z_{16} \quad (81)$$

$$BF_{P100}(z_9, z_{16}) = BF_{0_{P100}} + \frac{\delta BF_{P100}}{\delta z_9} \cdot z_9 + \frac{\delta BF_{P100}}{\delta z_{16}} \cdot z_{16} \quad (82)$$

$$BF_{P110}(z_9, z_{16}) = BF_{0_{P110}} + \frac{\delta BF_{P110}}{\delta z_9} \cdot z_9 + \frac{\delta BF_{P110}}{\delta z_{16}} \cdot z_{16} \quad (83)$$

$$BF_{P135}(z_9, z_{16}) = BF_{0_{P135}} + \frac{\delta BF_{P135}}{\delta z_9} \cdot z_9 + \frac{\delta BF_{P135}}{\delta z_{16}} \cdot z_{16} \quad (84)$$

$$BF_{P180}(z_9, z_{16}) = BF_{0_{P180}} + \frac{\delta BF_{P180}}{\delta z_9} \cdot z_9 + \frac{\delta BF_{P180}}{\delta z_{16}} \cdot z_{16} \quad (85)$$

The ΔBF then becomes the range in Best Focus at each z_9 and z_{16} offset.

$$\Delta BF(z_9, z_{16}) = range[BF_{P84}(z_9, z_{16}), BF_{P90}(z_9, z_{16}), BF_{P100}(z_9, z_{16}),$$
$$BF_{P110}(z_9, z_{16}), BF_{P135}(z_9, z_{16}), BF_{P180}(z_9, z_{16})] \quad (86)$$

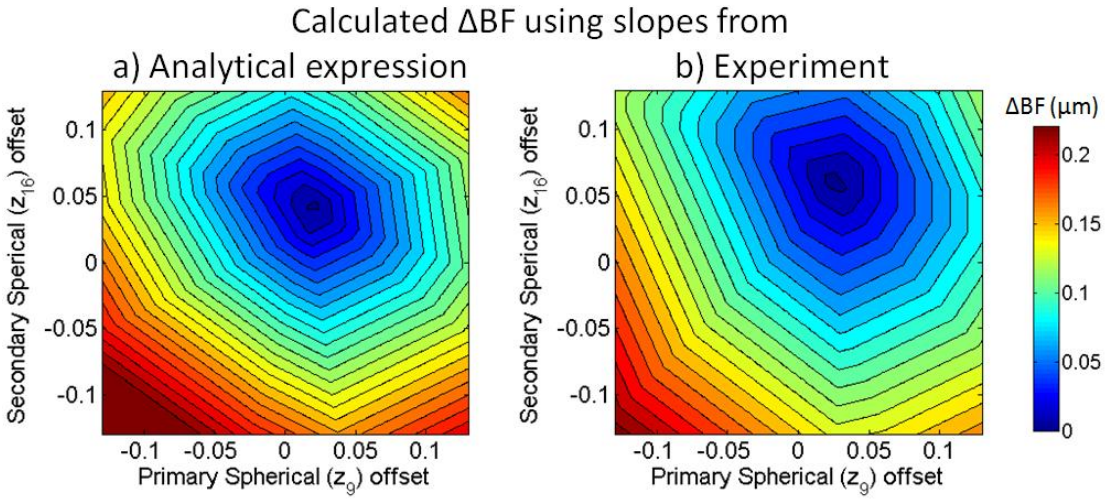

Figure 77: Extrapolation for ΔBF over pitches of 84, 90, 100, 110, 135, and 180 nm using a) slopes from analytical expression has a minimum at z_9=+0.0217 and z_{16}=+0.0442 and using b) experimental slopes has a minimum at z_9=+0.0234 and z_{16}=+0.0624

The calculated ΔBF as a function of z_9 and z_{16} is shown in Figure 77 from both the analytically calculated slopes as well as the experimental slopes. The compensating wavefront with the minimum ΔBF using the slopes from the analytical expression had a primary spherical aberration offset of z_9=+0.0217 and a secondary spherical aberration offset of z_{16}=+0.0442. The compensating wavefront using the experimental slopes had a primary spherical aberration offset of z_9=+0.0234 and a secondary spherical aberration offset of z_{16}=+0.0624. The experimental process windows are shown in Figure 78 as the uncorrected case along with the compensating wavefront of z_9=+0.02 and z_{16}=+0.06. With no applied offsets, the ΔBF between all pitches was 64 nm, and the UDOF was 59 nm. The applied wavefront correction decreased the ΔBF to 12 nm and increased the UDOF to 108 nm, which was then limited by pitch 135 nm that had the smallest DOF.

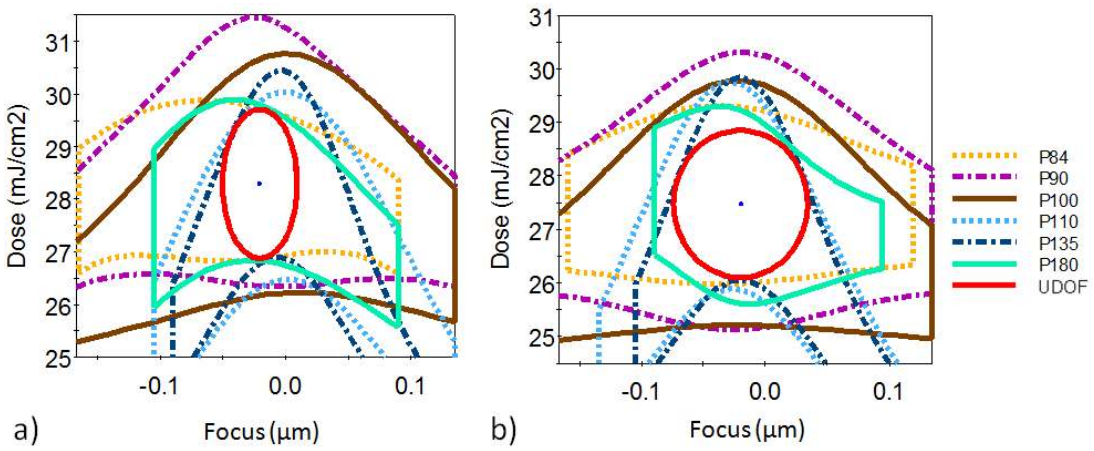

Figure 78: Experimental process windows for 45 nm lines through pitch on a 1% TaSiON AttPSM with a) no applied wavefront had a 59 nm UDOF and b) z_9=+0.02 and z_{16}=+0.06 offsets had a 108 nm UDOF, an improvement of 83%

7.5 Contact holes on a thin AttPSM

The experimental best focus for the contact holes on a 6% MoSi AttPSM is plotted with simulation in Figure 79 [271]. The simulation agrees that the $\delta BF/\delta z_9$ slope decreases through pitch, and the 120 nm pitch has a negative slope. These slopes are tabulated in Table 4 along with those calculated from the analytical expression. Again,

the simulation does not have identical slopes or intercepts as the experiment, so the optimized solution of z_9= -0.05 and z_{16}= -0.12 found by the MKS algorithm would not represent the best compensating wavefront. Again, linear interpolation through both z_9 and z_{16} offsets was used to find the best solution. The interpolated solution using analytical slopes had a primary spherical aberration offset of z_9= -0.045 and a secondary spherical aberration offset of z_{16}= -0.091.

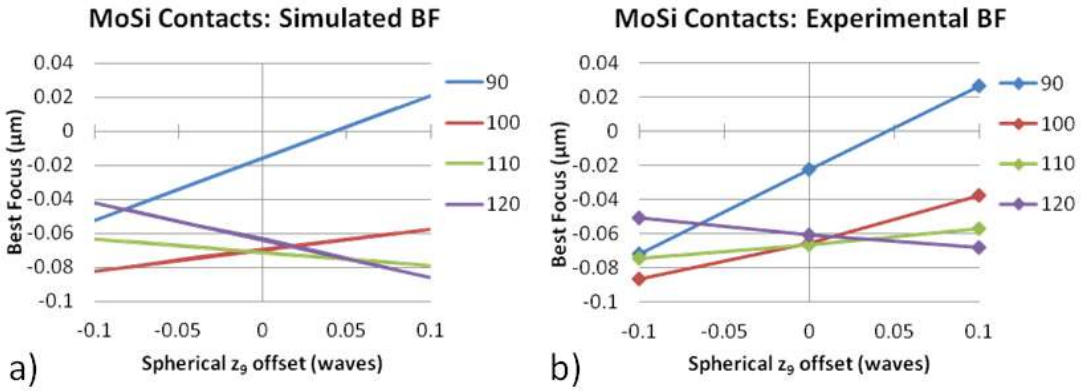

Figure 79: Best Focus versus z_9 coefficient offset through pitch for contact holes on a 6% MoSi AttPSM in a) simulation and b) experiment

The interpolated solution using experimental slopes had a primary spherical aberration offset of z_9= -0.01 and a secondary spherical aberration offset of z_{16}= -0.1. The experimental process windows are shown in Figure 80 as the uncorrected case along with the compensating wavefront. With no applied offsets, the ΔBF between all pitches was 44 nm, and the UDOF was 92 nm. The applied wavefront correction decreased the ΔBF to 7 nm and increased the UDOF to 109 nm, which was limited by the 120 nm pitch that had the smallest DOF.

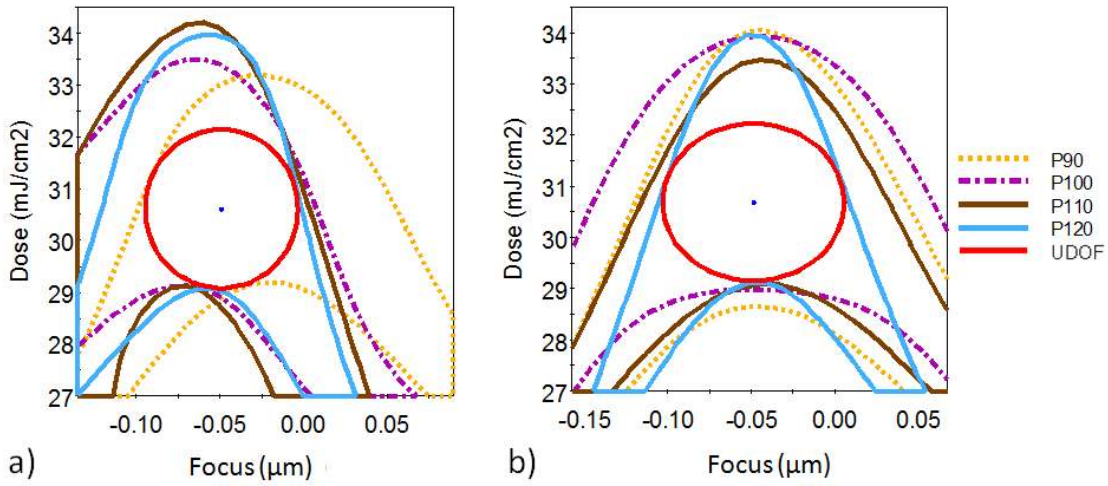

Figure 80: Experimental process windows for contact holes through pitch on a 6% MoSi AttPSM with a) no applied wavefront have a 92 nm UDOF and b) z_9= -0.01 and z_{16}= -0.1 offsets have a 109 nm UDOF, an improvement of 18%

The signs of the compensating spherical coefficients are opposite between the lines on the TaSiON mask and the contact holes on the MoSi mask. This can be explained by the phase errors from mask topography, calculated as the phase difference between the 0^{th} and 1^{st} diffraction orders taken from rigorous simulation. The phase error for each pitch is plotted at the corresponding pupil radius of the 1^{st} diffraction order based on a σ_C of 0.76 and mirrored due to a symmetric source, shown in Figure 81. Note that these functions of phase error vs. pupil radius were used to calculate the Zernike sensitivities in Figure 29. For the 1D lines on the TaSiON AttPSM, the pupil phase error for all pitches except 180 nm resemble the primary spherical Seidel aberration, shown in purple in Figure 81a. This is consistent with the optimization results that found primary spherical aberration could reduce the ΔBF for all pitches except 180 nm, as shown in Figure 49a. A higher order aberration is required to compensate for the 180 nm pitch, which may be due to the increased complexity of the pupil phase errors resulting from the entrance of the second diffraction order.

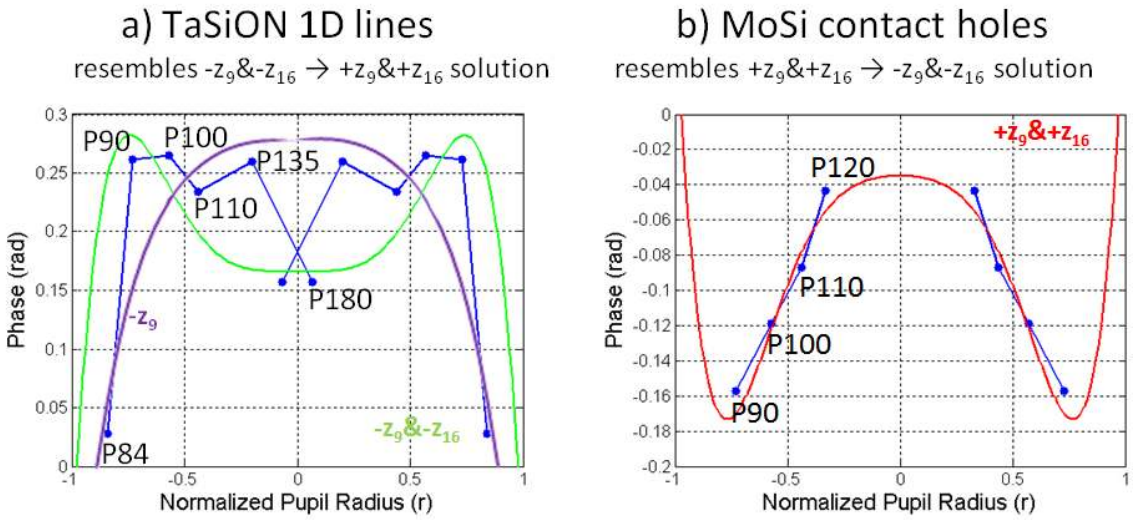

Figure 81: Simulated mask phase errors (blue) within normalized pupil radius for a) TaSiON 1D features at 84, 90, 100, 110, 135, and 180 nm pitch and b) MoSi contact hole features at 90, 100, 110, and 120 nm pitch

The pupil phase error for all pitches resembles coefficients of negative z_9 together with negative z_{16} (green in Figure 81a), suggesting that a solution of $+z_9/+z_{16}$ would provide compensation, which was also found by the MKS algorithm discussed section 5.2.2. For the contact holes on the MoSi AttPSM, the pupil phase error resembles coefficients of positive z_9 together with positive z_{16} (red in Figure 81b), suggesting that a solution of $-z_9/-z_{16}$ would provide compensation, which is also consistent with the solution found by the MKS algorithm. The predicted signs of the solutions are confirmed by experiment for the TaSiON mask and the MoSi mask in Figures 78b and 80b, respectively.

7.6 Lines and spaces on an AltPSM

Scattered light from the etched space on an AltPSM causes an intensity imbalance between the etched and unetched space [272], [273]. The unetched space prints larger than the etched space so that lines around the etched space are paired closer together. This undesirable mask topography effect can be observed in the process windows as a

larger best exposure (BE) for the shifted (etched) space and a smaller BE for the unshifted space. This results in a degraded UDOF, as shown in Figure 82a for a pitch of 115 nm. Simulations have shown that the UDOF can be increased by applied primary spherical aberration and further increased by secondary spherical aberration [269]. This was experimentally verified for a 50 nm line, as shown in Figure 82 for a 115 nm pitch, in Figure 83 for a 125 nm pitch and in Figure 84 for a 150 nm pitch. The UDOF for a pitch of 115 is increased to 66 nm by a primary spherical aberration offset of z_9= -0.09. When secondary spherical aberration is also applied, the UDOF increases slightly to 68 nm, and the FEMs become more symmetric , as shown in Figure 82c.

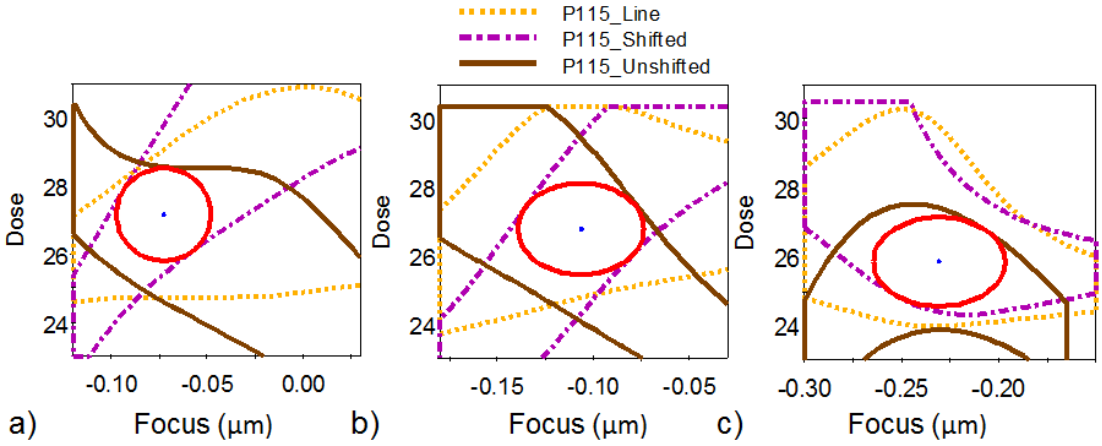

Figure 82: Experimental process windows for 50 nm line with 115 nm pitch on an AltPSM with a) no applied wavefront has a 49 nm UDOF and b) z_9= -0.09 offset has a 66 nm UDOF and c) z_9= -0.08 and z_{16}=+0.1 offsets has a 68 nm UDOF

In Figure 83a, the degraded UDOF of pitch 125 nm due to the intensity imbalance is 48 nm. The UDOF is increased to 97 nm by a primary spherical aberration offset of z_9= -0.09 in Figure 83b, and increased to 132 nm by offsets of z_9= -0.08 and z_{16}=+0.1 in Figure 83c. The UDOF of the applied wavefront is then limited by the unshifted space, which has the smallest DOF. In Figure 84a, the degraded UDOF of pitch 150 nm is 0 nm, which is increased to 83 nm by a primary spherical aberration offset of z_9= -0.09 in Figure 84b, and increased to 141 nm by offsets of z_9= -0.08 and z_{16}=+0.01 in Figure 84c.

Note that the best focus is dramatically shifted in the solution cases, due to the large applied spherical aberration.

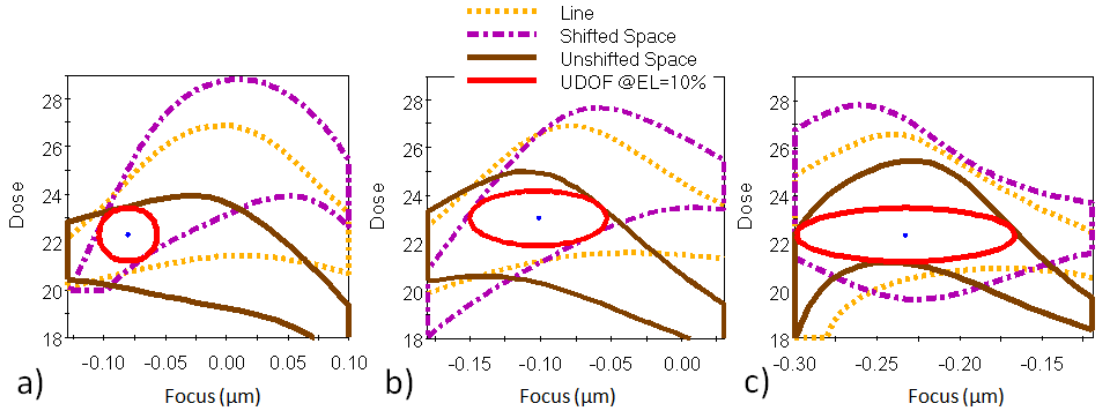

Figure 83: Experimental process windows for 50 nm line with 125 nm pitch on an AltPSM with a) no applied wavefront has a 48 nm UDOF and b) z_9= -0.09 offset has a 97 nm UDOF and c) z_9= -0.08 and z_{16}=+0.1 offsets has a 132 nm UDOF

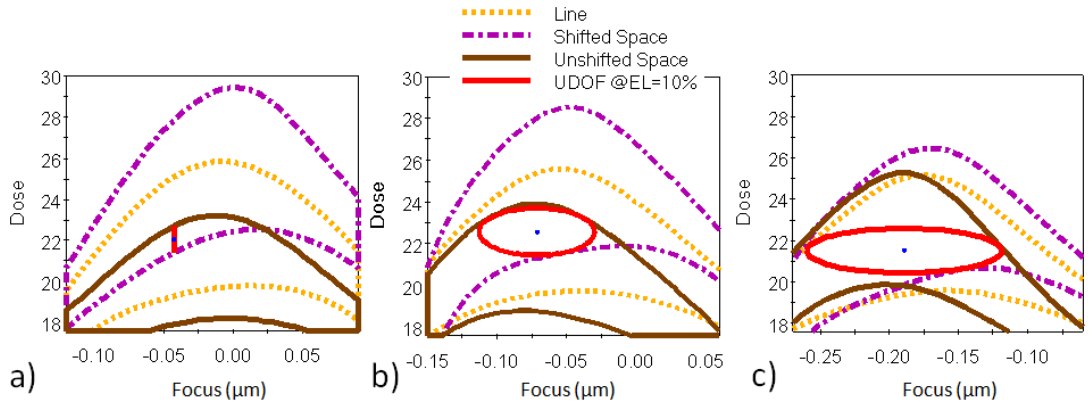

Figure 84: Experimental process windows for 50 nm line with 150 nm pitch on an AltPSM with a) no applied wavefront has a 0 nm UDOF and b) z_9= -0.09 offset has a 83 nm UDOF and c) z_9= -0.08 and z_{16}=+0.1 offsets has a 141 nm UDOF

In Figure 85a, the UDOF of pitch 200 nm with no applied offsets is 56 nm. With the z_9 of -0.09 that improved the UDOF for the smaller pitches, this UDOF is degraded to 31 nm, shown in Figure 85b. This reveals that the spherical aberration which is optimum for one pitch may degrade another. The UDOF is increased to 75 nm by offsets of z_9= -0.08 and z_{16}=+0.01 in Figure 84c, but still suffers a difference between the BE of the shifted space and the unshifted space, suggesting that larger amounts of spherical aberration would be required for compensation. In order to simultaneously optimize all

pitches, a pitch dependent bias would be required to alleviate some of the intensity imbalance for this larger pitch.

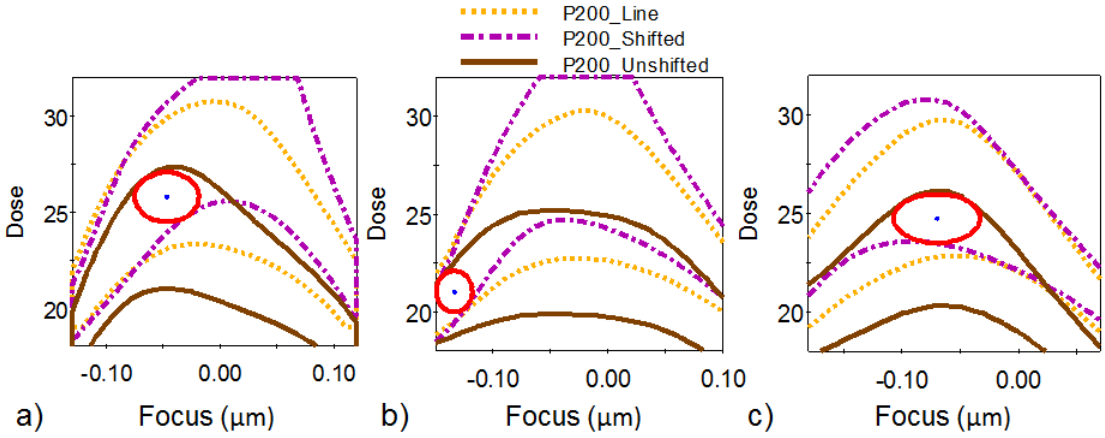

Figure 85: Experimental process windows for 50 nm line with 200 nm pitch on an AltPSM with a) no applied wavefront has a 56 nm UDOF and b) z_9= -0.09 offset has a 31 nm UDOF and c) z_9= -0.08 and z_{16}=+0.1 offsets has a 75 nm UDOF

7.7 Line ends on a thick AttPSM

The distribution of light in the pupil plane can have a large impact on the image at the wafer plane. For example, an elliptical source has the ability to stretch line end geometry in order to decrease the best exposure (BE) between the CD and the gap, as defined in Figure 59. Simulations were performed with both a symmetric C-Quad illuminator as well as an elliptical C-Quad illuminator, where the X-oriented poles are larger than the Y-oriented poles, as shown in Figure 86.

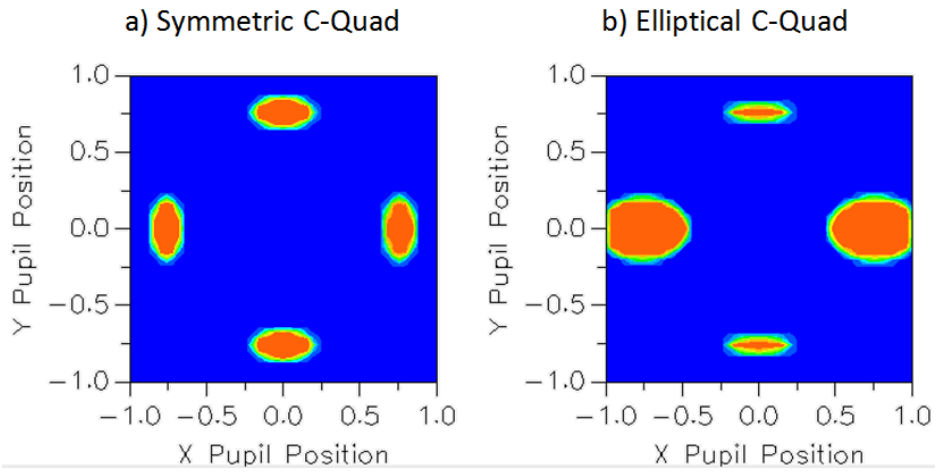

Figure 86: C-Quad source to illuminate line ends with a) symmetry and b) ellipticity

Line ends with a 50 nm line, 100 nm pitch, and 40 nm gap have no UDOF when illuminated by the symmetric C-Quad and targets are set as drawn on the mask; CD_{Target}= 50 nm and gap_{Target}= 40 nm. The elliptical source with more intensity on the X-oriented poles is able to stretch the lines closer to that drawn on the mask, increasing the UDOF with 3% EL to 95 nm shown in Figure 87b.

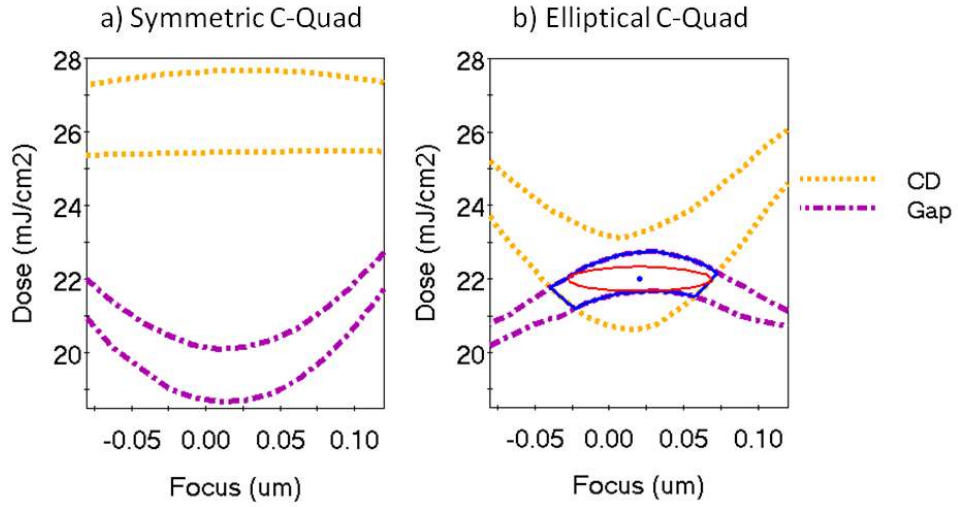

Figure 87: Kirchhoff simulated process windows of 50 nm lines at 100 nm pitch with a 40 nm gap with a) symmetric source has UDOF of 0 and b) elliptical source has UDOF of 95 nm

An experiment was performed in order to demonstrate that pupil plane phase can have a similar impact as the pupil plane magnitude. Astigmatism is particularly tuned to

the geometry of line ends due to its asymmetric fingerprint. Its effect was quantified by the UDOF between the CD and gap of line ends, where the targets were set to the values as drawn on the mask. Since an as drawn target results in a smaller process window, a smaller exposure latitude value of EL=3% was used. For a pitch of 100 nm, the UDOF with no applied offsets was 41 nm, as shown in Figure 88a. This degraded UDOF can be described as line end pullback, where the line end prints shorter than as drawn due to the proximity effects. A positive astigmatism offset of z_5=+0.05 effectively stretches the line end and reduces the line end pullback, increasing the UDOF to 135 nm as shown in Figure 88b.

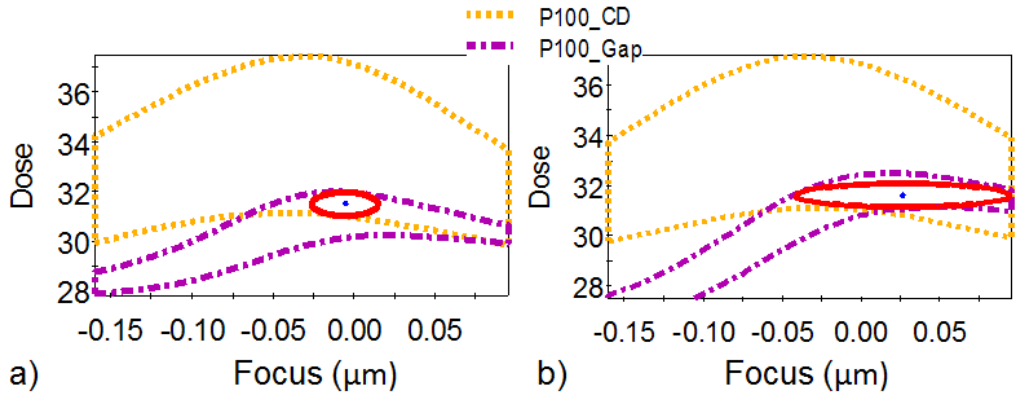

Figure 88: Experimental process windows for line ends with 100 nm pitch and 45 nm gap on a thick TaSiON AttPSM with a) no applied wavefront has a 41 nm UDOF and b) z_5=+0.05 offset has a 135 nm UDOF

With no astigmatism offset, the CD/gap UDOF of a 120 nm pitch is 45 nm, as shown in Figure 89a. The positive astigmatism offset of z_5=+0.05 increases the UDOF to 67 nm shown in Figure 89b.

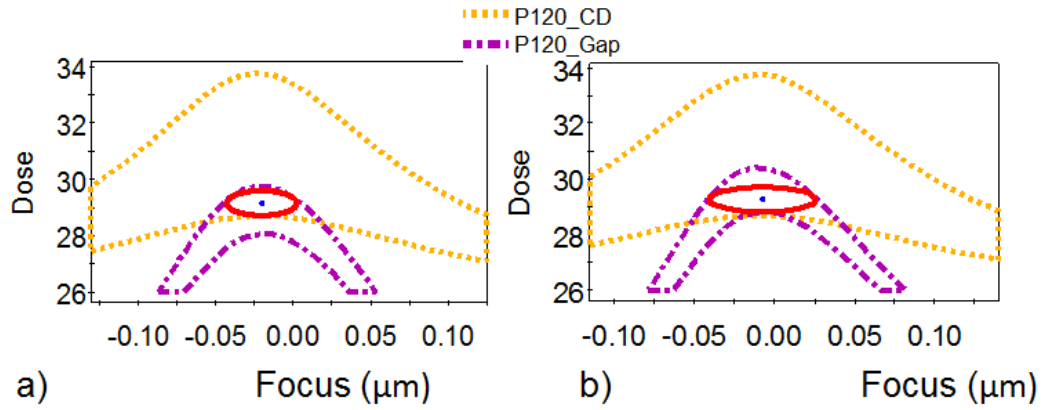

Figure 89: Experimental process windows for line ends with 120 nm pitch and 45 nm gap on a thick TaSiON AttPSM with a) no applied wavefront has a 45 nm UDOF and b) z_5=+0.05 offset has a 67 nm UDOF

Likewise, positive astigmatism increases the UDOF from 0 to 55 nm for a 140 nm pitch in Figure 90, from 7 to 48 nm for a 160 nm pitch in Figure 91, and from 31 to 42 nm for a 180 nm pitch in Figure 92. The ability of astigmatism to increase the UDOF of line ends by reducing line end pullback shows that the phase of the pupil plane can have a beneficial impact on wafer level metrics. This experiment, where the mask targets were set 'as drawn', reveals that the pupil plane may be a useful compensation parameter in a situation with mask biasing errors.

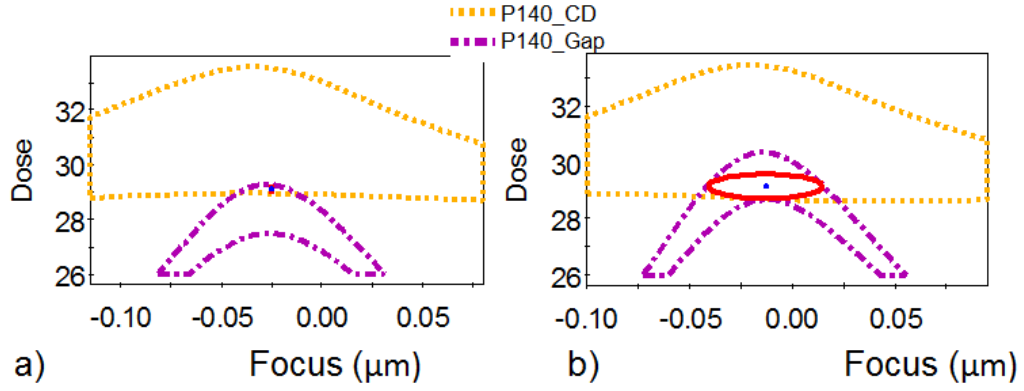

Figure 90: Experimental process windows for line ends with 140 nm pitch and 42.5 nm gap on a thick TaSiON AttPSM with a) no applied wavefront has a 0 nm UDOF and b) z_5=+0.05 offset has a 55 nm UDOF

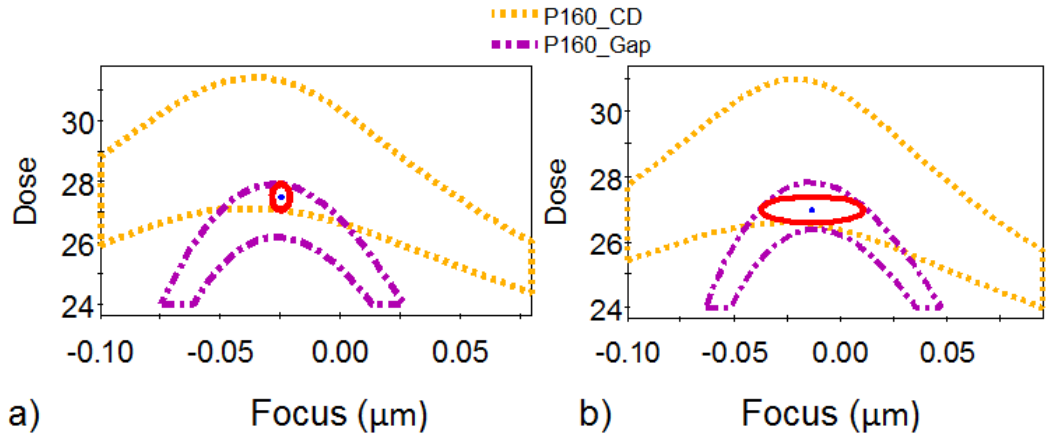

Figure 91: Experimental process windows for line ends with 160 nm pitch and 42.5 nm gap on a thick TaSiON AttPSM with a) no applied wavefront has a 7 nm UDOF and b) z_5=+0.05 offset has a 48 nm UDOF

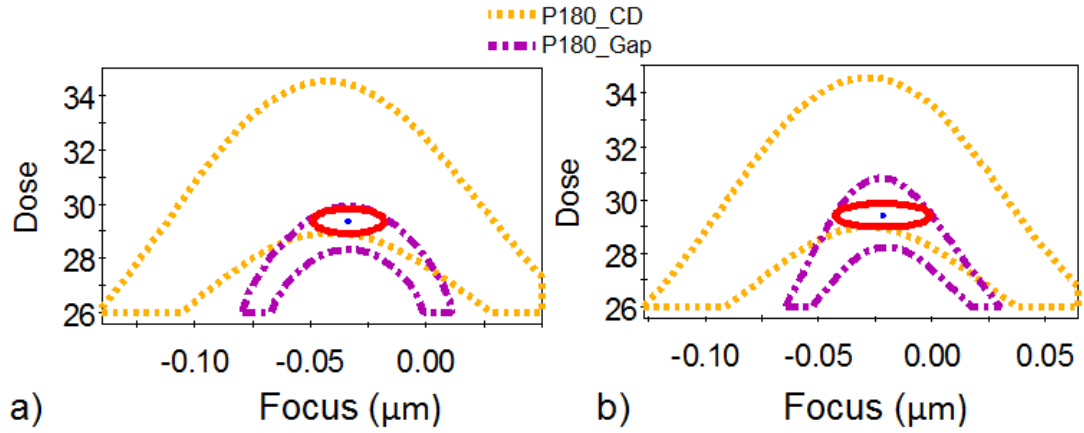

Figure 92: Experimental process windows for line ends with 180 nm pitch and 42.5 nm gap on a thick TaSiON AttPSM with a) no applied wavefront has a 31 nm UDOF and b) z_5=+0.05 offset has a 42 nm UDOF

8. CONCLUSIONS

The mask topography of subwavelength features can create phase errors on the diffraction orders, which degrade the process yield. Resolution enhancement techniques have inadequate control over these phase errors, thus wavefront compensation requires the manipulation of the lens pupil domain. Rigorous calculations showed that the phase errors caused by thick masks are particularly sensitive to spherical aberration. Spherical aberration in the form of Zernike polynomials was shown to linearly shift best focus by a pitch dependent amount and to tilt the FEM. An aerial image model was used to explain an increased FEM tilt due to off-axis illumination.

A compensating wavefront defined by Zernike spherical aberration coefficients was found by three methods; simulation, analytics, and experiment. The solution from rigorous simulation was found with a mutation-only genetic algorithm, named the MKS algorithm. An analytical expression estimated the BF shift as proportional to the coefficient of a quadratic fitted to the diffraction order's phases induced by the applied Zernike coefficients. The analytically derived slope of BF vs. z_n, or $\delta BF/\delta z_n$, for each pitch matched well with simulation, revealing that the effects of spherical aberration can be easily predicted. The analytical expression also replicated trends seen in experimental data both through pitch and orientation. The analytical solution was found by using the derived $\delta BF/\delta z_n$ slopes with linear interpolation to calculate the spherical coefficients that minimize the ΔBF. Similar linear interpolation with the experimental $\delta BF/\delta z_n$ slopes led to the experimental solution. The compensating Zernike spherical aberration coefficients

for each optimization method are tabulated in Table 5 for both the lines on the 1% TaSiON AttPSM and the contact holes on the 6% MoSi AttPSM. The effect of the optimal spherical coefficients is to shift the process windows through focus in order to increase the overlap between multiple pitches, but it does not increase the DOF of an individual pitch. These coefficients could be used as initial conditions in a joint optimization with source and mask for further improvement.

Table 5: Compensating wavefront solutions found by optimization methods

	TaSiON 1D		MoSi CH	
Optimization Method	z_9	z_{16}	z_9	z_{16}
MKS Algorithm	+0.05	+0.08	-0.05	-0.12
Analytical Expression	+0.02	+0.04	-0.05	-0.09
Experimental	+0.02	+0.06	-0.01	-0.10

The signs of solutions between the two test cases are the opposite; $-z_9/-z_{16}$ for the TaSiON mask and $+z_9/+z_{16}$ for the MoSi mask. This is correlated to the pupil phase errors due to mask topography as measured by rigorous simulations. The experimental UDOF before and after applied spherical aberration offsets is tabulated in Table 6. Note that spherical aberration did not provide a UDOF improvement for the 1D lines on the binary or MoSi mask since even without wavefront correction, the small ΔBF from these thin masks did not limit the UDOF, which is why these masks are currently used in manufacturing [274]. Conversely, the 1D lines on both the 1% TaSiON AttPSM and the AltPSM suffer from degraded UDOF due to the large topography of their bi-layer mask stack. Though the contact holes on the 6% MoSi AttPSM have the thinner mask layer, they suffer from a large ΔBF of 44 nm, which degrades the UDOF, and do benefit from wavefront compensation.

Table 6: Experimental improvement by spherical aberration

Mask Type	Feature Type	UDOF (nm) No offsets	UDOF (nm) With offsets	Improvement (%)
TaSiON	1D lines through pitch	59	108	83
MoSi	2D CHs through pitch	92	109	18
AltPSM	1D lines at pitch = 115	49	68	39
	1D lines at pitch = 125	48	132	175
	1D lines at pitch = 150	0	141	undef
	1D lines at pitch = 200	56	75	34

Experimental data demonstrates that pupil wavefront manipulation in the form of spherical aberration has the capability to compensate for mask topography induced pitch dependent best focus. Pupil wavefront manipulation provides a solution that is equivalent to the dual trench or SCAAM compensation methods, without the complexity of numerous masking steps. This dissertation recommends that spherical aberration applied in the pupil plane be used to decrease pitch dependent best focus and ultimately improve process yield. This will allow previously avoided designs, such as a combination of pitches which result in an unacceptable ΔBF, to be utilized. Pupil wavefront manipulation will also allow thick masks with independent tuning of phase and transmission to be explored for further applications in semiconductor optical lithography.

9. APPENDIX A

Matlab code connects to PROLITH™ and runs an FEM to extract BF and DOF.

Script accepts the following input parameters:

- p: pitch (nm) - number
- z_9: primary spherical coefficient (waves) - number
- z_{16}: secondary spherical coefficient (waves) - number
- z_{25}: tertiary spherical coefficient (waves) - number
- filename: name of text file where input and output values will be written - string

```
% AltPSM.m ____________________________________________________________________
% Calls Prolith to perform an FEM on an AltPSM and calculate UDOF over
% line, space, and shifted space.
% Author: Monica Kempsell Sears
% Nanolithography Research Labs, RIT
%______________________________________________________________________________


function [UDOF]= AltPSM(p,z9,z16,z25, filename)
fid = fopen(filename, 'at'); fprintf(fid,('\n')); %text file to save input/output values
str=sprintf('p %d z9 %d z16 %d z25 %d',p,z9,z16,z25);
fprintf(fid,(str)); %print input variables to text file


% Variable definition
line=50;  fprintf(fid,['l ',num2str(l)]); %print variable to text file
s=p-line; % Target space
bias=0; fprintf(fid,[' bias ',num2str(bias)]); % Global bias to lines
bias_to_phaseshifted_space=9; % Global bias to etched spaces
fprintf(fid,[' spacebias %d',bias_to_phaseshifted_space]);
Pol_state=6; %Polarization types: 1- X,2-Y,3-radial,4-azimuthal,6-XY,0-unpolarized
fprintf(fid,['Pol_state ',num2str(Pol_state)]);
DT_AltPSM=0; %1: Dual Trench 0: Single Trench
resist=1; %1: resist model 2: LPM
calculation_type=1; %0: Kirchhoff, 1: Rigorous, 2: Accelerated
pc=0.3; fprintf(fid,[' pc_',num2str(pc),' ']);%partial coherence
NA=1.35; fprintf(fid,[' NA_',num2str(NA),' ']);
lamda=193;
nQz=1.56312;
etch_depth=lamda/(2*(nQz-1)); % 171.4 nm is theoretical
if DT_AltPSM==1
    etch_type=1.5; fprintf(fid,' DTAltPSM '); %Dual Trench
else
    etch_type=1; fprintf(fid,' STAltPSM ');%Single Trench
end;

%FEM inputs
E=15; F=0.05; %initial focus and exposure values
E_start=10;E_end=25;E_step=2; % exposure range for FEM
fprintf(fid,sprintf(' E_start:%d/E_end:%d/E_step:%d',E_start,E_end,E_step));
EL=.03;  % Exposure Latitude: 0.03= +/-3% requirement
fprintf(fid,[' EL_',num2str(EL),' ']);
plot_NILS=0; %if =1, displays figure with NILS through horizontal position
return_after_DOF=0; %for troubleshooting: if 1, stops simulation after DOF calculation
plot_FE=0; %if =1, displays figure with FEM
measure_tilt=0; %if =1, extracts tilt of FEM
```

```
if return_after_DOF==1
    display('Will Return after DOF');
end;

%connects to Prolith
global MPPI_PROLITH
global MPPI_PROLITHDOCUMENT
global MPPI_PROLITHSIMENGINE
connectprolith;
invoke(MPPI_PROLITH, 'Database'); % set database
% set imaging system
MPPI_imagingSystem = invoke(MPPI_PROLITHDOCUMENT, 'GetImagingSystem', 1);
%set image calculation mode to cmVector, cmHighNAScalar, or cmFullScalar
invoke (MPPI_imagingSystem, 'SetImageCalculationMode', 'cmVector');
% define simulation grid
GridSize = invoke(MPPI_PROLITHDOCUMENT, 'GetGridSize');
GridSize.get('UseTargetGridSizes').set('Value',1);
gridvalueXY=0.6; GridSize.get('TargetGridSizeXY').set('Value', gridvalueXY);
gridvalueZ=1.2; GridSize.get('TargetGridSizeZ').set('Value', gridvalueZ);
if resist==2 % USE LUMPED PARAMETER MODEL
    LPM_resist_thickness=100; fprintf(fid,' LPM ');
    invoke(MPPI_PROLITHSIMENGINE, 'SetInput', 29351, 0, 1); % 0: resist model 1: LPM
    invoke(MPPI_PROLITHSIMENGINE, 'SetInput', 29646, 0, 2); % 2: defocus through resist
    invoke(MPPI_PROLITHSIMENGINE, 'SetInput', 29344, 0, LPM_resist_thickness); % nm
    invoke(MPPI_PROLITHSIMENGINE, 'SetInput', 30042, 0, 1.7); % Refractive index
    invoke(MPPI_PROLITHSIMENGINE, 'SetInput', 29346, 0, 2); % Diffusion Length nm
    invoke(MPPI_PROLITHSIMENGINE, 'SetInput', 29345, 0, 0.02); % Absorption 1/um
    invoke(MPPI_PROLITHSIMENGINE, 'SetInput', 29343, 0, 20); % Contrast
    invoke(MPPI_PROLITHSIMENGINE, 'SetInput', 29357, 0, 1); % Dose to Clear mJ/cm2
    invoke(MPPI_PROLITHSIMENGINE, 'SetInput', 29356, 0, 0); % Development Rmin nm/s
elseif resist==1
    invoke(MPPI_PROLITHSIMENGINE, 'SetInput', 29351, 0, 0); % 0: resist model 1: LPM
    Resist_Stack = invoke(MPPI_PROLITHDOCUMENT, 'GetWaferProcessStack');
    Resist_Process = invoke(Resist_Stack, 'GetResistProcess');
    waferProcessSubstrate = invoke (Resist_Stack, 'GetProcess', 1);
    invoke (waferProcessSubstrate, 'LoadMaterial', 'Silicon', 1);
    %calibrated physical resist model from IMEC
    resist_name= 'TOK TArF Pi6-001ME - bin'; resist_thickness=105;
    BARC_name='Brewer ARC 29S'; BARC_thickness=95;
    invoke (Resist_Process, 'LoadResist', resist_name);
    Resist_Process.get('Thickness').set('Value',resist_thickness);
    invoke(Resist_Stack,'InsertCoatProcess',2, BARC_name, 0, BARC_thickness); %Topcoat
    fprintf(fid,' IMEC_Resist_Model ');
end;

% Set calculation mode
invoke(MPPI_PROLITHSIMENGINE,'SetMaskTopoSimulationMode',1, calculation_type);
invoke(MPPI_imagingSystem,'LoadParametricSource', 10) %10: conventional 70: Dipole
MPPI_Source = invoke (MPPI_imagingSystem, 'GetSource');
MPPI_Source.get('Radius').set('Value',pc);fprintf(fid,[' pc',num2str(pc)]);
MPPI_imagingSystem.get('Wavelength').set('Value',lamda); % wavelength definition
MPPI_imagingSystem.get('IsImmersionEnabled').set('Value',1);
MPPI_imagingSystem.get('ReductionRatio').set('Value',4); %ASML systems are 4
MPPI_imagingSystem.get('RefractiveIndex').set('Value',1.44);
MPPI_imagingSystem.get('NumericalAperture').set('Value',NA); %numerical aperture
%Set Polarization
invoke (MPPI_imagingSystem, 'LoadParametricPolarization', Pol_state);
Polarization = invoke (MPPI_imagingSystem, 'GetPolarization');
Polarization.get('DegreeOfPolarization').set('Value',1); %0 is unpolarized

% parametric 1D AltPSM Line mask: line defined in middle
invoke(MPPI_PROLITHSIMENGINE,'LoadParametricMask',1, 2, 0);
Mask_1D = MPPI_PROLITHDOCUMENT.GetMask (1);
invoke(Mask_1D, 'PSMFeatureWidth', 1, line+bias); % Line
invoke(Mask_1D, 'PSMFeatureTransmittance', 1, 0); % Line - transmittance=0
invoke(Mask_1D, 'PSMFeaturePhase', 1, 0); % Line - phase =0
% unetched (unshifted) space
invoke(Mask_1D, 'PSMFeatureWidth', 4, 2*p-s-2*line-2*bias-bias_to_phaseshifted_space);
invoke(Mask_1D, 'PSMFeatureTransmittance', 4, 1); % space - transmission=1
invoke(Mask_1D, 'PSMFeaturePhase', 4, 0); % space - phase=0
invoke(Mask_1D, 'PSMFeatureWidth', 3, line+bias); % Line
```

```
invoke(Mask_1D, 'PSMFeatureTransmittance', 3, 0); % Line - transmittance=0
invoke(Mask_1D, 'PSMFeaturePhase', 3, 0); % Line - phase =0
invoke(Mask_1D, 'PSMFeatureWidth', 2, s+bias_to_phaseshifted_space); % shifted space
invoke(Mask_1D, 'PSMFeatureTransmittance', 2, 1); % space - transmission=1
invoke(Mask_1D, 'PSMFeaturePhase', 2, 180); % space - phase=180

% Set up simulation region
[~] = invoke(MPPI_PROLITHSIMENGINE, 'SimulationRegion');
invoke(MPPI_PROLITHSIMENGINE, 'SetInput', 29865,0,2*(p+p/10)); % width
% measurement plane for line
invoke(MPPI_PROLITHSIMENGINE,'Create1DMetrologyPlane','line1',-p/2-p/10,p/2+p/10);
% measurement plane for shifted space
invoke(MPPI_PROLITHSIMENGINE,'Create1DMetrologyPlane','shifted_space',-p/10,p+p/10);
%measurement plane for space
invoke(MPPI_PROLITHSIMENGINE,'Create1DMetrologyPlane','Unshifted_space',-p-p/10,p/10);
%Target for line CD
invoke(MPPI_PROLITHSIMENGINE, 'SetMetrologyPlaneLithoTargetCD','line1', line);
%Target for space
invoke(MPPI_PROLITHSIMENGINE, 'SetMetrologyPlaneLithoTargetCD','shifted_space',s);
%Target for Unshifted_space
invoke(MPPI_PROLITHSIMENGINE, 'SetMetrologyPlaneLithoTargetCD','Unshifted_space',s);
invoke(MPPI_PROLITHSIMENGINE, 'SetActiveMetrologyPlane', 'line1');
% Aerial Image Tone: 1= Line, 0=Space
invoke(MPPI_PROLITHSIMENGINE, 'SetMetrologyPlaneAerialImageTone', 'line1', 1);
invoke(MPPI_PROLITHSIMENGINE, 'SetMetrologyPlaneAerialImageTone', 'shifted_space', 0);
invoke(MPPI_PROLITHSIMENGINE, 'SetMetrologyPlaneAerialImageTone', 'Unshifted_space', 0);

% Measurement method
invoke(MPPI_PROLITHSIMENGINE, 'SetInput', 29641, 0, 0); %0: Relative 1: Absolute
invoke(MPPI_PROLITHSIMENGINE, 'SetInput', 29115, 0, 10); %Measurement Height 10%
invoke(MPPI_PROLITHSIMENGINE, 'SetInput', 29604, 0, 2);% 1: Weighted 2: Raw Threshold
invoke(MPPI_PROLITHSIMENGINE, 'SetInput', 29358, 0, 0); %0nm CD measurement offset
invoke(MPPI_PROLITHSIMENGINE, 'SetInput', 29605, 0, 1); %0: Rectangle 1: Ellipse

if calculation_type~=0
    if calculation_type==1
        fprintf(fid,(' Rigorous '));
    else
        fprintf(fid,(' Accelerated '));
    end;
    % Based on binary stack values from IMEC:
    sidewall_angle=86;
    tCrO=18; nCrO=1.965; kCrO=1.201; %Chromium Oxide
    tCr=55; nCr=1.477; kCr=1.762; %Chrome
    invoke(MPPI_PROLITHSIMENGINE,'InsertMaskTopoLayer',1, 1);
    invoke(MPPI_PROLITHSIMENGINE, 'SetMaskTopoLayerMaterial', 1, 1, 'Chromium Oxide');
    invoke(MPPI_PROLITHSIMENGINE, 'SetMaskTopoLayerMaterial', 1, 2, 'Chromium');
    invoke(MPPI_PROLITHSIMENGINE, 'SetMaskTopoLayerThickness', 1, 1, tCrO);
    invoke(MPPI_PROLITHSIMENGINE, 'SetMaskTopoLayerRIReal', 1, 1, nCrO);
    invoke(MPPI_PROLITHSIMENGINE, 'SetMaskTopoLayerRIImaginary', 1, 1, kCrO);
    invoke(MPPI_PROLITHSIMENGINE, 'SetMaskTopoLayerThickness', 1, 2, tCr);
    invoke(MPPI_PROLITHSIMENGINE, 'SetMaskTopoLayerRIReal', 1, 2, nCr);
    invoke(MPPI_PROLITHSIMENGINE, 'SetMaskTopoLayerRIImaginary', 1, 2, kCr);
    invoke(MPPI_PROLITHSIMENGINE, 'SetMaskTopoLayerRIReal', 1, 3, nQz);
    % Etch CrO and Cr
    invoke(MPPI_PROLITHSIMENGINE,'SetMaskTopoGroupLayerEtchDepth',1, 1, 0, 1,tCrO);
    invoke(MPPI_PROLITHSIMENGINE,'SetMaskTopoGroupLayerEtchDepth',1, 2, 0, 1,tCr);
    invoke(MPPI_PROLITHSIMENGINE,'SetMaskTopoGroupLayerProfileInfo',1, 1, 0, 1, 0,...
        sidewall_angle);
    invoke(MPPI_PROLITHSIMENGINE,'SetMaskTopoGroupLayerProfileInfo',1, 2, 0, 1, 0,...
        sidewall_angle);
    % Etch Quartz by 0.2nm to remove all Cr in unshifted region
    invoke(MPPI_PROLITHSIMENGINE,'SetMaskTopoGroupLayerEtchDepth',1, 3, 0, 1,0.2);
    invoke(MPPI_PROLITHSIMENGINE,'SetMaskTopoGroupLayerEtchDepth',1, 3, 180, 1,...
        etch_depth*etch_type); % Etch Quartz for 180deg region
    % 0: Sidewall angle, 1: Footer height, 2: top Corner radius, 3: bottom Corner radius
    invoke(MPPI_PROLITHSIMENGINE,'SetMaskTopoGroupLayerProfileInfo',1, 3, 180, 1,...
        0, sidewall_angle);
    invoke(MPPI_PROLITHSIMENGINE,'SetMaskTopoGroupLayerProfileInfo',1, 2, 180, 1,...
        0, sidewall_angle);
    invoke(MPPI_PROLITHSIMENGINE,'SetMaskTopoGroupLayerProfileInfo',1, 1, 180, 1,...
```

```
        0, sidewall_angle);
    invoke(MPPI_PROLITHSIMENGINE,'SetMaskTopoGroupLayerProfileInfo',1, 1, 0, 1, 0,...
        sidewall_angle);
    invoke(MPPI_PROLITHSIMENGINE,'SetMaskTopoGroupLayerProfileInfo',1, 2, 0, 1, 0,...
        sidewall_angle);
    invoke(MPPI_PROLITHSIMENGINE,'SetMaskTopoGroupLayerBiasInfo',1, 1, 0, 1, 0, 0);
    invoke(MPPI_PROLITHSIMENGINE,'SetMaskTopoGroupLayerProfileInfo',1, 3, 0, 1, 0,...
        sidewall_angle);
    if DT_AltPSM==1
        invoke(MPPI_PROLITHSIMENGINE,'SetMaskTopoGroupLayerEtchDepth',1, 3, 0,...
            1,etch_depth*0.5); % Etch other Quartz for dual trench
        invoke(MPPI_PROLITHSIMENGINE,'SetMaskTopoGroupLayerProfileInfo',1, 3, 0,...
            1, 0, sidewall_angle);
    end;

    % Define Maxwell Advanced Properties for 1st pass (only pass)
    %RCWA (1) for 1D mask, FDTD (2) for 2D mask
    invoke(MPPI_PROLITHSIMENGINE,'SetMaskTopoEMFType',1, 1);
    %speedfactor between 1 and 8, smaller means more accuracy
    invoke(MPPI_PROLITHSIMENGINE,'SetEMFSpeedFactorXY',1, 4);
    %smaller speedfactor required for sloped sidewall angles on mask
    invoke(MPPI_PROLITHSIMENGINE,'SetEMFSpeedFactorZ',1, 6);
     %0: single point, 1: range of angles
    invoke(MPPI_PROLITHSIMENGINE,'SetEMFSourceIntegration',1, 1);
    % if type=range of angles
    invoke(MPPI_PROLITHSIMENGINE,'SetEMFMaxAngleFromOpticalAxis',1, 4);
    %either 1 or 2 number of angles
    invoke(MPPI_PROLITHSIMENGINE,'SetEMFMaxNumAnglesFromOpticalAxis',1, 1);
    %either 2, 4, or 8
    invoke(MPPI_PROLITHSIMENGINE,'SetEMFAzimuthalNumOfAngles',1, 4);
else
    fprintf(fid,(' Kirchhoff '));
end;

% load a pupil filter
invoke(MPPI_imagingSystem, 'LoadDatabaseAberration', 'TEST', 1);
aberrationZernike=invoke(MPPI_imagingSystem, 'GetAberration');
aberrationZernike.get('Coefficient', 9).set('Value',z9); % Primary Spherical
aberrationZernike.get('Coefficient', 16).set('Value',z16); % Secondary Spherical
aberrationZernike.get('Coefficient', 25).set('Value',z25); % Tertiary Spherical

% Set metrology parameters
% Sidewall Angle Specification (degrees) 1-> no requirement
invoke(MPPI_PROLITHSIMENGINE, 'SetInput', 29186,0,80);
% Resist Loss Specification (percent)99-> no requirement
invoke(MPPI_PROLITHSIMENGINE, 'SetInput', 29187,0,20);
% Exposure Latitude Specification (percent)
invoke(MPPI_PROLITHSIMENGINE, 'SetInput', 29188,0,100*EL);
% Set Focus Parameters
MPPI_imagingSystem.get('Dose').set('value', E);
MPPI_imagingSystem.get('FocusAtMask').set('value', 0);
MPPI_imagingSystem.get('Focus').set('value', 0);
invoke(MPPI_imagingSystem, 'SetFocusDirection', 'fdUp');
invoke(MPPI_imagingSystem, 'SetFocusRelativePosition', 'rpTop');

%_____________________________________________________________________
% Wide focal range to determine focus values with NILS>0
%_____________________________________________________________________

F_start=-0.5; F_stop=0.2; F_step=0.01;

fprintf(fid,sprintf(' F_start:%.1f/F_end:%.1f/F_step:%.2f',F_start,F_stop,F_step));
Focus=F_start:F_step:F_stop;
% Focus is input parameter to simulation
invoke(MPPI_PROLITHSIMENGINE, 'AddInput', 29102, F_start,F_stop,F_step,F);
% NILS-Right in Resist is output parameter
invoke(MPPI_PROLITHSIMENGINE, 'AddOutput', 75);
% NILS-Left in Resist is output parameter
invoke(MPPI_PROLITHSIMENGINE, 'AddOutput', 76);
invoke(MPPI_PROLITHSIMENGINE, 'SimulationRun');
% Error Handling for the next statements
```

```
while invoke(MPPI_PROLITHSIMENGINE, 'IsDataSetReady') == 0;
    pause(0.2);
end

% Create variables which hold the simulated NILS values
nrr = double(invoke(MPPI_PROLITHSIMENGINE, 'NumResultsRecords'));
NILS_right=zeros(1,nrr);NILS_left=zeros(1,nrr);
for irr = 1:nrr
        NILS_right(irr) = invoke(MPPI_PROLITHSIMENGINE, ...
            'GetMetrologyPlaneSimSetResult', 'line1', 75,irr-1);
        NILS_left(irr) = invoke(MPPI_PROLITHSIMENGINE, ...
            'GetMetrologyPlaneSimSetResult', 'line1', 76,irr-1);
end
[maxNILSR,IR]=max(NILS_right); % maximum NILS - Right
[maxNILSL,IL]=max(NILS_left); % maximum NILS - Left
maxNILS=max(maxNILSR,maxNILSL);
focus_index=round(mean(IR,IL));

% Find minimum acceptable focus value: Start from focus with highest
% NILS, and keep lowering until the NILS becomes less than 90% of max NILS
temp_focus=focus_index;
while temp_focus>0 && NILS_right(temp_focus)>0.9*maxNILSR ...
        && NILS_left(temp_focus)>0.9*maxNILSL
    focus_index_lower=temp_focus;
    temp_focus=temp_focus-1;
end;
if temp_focus==focus_index
    focus_index_lower=temp_focus; % weren't any smaller in-spec focus values
end;
% Find maximum acceptable focus value: Start from focus with highest
% NILS, and keep increasing until the NILS becomes less than 90% of max NILS
temp_focus=focus_index;
while NILS_right(temp_focus)>0.9*maxNILSR && NILS_left(temp_focus)>0.9*maxNILSL
    focus_index_higher=temp_focus;
    temp_focus=temp_focus+1;
end;
if temp_focus==focus_index
    focus_index_higher=temp_focus; % weren't any larger in-spec focus values
end;
% middle focus value becomes center of range where NILS>90% of max NILS
focus_index=round((focus_index_lower+focus_index_higher)/2); % middle Focus index
max_index=Focus(round(focus_index)); % middle Focus value

% Simulation to determine BE at focus = max_index_____________________________
invoke(MPPI_PROLITHSIMENGINE, 'SetInput', 29188,0,200); % max EL to force DOF=0
invoke(MPPI_PROLITHSIMENGINE, 'AddInput', 29102, max_index-0.001,max_index+0.001,...
    0.0005,max_index); % Tiny Focus range to look at max EL
invoke(MPPI_PROLITHSIMENGINE, 'AddInput', 29101, E_start,E_end,E_step,E); % Exposure
invoke(MPPI_PROLITHSIMENGINE, 'SetActiveMetrologyPlane', 'line1');
invoke(MPPI_PROLITHSIMENGINE, 'AddOutput', 21); % Resist CD

invoke(MPPI_PROLITHSIMENGINE, 'SimulationRun');
while invoke(MPPI_PROLITHSIMENGINE, 'IsDataSetReady') == 0;
    pause(0.2);
end
BE = invoke(MPPI_PROLITHSIMENGINE, 'BestExposure'); % Best Exposure - output

% Using BE, run simulation through focus to find new "BF"
%FIND index at minimum CD Error and use that as new_max_index
invoke(MPPI_PROLITHSIMENGINE, 'AddInput', 29102, F_start,F_stop,F_step,F); % Focus
invoke(MPPI_PROLITHSIMENGINE, 'SetInput', 29101, 0,BE); % Resist Exposure
invoke(MPPI_PROLITHSIMENGINE, 'AddOutput', 25); % Resist Placement Error
invoke(MPPI_PROLITHSIMENGINE, 'AddOutput', 24); % Resist Loss (nm)
invoke(MPPI_PROLITHSIMENGINE, 'AddOutput', 22); % CD Error

invoke(MPPI_PROLITHSIMENGINE, 'SimulationRun');
while invoke(MPPI_PROLITHSIMENGINE, 'IsDataSetReady') == 0;
    pause(0.2);
end
nrr = double(invoke(MPPI_PROLITHSIMENGINE, 'NumResultsRecords'));
PE_num=zeros(1,nrr);RL_num=zeros(1,nrr);CD_error=zeros(1,nrr);
```

```
for irr = 1:nrr
    RL_num(irr)=invoke(MPPI_PROLITHSIMENGINE,'GetMetrologyPlaneSimSetResult',...
        'line1', 24,irr-1);
    CD_error(irr)=invoke(MPPI_PROLITHSIMENGINE,'GetMetrologyPlaneSimSetResult',...
        'line1', 22,irr-1);
    % only extract Placement Error if Resist Loss and CD Error are resonable
    if RL_num(irr)< 0.9*resist_thickness && CD_error(irr)<40
        PE_num(irr)=invoke(MPPI_PROLITHSIMENGINE,'GetMetrologyPlaneSimSetResult',...
            'line1', 25,irr-1);
    else
        PE_num(irr)=100;
    end;
end;
if plot_NILS==1
    figure; plot(Focus,PE_num); title('Placement Error');xlabel('Focus (um)'); ...
        ylabel('PE (nm)');
    figure; plot(Focus,RL_num); title('Resist Loss');xlabel('Focus (um)'); ...
        ylabel('RL (nm)');
    figure; plot(Focus,CD_error); title('CD Error');xlabel('Focus (um)'); ...
        ylabel('CD Error (%)');
end;
if min(abs(CD_error))<max(abs(CD_error)) % verify CD_error isn't constant
    [~,I_CDE]=min(abs(CD_error));
    max_index=Focus(I_CDE); % NEW max_index
end;
fprintf(fid,[' max_index ',num2str(max_index)]);

if plot_NILS==1
    display(['max_index: ',num2str(max_index)]);
    figure; plot(Focus, NILS_right,'b.-',Focus, NILS_left,'r.-');
    title(sprintf('NILS through focus for biases: %d / %d',bias,...
        bias_to_phaseshifted_space)); xlabel('Focus'); ylabel('NILS');
end;

% Find number of focus values to include below max_index
compare_value=0.1*maxNILS; %criteria
for temp=1:length(Focus)
    if focus_index-temp<1
        new_F_start=F_start;
    elseif NILS_right(focus_index-temp)<compare_value || ...
            NILS_left(focus_index-temp)<compare_value
        new_F_start=Focus(focus_index-temp)+F_step/2;
        break;
    end;
end;
% Find number of values to include above max_index
for temp=1:length(Focus)
    if focus_index+temp>length(NILS_right)
        new_F_stop=F_stop;
    elseif NILS_right(focus_index+temp)<compare_value || ...
            NILS_left(focus_index+temp)<compare_value
            new_F_stop=Focus(focus_index+temp)-F_step/2;
            break;
    end;
end;
fprintf(fid,sprintf(' new_F_start:%.2f/new_F_stop:%.2f',new_F_start,new_F_stop));

Fnew_step=(new_F_stop-new_F_start)/25; % 25 focus points for simulation
if Fnew_step>0.01
    Fnew_step=0.01; % ensure step size is no bigger than 10nm
end;
if Fnew_step<0.0001 % ensure step size is at least 0.1nm
    display('Error: No focal range');
    fprintf(fid,('\n'));fclose(fid);
    disconnectprolith;
    UDOF=0; return;
end;


%_____________________________________________________________________________
% Find BE at focus where NILS is maximum: Focus= NEW max_index
```

```
invoke(MPPI_PROLITHSIMENGINE, 'SetInput', 29188,0,200); % max EL to force DOF=0
invoke(MPPI_PROLITHSIMENGINE, 'AddInput', 29102, max_index-0.001,max_index+0.001,...
    0.0005,max_index); % narrow Focus range to find max EL
invoke(MPPI_PROLITHSIMENGINE, 'AddInput', 29101, 15,120,2,E); % huge exposure range
invoke(MPPI_PROLITHSIMENGINE, 'AddOutput', 21); % Resist CD

invoke(MPPI_PROLITHSIMENGINE, 'SimulationRun');
while invoke(MPPI_PROLITHSIMENGINE, 'IsDataSetReady') == 0;
    pause(0.2);
end
BE = invoke(MPPI_PROLITHSIMENGINE, 'BestExposure');
BE_range = get(MPPI_PROLITHSIMENGINE, 'ExposureLatitudeAbsolute');

if BE==0
    display('Error: Best Exposure is zero');
    fprintf(fid,'\n');fclose(fid);
    if return_after_DOF==0
        disconnectprolith;
    end;
    UDOF=0;  return;
end;

%_____________________________________________________________________
% Measure Placement Error at BE:
invoke(MPPI_PROLITHSIMENGINE, 'SetInput', 29102, 0,max_index); % Focus
invoke(MPPI_PROLITHSIMENGINE, 'SetInput', 29101, 0,BE); % Resist Model
invoke(MPPI_PROLITHSIMENGINE, 'AddOutput', 25); % Resist Placement Error
invoke(MPPI_PROLITHSIMENGINE, 'SingleRun');
invoke(MPPI_PROLITHSIMENGINE, 'SetActiveMetrologyPlane', 'line1');
PE = invoke(MPPI_PROLITHSIMENGINE, 'GetMetrologyPlaneSingleRunResult', 'line1', 18);
fprintf(fid,[' BE ',num2str(BE)]);
fprintf(fid,[' PE ',num2str(PE)]);

%_____________________________________________________________________
% Wide range for initial FEM to determine DOF
%_____________________________________________________________________


E_start=BE-BE_range/2;
E_stop=BE+BE_range/2;
E_num=8; % number of exposure values in FEM
E_step=0.999*(E_stop-E_start)/(E_num-1);

invoke(MPPI_PROLITHSIMENGINE, 'SetInput', 29188,0,100*EL); % EL Specification (%)
% Focus
invoke(MPPI_PROLITHSIMENGINE, 'AddInput', 29102, new_F_start,new_F_stop,Fnew_step,F);
% Exposure
invoke(MPPI_PROLITHSIMENGINE, 'AddInput', 29101, E_start,E_stop,E_step,E);
invoke(MPPI_PROLITHSIMENGINE, 'AddOutput', 21); % Resist CD

invoke(MPPI_PROLITHSIMENGINE, 'RunSimSet');
while invoke(MPPI_PROLITHSIMENGINE, 'IsDataSetReady') == 0;
    pause(0.2);
end

% Save .pl2 Document
PL2File = 'D:\monica\Documents\Simulator\Output data\AltPSM.pl2';
invoke(MPPI_PROLITHDOCUMENT,'SaveAs', PL2File);

% Extract Output Values for overlapping features
UDOF=get(MPPI_PROLITHSIMENGINE, 'OverlapDepthOfFocus');
UBF=get(MPPI_PROLITHSIMENGINE, 'OverlapBestFocus');
UBE=get(MPPI_PROLITHSIMENGINE, 'OverlapBestExposure');
% Extract Output Values for line
invoke(MPPI_PROLITHSIMENGINE, 'SetActiveMetrologyPlane', 'line1');
BF = invoke(MPPI_PROLITHSIMENGINE, 'BestFocus');
BE = invoke(MPPI_PROLITHSIMENGINE, 'BestExposure');
DOF = invoke(MPPI_PROLITHSIMENGINE, 'DepthOfFocus');
PFE_NAME_line=['D:\Simulator output files\STAltPSM trenchbias\STAltPSM_L',...
    num2str(line),'_L_P',num2str(p),'_z9-',num2str(z9),'.pfe'];
invoke(MPPI_PROLITHSIMENGINE, 'OutputPFEData', PFE_NAME_line);
```

```
% Extract Output Values for unshifted space
invoke(MPPI_PROLITHSIMENGINE, 'SetActiveMetrologyPlane', 'Unshifted_space');
BFSspace = invoke(MPPI_PROLITHSIMENGINE, 'BestFocus');
BESspace = invoke(MPPI_PROLITHSIMENGINE, 'BestExposure');
DOFSspace = invoke(MPPI_PROLITHSIMENGINE, 'DepthOfFocus');
PFE_NAME_Unshiftedspace=['D:\Simulator output files\STAltPSM trenchbias\STAltPSM_L',...
    num2str(line),'_Us_P',num2str(p),'_z9-',num2str(z9),'.pfe'];
invoke(MPPI_PROLITHSIMENGINE, 'OutputPFEData', PFE_NAME_Unshiftedspace);
% Extract Output Values for shifted space
invoke(MPPI_PROLITHSIMENGINE, 'SetActiveMetrologyPlane', 'shifted_space');
BFspace = invoke(MPPI_PROLITHSIMENGINE, 'BestFocus');
BEspace = invoke(MPPI_PROLITHSIMENGINE, 'BestExposure');
DOFspace = invoke(MPPI_PROLITHSIMENGINE, 'DepthOfFocus');
PFE_NAME_Shiftedspace=['D:\Simulator output files\STAltPSM trenchbias\STAltPSM_L',...
    num2str(line),'_Ss_P',num2str(p),'_z9-',num2str(z9),'.pfe'];
invoke(MPPI_PROLITHSIMENGINE, 'OutputPFEData', PFE_NAME_Shiftedspace);

if return_after_DOF==1
    display(sprintf('Line1 DOF: %.3f BF: %.3f BE: %.2f',DOF,BF,BE));
    display(sprintf('Unshifted_space DOF: %.3f BF: %.3f BE: %.2f',DOFspace,...
        BFspace,BEspace));
    display(sprintf('shifted_space DOF: %.3f BF: %.3f BE: %.2f',DOFSspace,...
        BFSspace,BESspace));
    display(sprintf('UDOF: %.3f BF: %.3f BE: %.2f',UDOF,UBF,UBE));
    fprintf(fid,'\n');fclose(fid);return;
end;
if DOF==0
    fprintf(fid,[' BestFocus1 ',num2str(BF)]);
    fprintf(fid,[' BestExposure1 ',num2str(BE)]);
    display(['Error! p: ',num2str(p),' z9=',num2str(z9),' DOF: ',num2str(DOF)]);
    fprintf(fid,'\n');fclose(fid);
    disconnectprolith;
    return;
end;

% print output values to text file
fprintf(fid,[' Line/s/Ss_UDOF ',num2str(UDOF),' Line/s/Ss_BF ',num2str(UBF)]);
fprintf(fid,[' BestFocus1 ',num2str(BF)]);
fprintf(fid,[' BestExposure1 ',num2str(BE)]);
fprintf(fid,[' DOF ',num2str(DOF)]);
fprintf(fid,[' BestFocusSspace ',num2str(BFSspace)]);
fprintf(fid,[' BestExposureSspace ',num2str(BESspace)]);
fprintf(fid,[' DOFSspace ',num2str(DOFSspace)]);
fprintf(fid,[' BestFocusspace ',num2str(BFspace)]);
fprintf(fid,[' BestExposurespace ',num2str(BEspace)]);
fprintf(fid,[' DOFspace ',num2str(DOFspace)]);
%_____________________________________________________________________________
% Smaller FE within DOF to determine polynomial tilt
%_____________________________________________________________________________
if measure_tilt==1
    E_num=7;
    E_start=(1-EL/2)*BE;
    E_stop=(1+EL/2)*BE;
    E_step=0.999*(E_stop-E_start)/(E_num-1);
    E_small=E_start:E_step:E_stop;
    F_num=20;
    FL=DOF/4; %+/- Focus Latitude: Half DOF
    F2_start=(BF-FL);
    F2_stop=BF+FL;
    F2_step=(F2_stop-F2_start)/(F_num-1);
    Focus2=F2_start:F2_step:F2_stop;
    % input parameters to vary for FEM
    % Exposure
    invoke(MPPI_PROLITHSIMENGINE, 'AddInput', 29101, E_start,E_stop,E_step,0.4);
    % Focus
    invoke(MPPI_PROLITHSIMENGINE, 'AddInput', 29102, F2_start,F2_stop,F2_step,F);
    invoke(MPPI_PROLITHSIMENGINE, 'AddOutput', 21); % Resist CD
    invoke(MPPI_PROLITHSIMENGINE, 'SimulationRun');
    while invoke(MPPI_PROLITHSIMENGINE, 'IsDataSetReady') == 0; % Error Handling
        pause(0.2);
    end
```

```
nrr = double(invoke(MPPI_PROLITHSIMENGINE, 'NumResultsRecords'));
CD=zeros(E_num,nrr/E_num);
count=0;
for temp=1:F_num
    for temp2=1:E_num
        CD(temp2,temp)=invoke(MPPI_PROLITHSIMENGINE, ...
            'GetMetrologyPlaneSimSetResult', 'line1', 21,count);
        count=count+1;
    end;
end;
% Replacing negative values with 0 to prevent errors
while min(min(CD))<0
    [CDarray,Iarray]=min(CD);
    [~,Iarray2]=min(CDarray);
    [~,It]=min(CDarray);
    CD(Iarray(It),Iarray2)=0;
end;
% Create arrays for CD vs focus for each exposure
for i = 1:length(E_small)
    eval(['CD' num2str(i) '=CD(' num2str(i) ',1:' num2str(length(Focus2)) ');']);
end
%Polynomial Fit to find Slope
n=4; %polynomial order
for i = 1:length(E_small)
    eval(['[pf' num2str(i) ',S' num2str(i) ',MU' num2str(i) ...
        ']=polyfit(Focus2,CD' num2str(i) ',n);']);
end
if plot_FE==1
    %Plot FE matrix
    figure;
    for i = 1:length(E_small)
        % Use handle property to control color of line
        h=plot(Focus2, eval(['CD' num2str(i) ]), '.-');
        hold on
    end
    hold on; plot(Focus2, linspace(s,s,length(Focus2)),'k--');
    hold on; plot(Focus2, linspace(s*1.1,s*1.1,length(Focus2)),'r--');
    hold on; plot(Focus2, linspace(s*0.9,s*0.9,length(Focus2)),'r--');
    xlabel('Focus um');
    ylabel('Aerial Image CD');
    % Create legend
    for i=1:length(E_small)
        legend_array{i}=num2str(E_small(i));
    end;
    legend_array{length(E_small)+1}='Target';
    legend_array{length(E_small)+2}='CD Spec';
    legend_array{length(E_small)+3}='CD Spec';
    for i=4+length(E_small):3+length(E_small)*2
        legend_array{i}=['fit ',num2str(E_small(i-3-length(E_small)))];
    end;
    for i = 1:length(E_small)
        [~]=plot(Focus2, eval(['pf' num2str(i) '(1)*((Focus2-MU' num2str(i)...
            '(1))/MU' num2str(i) '(2)).^(n)+pf' num2str(i) '(2)*((Focus2-MU'...
            num2str(i) '(1))/MU' num2str(i) '(2)).^(n-1)+pf' num2str(i)...
            '(3)*((Focus2-MU' num2str(i) '(1))/MU' num2str(i) '(2)).^(2)+pf'...
            num2str(i) '(4)*((Focus2-MU' num2str(i) '(1))/MU' num2str(i)...
            '(2)).^1+pf' num2str(i) '(n+1)']), 'g--');
        hold on
    end
    legend(legend_array);
    title(['Prolith FEM with ',num2str(n),'th order regression for pitch='...
        ,num2str(p),'nm']);
end;
% Calculate average tilt and absolute tilt
tilt1=0;
absolute_tilt=0;
for i=1:length(E_small)
    tilt1=eval(['pf' num2str(i) '(n)+tilt1']);
    absolute_tilt=eval(['abs(pf' num2str(i) '(n))+absolute_tilt']);
end;
tilt1=tilt1/length(E_small);
```

```
    absolute_tilt=absolute_tilt/length(E_small);
    fprintf(fid,[' Tilt1 ',num2str(tilt1)]);
    fprintf(fid,[' ABStilt1 ',num2str(absolute_tilt)]);

end;
display(['p: ',num2str(p),' coef: ',num2str(z9),'/',num2str(z16),'/',num2str(z25),...
    ' UDOF3= ',num2str(UDOF)]);
fclose(fid); %close text file
disconnectprolith; %disconnect from Prolith
```

10. APPENDIX B

- Maximization of a merit function (the UDOF from the script in Appendix A)

Script accepts the following input parameters:

- p: pitch (nm) - number
- filename: name of text file where input and output values will be written - string

```
%_____________________________________________________________________
% function: MKS_Optimization.m
% Uses mutation-only evolutionary strategy (ES) algorithm to maximize a
% merit value (UDOF)
% Author: Monica Kempsell Sears
% Nanolithography Research Labs, RIT
%_____________________________________________________________________

function [solution]=MKS_Optimization(p,filename)
tic;  % measures runtime
fid = fopen(filename, 'at');
num_var=3; %Number of variables:
done=zeros(10000,num_var); % Store calculated parameter combinations
done_counter=1;
num_children=8; % Number of children to generate from each parent
num_parents=5; % Number of top candidates to become a parent
iterations=10; % number of iterations
lamda=num_children*num_parents; % Population size
pop_size=round(lamda^(1/num_var))^num_var; %initial pop size from cartesian grid

% Display merit value through each iteration if display_on=1;
display_on=1;
str=sprintf('iterations %d pop size %d num_parents %d num_children %d'...
    ,iterations,pop_size,num_parents,num_children);
display(str); fprintf(fid,[str,'\n']);

% Generate initial pop using Cartesian Grid
z9_var_range=0.08; % range from 0 to 0.08
z16_var_range=0.2; % range from -0.1 to 0.1
z25_var_range=0.2; % range from -0.1 to 0.1
c_z9=z9_var_range*linspace(0,1,round(lamda^(1/num_var))); %Primary Spherical candidates
c_z16=z16_var_range*linspace(0,1,round(lamda^(1/num_var)))-z16_var_range/2; % Secondary
c_z25=z25_var_range*linspace(0,1,round(lamda^(1/num_var)))-z25_var_range/2; % Tertiary

extra_rand=13; % number of candidates to initialize randomly
initial_pop=zeros(pop_size+extra_rand,num_var); filler=1; %initial pop
for k=1:round(lamda^(1/num_var))
    for l=1:round(lamda^(1/num_var))
        for m=1:round(lamda^(1/num_var))
            initial_pop(filler,:)=[c_z9(k),c_z16(l),c_z25(m)];
            filler=filler+1;
        end;
    end;
end;

%Additional initial conditions generated randomly ON GRID OF 0.01
for i=1:extra_rand
    initial_pop(pop_size+i,:)=[(randi(100*z9_var_range,1,1))/100,...
```

```
        (randi(100*z16_var_range,1,1))/100-z16_var_range/2,...
        (randi(100*z25_var_range,1,1))/100-z25_var_range/2];
end;

% Grade each individual
merit=zeros(1,pop_size+extra_rand);
if display_on==1
    display(' Iteration: 0');
end;
for i=1:pop_size+extra_rand
    [merit(i)]=AltPSM(p,initial_pop(i,1),initial_pop(i,2),initial_pop(i,3),filename);
    done(done_counter,:)=initial_pop(i,:); % Saves calculated candidates
    done_counter=done_counter+1;
end;
MaxMerit=max(merit);
if display_on==1
    display(['Iteration = 0: the max UDOF value= ',num2str(MaxMerit)]);
end;

% Start iterations with mutation
count=0;
while MaxMerit<100 && count<iterations
    count=count+1;
    % Find num_parents best solutions
    best_parents=zeros(num_parents,num_var);
    [save_error,index]=sort(merit,'descend'); %descend for maximize
    for i=1:num_parents
        if count==1
            best_parents(i,:)=initial_pop(index(i),:);
        else
            best_parents(i,:)=pop(index(i),:);
        end;
    end;

    %Generate children
    pop=zeros(lamda+num_parents,num_var); % Also store best parents
    %Generate num_children for each num_parents
    filler=1;
    mutation=0.01; % Child is mutated in each coordinate by this value
    for i=1:num_parents
        pop(filler,:)  =[best_parents(i,1)-mutation,best_parents(i,2)...
            -mutation,best_parents(i,3)-mutation];
        pop(filler+1,:)=[best_parents(i,1)+mutation,best_parents(i,2)-mutation,...
            best_parents(i,3)-mutation];
        pop(filler+2,:)=[best_parents(i,1)-mutation, best_parents(i,2)+mutation,...
            best_parents(i,3)- mutation];
        pop(filler+3,:)=[best_parents(i,1)+mutation, best_parents(i,2)+mutation,...
            best_parents(i,3)- mutation];
        pop(filler+4,:)=[best_parents(i,1)-mutation, best_parents(i,2)-mutation,...
            best_parents(i,3)+ mutation];
        pop(filler+5,:)=[best_parents(i,1)+mutation, best_parents(i,2)-mutation,...
            best_parents(i,3)+ mutation];
        pop(filler+6,:)=[best_parents(i,1)-mutation, best_parents(i,2)+mutation,...
            best_parents(i,3)+ mutation];
        pop(filler+7,:)=[best_parents(i,1)+mutation, best_parents(i,2)+mutation,...
            best_parents(i,3)+ mutation];
        pop(filler+8,:)=best_parents(i,:);
        filler=filler+9;
    end;

    % Grade each individual
    merit=zeros(1,lamda+num_parents);
    if display_on==1
        display([' Iteration: ',num2str(count)]);
    end;
    for i=1:lamda+num_parents
        %check if in done - TABU SEARCH
        tf=ismember(done,pop(i,:),'rows');
        call_merit=1;
        if max(tf)>0
            % Secondary sampling points located on a 3D cross centered on grid point
```

```
            % unrandom mutation
            if     max(ismember(done,[pop(i,1)-mutation,pop(i,2),pop(i,3)],'rows'))==0
                pop(i,:)  =[pop(i,1)-mutation, pop(i,2),pop(i,3)];
            elseif max(ismember(done,[pop(i,1)+mutation, pop(i,2),pop(i,3)],'rows'))==0
                pop(i,:)  =[pop(i,1)+mutation, pop(i,2),pop(i,3)];
            elseif max(ismember(done,[pop(i,1),pop(i,2) -mutation,pop(i,3)],'rows'))==0
                pop(i,:)  =[pop(i,1),pop(i,2) -mutation,pop(i,3)];
            elseif max(ismember(done,[pop(i,1),pop(i,2) +mutation,pop(i,3)],'rows'))==0
                pop(i,:)  =[pop(i,1),pop(i,2) +mutation,pop(i,3)];
            elseif max(ismember(done,[pop(i,1),pop(i,2), pop(i,3)-mutation],'rows'))==0
                pop(i,:)  =[pop(i,1),pop(i,2), pop(i,3)-mutation];
            elseif max(ismember(done,[pop(i,1),pop(i,2), pop(i,3)+mutation],'rows'))==0
                pop(i,:)  =[pop(i,1),pop(i,2), pop(i,3)+mutation];
            % a random mutation
            else
                pop(i,:)  =[pop(i,1)+randi([-10 10],1,1) *mutation,pop(i,2)+...
                    randi([-10 10],1,1)*mutation,pop(i,3)+randi([-10 10],1,1)*mutation];
                if max(ismember(done,[pop(i,1),pop(i,2), pop(i,3)],'rows'))>0
                    call_merit=0;
                    display('Already done');
                end;
            end;
        end;
        if call_merit==1
            [merit(i)]=AltPSM(p,pop(i,1),pop(i,2),pop(i,3),filename);
            done(done_counter,:)=pop(i,:);
        end;
        if done_counter<length(done)
            done_counter=done_counter+1;
        else
            done_counter=1;
            display(['Error: Done Counter=',num2str(done_counter),' not long enough']);
        end;
    end;
    % Append mu to new pop: 'mu+lamda'
    for i=1:num_parents
        pop(lamda+i,:)=best_parents(i,:);
        merit(lamda+i)=save_error(i);
    end;
    MaxMerit=max(merit);
    if display_on==1
        display(['Iteration = ',num2str(count),': the max UDOF= ',num2str(MaxMerit)]);
    end;
end;

% After all iterations, find solution with lowest error
[~,index]=sort(merit,'descend');
solution=pop(index(1),:);
display(['Final MeritValue: ',num2str(solution)]);
tElapsed=toc;
display(['Time Elapsed: ',num2str(tElapsed/(60*60)),' hr']);
```

11. REFERENCES

[1] D. Englebart, "Microelectronics and the art of similitude," *IEEE International Solid-State Circuits Conference*, vol. III, pp. 76 –77, Feb. 1960.

[2] G. Moore, "Cramming more components onto integrated circuits," *Electronics*, vol. 38, no. 8, pp. 114–117, Apr. 1965.

[3] G. E. Moore, "Progress in digital integrated electronics," *IEEE International Electron Devices Meeting*, vol. 21, pp. 11 – 13, 1975.

[4] G. E. Moore, "Lithography and the future of Moore's law," *Proc. SPIE*, vol. 2438, no. 1, pp. 2–17, Jun. 1995.

[5] B. Lin, "The 157-nm Good/Bad News from Intel," *J. Micro/Nanolith. MEMS MOEMS*, vol. 2, no. 3, pp. 165–166, Jul. 2003.

[6] V. Bakshi and A. Yen, "Special Section Guest Editorial: EUV Sources for Lithography," *J. Micro/Nanolith. MEMS MOEMS*, vol. 11, no. 2, pp. 021101–1, Jun. 2012.

[7] C.-T. Wu, H. M. Lin, W.-M. Wu, M.-H. Chan, B. S. Lin, K.-H. Lin, A. J. Hazelton, T. Ohhashi, K. Nakano, Y. Iriuchijima, C. Lee, and L. Hung, "The rapid introduction of immersion lithography for NAND flash: challenges and experience," *Proc. SPIE*, vol. 6924, p. 69241A–10, 2008.

[8] K. Lucas, C. Cork, B. Yu, G. Luk-Pat, B. Painter, and D. Z. Pan, "Implications of triple patterning for 14nm node design and patterning," *Proc. SPIE*, vol. 8327, p. 832703, Mar. 2012.

[9] Bruce W. Smith, "Optics for Photolithography," in *Microlithography: Science and Technology*, 2nd ed., Bruce W. Smith and Kazuaki Suzuki, Eds. Boca Raton: CRC Press, 2007, pp. 149–242.

[10] B. Lin, "Where is the lost resolution?," *Proc. SPIE*, vol. 633, pp. 44–50, 1986.

[11] W. J. Smith, E. Betensky, D. Williamson, J. C. Minano, and R. J. Koshel, "The past, present, and future of optical design," *Proc. SPIE*, vol. 6342, p. 63422Y–32, 2006.

[12] D. M. Williamson, "Evolution of ring-field systems in microlithography," *Proc. SPIE*, vol. 3482, pp. 369–376, 1998.

[13] D. M. Williamson, "Remaining challenges in microlithographic optical design," *Proc. SPIE*, vol. 5874, p. 58740N–12, 2005.

[14] Michael S. Hibbs, "System Overview of Optical Steppers and Scanners: Optical Considerations," in *Microlithography: Science and Technology*, 2nd ed., Bruce Smith and Kazuaki Suzuki, Eds. Boca Raton: CRC Press, 2007, p. 31.

[15] C. A. Mack, "Aerial Image Formation - The Details," in *Fundamental principles of optical lithography the science of microfabrication*, Hoboken: Wiley, 2007, pp. 83–84.

[16] C. A. Mack, "Defocus as an aberration," in *Fundamental principles of optical lithography the science of microfabrication*, Hoboken: Wiley, 2007, pp. 95–97.

[17] J. W. Bossung, "Projection Printing Characterization," *Proc. SPIE*, vol. 100, p. 80, Jan. 1977.

[18] C. A. Mack, "PROLITH: A comprehensive optical lithography model," *Proc. SPIE*, vol. 538, pp. 207–220, 1985.
[19] C. A. Mack and J. D. Byers, "New model for focus-exposure data analysis," *Proc. SPIE*, vol. 5038, pp. 396–405, 2003.
[20] G. Airy, "On the Diffraction of an Object-glass with Circular Aperture," *Transactions of the Cambridge Philosophical Society*, vol. 5, no. 3, pp. 283–291, 1835.
[21] *Techniques of microphotography: precision photography at extreme reductions*. Eastman Kodak Industral Data Book No. P-52, pp. 4-14, 1963.
[22] B. Saleh and S. Sayegh, "Reduction of errors of microphotographic reproductions by optimal corrections of original masks," *Optical Engineering*, vol. 20, no. 5, pp. 781–784, 1981.
[23] S. I. Sayegh and B. E. A. Saleh, "Image Design: Generation of a Prescribed Image at the Output of a Band-Limited System," *IEEE Transactions on Pattern Analysis and Machine Intelligence*, vol. 5, no. 4, pp. 441 –445, Jul. 1983.
[24] B. Saleh and K. Nashold, "Image construction: optimum amplitude and phase masks in photolithography," *Applied Optics*, vol. 24, no. 10, pp. 1432–1437, 1985.
[25] P. D. Robertson, F. W. Wise, A. N. Nesr, A. R. Neureuther, and C. H. Ting, "Proximity effects and influences of nonuniform illumination in projection lithography," *Proc. SPIE*, vol. 334, pp. 37–43, 1982.
[26] A. C. Liu and B. J. Lin, "A study of projected optical images for typical IC mask patterns illuminated by partially coherent light," *IEEE Transactions on Electron Devices*, vol. 30, no. 10, pp. 1251 – 1263, Oct. 1983.
[27] A. E. Rosenbluth, D. Goodman, and B. J. Lin, "A critical examination of submicron optical lithography using simulated projection images," *J. Vac. Sci. Technol. B*, vol. 1, no. 4, pp. 1190 –1195, Oct. 1983.
[28] P. Chien and M. Chen, "Proximity effects in submicron optical lithography," *Proc. SPIE*, vol. 772, pp. 35–40, 1987.
[29] B. W. Smith and D. E. Ewbank, "OPC and image optimization using localized frequency analysis," *Proc. SPIE*, vol. 4691, pp. 148–157, 2002.
[30] Y. Nissan-Cohen, P. Frank, E. W. Balch, B. Thompson, K. Polasko, and D. M. Brown, "Variable Proximity Corrections for Submicron Optical Lithographic Masks," *IEEE Symposium on VLSI Technology*, pp. 13 –14, May 1987.
[31] N. Shamma, F. Sporon-Fiedler, and E. Lin, "A method for correction of proximity effect in optical projection lithography," *Proc. KTI Microlithography Seminar Interface*, pp. 145–156, 1991.
[32] O. W. Otto, J. G. Garofalo, K. K. Low, C.-M. Yuan, R. C. Henderson, C. Pierrat, R. L. Kostelak, S. Vaidya, and P. K. Vasudev, "Automated optical proximity correction: a rules-based approach," *Proc. SPIE*, vol. 2197, no. 1, pp. 278–293, May 1994.
[33] E. Tamechika, T. Horiuchi, and K. Harada, "Resolution Improvement Using Auxiliary Pattern Groups in Oblique Illumination Lithography," *Jpn. J. Appl. Phys.*, vol. 32, no. Part 1, No. 12B, pp. 5856–5862, Dec. 1993.
[34] B. J. Lin, A. M. Moruzzi, and A. E. Rosenbluth, "Lithographic process having improved image quality," U.S. Patent 4902899Feb-1990.

[35] J. F. Chen and J. A. Matthews, “Mask for photolithography,” U.S. Patent 5242770Sep-1993.
[36] T. Ito, M. Tanuma, Y. Morooka, and K. Kadota, “Photo-projection image distortion correction for a 1-μm pattern process,” *Electronics and Communications in Japan Part II: Electronics*, vol. 69, no. 3, pp. 30–38, 1986.
[37] A. Starikov, “Use of a single size square serif for variable print bias compensation in microlithography: method, design, and practice,” *Proc. SPIE*, vol. 1088, pp. 34–46, 1989.
[38] F. M. Schellenberg, “Resolution enhancement technology: the past, the present, and extensions for the future,” *Proc. SPIE*, vol. 5377, pp. 1–20, 2004.
[39] D. Gabor, “Theory of communication. Part 3: Frequency compression and expansion,” *Journal of the Institution of Electrical Engineers - Part III: Radio and Communication Engineering*, vol. 93, no. 26, pp. 445 –457, Nov. 1946.
[40] J. P. Stirniman and M. L. Rieger, “Fast proximity correction with zone sampling,” *Proc. SPIE*, vol. 2197, no. 1, pp. 294–301, May 1994.
[41] N. B. Cobb, “Fast Optical and Process Proximity Correction Algorithms for Integrated Circuit Manufacturing,” University of California at Berkeley, Berkeley, 1998.
[42] Y. Hirai, N. Nomura, A. Misaka, S. Hayama, K. Yamashita, and K. Harafuji, “Computer Aided Proximity Effect Correction System in Photolithography,” *Jpn. J. Appl. Phys.*, vol. 28, no. Part 1, No. 10, pp. 2049–2052, Oct. 1989.
[43] C. A. Spence, J. L. Nistler, E. Barouch, U. Hollerbach, and S. A. Orszag, “Automated determination of CAD layout failures through focus: experiment and simulation,” *Proc. SPIE*, vol. 2197, no. 1, pp. 302–313, May 1994.
[44] N. B. Cobb and A. Zakhor, “Fast sparse aerial-image calculation for OPC,” *Proc. SPIE*, vol. 2621, no. 1, pp. 534–545, Oct. 1995.
[45] M. C. Lam and K. Adam, “Understanding the impact of rigorous mask effects in the presence of empirical process models used in optical proximity correction (OPC),” *Proc. SPIE*, vol. 6520, p. 65203M–9, 2007.
[46] P. Liu, Y. Cao, L. Chen, G. Chen, M. Feng, J. Jiang, H. Liu, S. Suh, S.-W. Lee, and S. Lee, “Fast and accurate 3D mask model for full-chip OPC and verification,” *Proc. SPIE*, vol. 6520, p. 65200R–12, 2007.
[47] Lord Rayleigh, “On the Theory of Optical Images, with special reference to the Microscope,” *The London, Edinburgh, and Dublin Philosophical Magazine and Journal of Science*, vol. 42, no. 5, pp. 167–195, 1896.
[48] Lord Rayleigh, “Investigations in optics, with special reference to the spectroscope,” *The London, Edinburgh, and Dublin Philosophical Magazine and Journal of Science*, vol. 8, no. 49, pp. 261–264,403–411, 477–480, 1879.
[49] H. Hänsel and W. Polack, “Verfahren zur Herstellung einer Phasenmaske mit Amplitudenstruktur [Process for the production of a phase mask with amplitude structure],” U.S. Patent 126361Jul-1977.
[50] D. C. Flanders and H. I. Smith, “Spatial period division exposing,” U.S. Patent 4360586Nov-1982.
[51] D. Goodman, “Some partially coherent images,” *Optical Sciences Center Newsletter*, vol. 12, no. 1, pp. 5–7, 1978.

[52] M. Shibuya, “Projection master for use with transmitted illumination,” U.S. Patent Sho 57-62052Apr-1982.
[53] M. D. Levenson, N. S. Viswanathan, and R. A. Simpson, “Improving resolution in photolithography with a phase-shifting mask,” *IEEE Transactions on Electron Devices*, vol. 29, no. 12, pp. 1828 – 1836, Dec. 1982.
[54] M. D. Levenson, D. S. Goodman, S. Lindsey, P. W. Bayer, and H. A. E. Santini, “The phase-shifting mask II: Imaging simulations and submicrometer resist exposures,” *IEEE Transactions on Electron Devices*, vol. 31, no. 6, pp. 753 – 763, Jun. 1984.
[55] A. Nitayama, T. Sato, K. Hashimoto, F. Shigemitsu, and M. Nakase, “New phase shifting mask with self-aligned phase shifters for a quarter micron photolithography,” *IEEE International Electron Devices Meeting*, pp. 57 –60, Dec. 1989.
[56] F. M. Schellenberg, D. Levenson, and P. J. Brock, “Optimization of real phase-mask performance,” *Proc. SPIE*, vol. 1604, no. 1, pp. 274–296, Jan. 1992.
[57] A. S. Wong, D. M. Newmark, J. B. Rolfson, R. J. Whiting, and A. R. Neureuther, “Investigating phase-shifting mask layout issues using a CAD toolkit,” *IEEE International Electron Devices Meeting*, vol. 91, pp. 705 –708, Dec. 1991.
[58] D. M. Newmark and A. R. Neureuther, “Phase-shifting mask design tool,” *Proc. SPIE*, vol. 1604, no. 1, pp. 226–235, Jan. 1992.
[59] M. D. Prouty and A. R. Neureuther, “Optical imaging with phase shift masks,” *Optical Microlithography: Technology for the Next Decade*, vol. 470, pp. 228–232, 1984.
[60] G. Galan, F. Lalanne, P. Schiavone, and J.-M. Temerson, “Application of Alternating-Type Phase Shift Mask to Polysilicon Level for Random Logic Circuits,” *Jpn. J. Appl. Phys.*, vol. 33, no. Part 1, No. 12B, pp. 6779–6784, Dec. 1994.
[61] K. Ooi, S. Hara, and K. Koyama, “Computer Aided Design Software for Designing Phase-Shifting Masks,” *Jpn. J. Appl. Phys.*, vol. 32, pp. 5887–5891, 1993.
[62] K. Ooi, K. Koyama, and M. Kiryu, “Method of Designing Phase-Shifting Masks Utilizing a Compactor,” *Jpn. J. Appl. Phys.*, vol. 33, no. 12B, pp. 6774–6778, Dec. 1994.
[63] A. Moniwa, T. Terasawa, K. Nakajo, J. Sakemi, and S. Okazaki, “Heuristic Method for Phase-Conflict Minimization in Automatic Phase-Shift Mask Design,” *Jpn. J. Appl. Phys.*, vol. 34, pp. 6584–6589, 1995.
[64] Michael S. Hibbs, “System Overview of Optical Steppers and Scanners: Latent Image Formation,” in *Microlithography: Science and Technology*, 2nd ed., Bruce Smith and Kazuaki Suzuki, Eds. Boca Raton: CRC Press, 2007, pp. 34–36.
[65] H. I. Smith, E. H. Anderson, and M. L. Schattenburg, “Lithography mask with a .pi.-phase shifting attenuator,” U.S. Patent 4890309Dec-1989.
[66] B. Lin, “The attenuated phase-shifting mask,” *Solid State Technology*, vol. 35, no. 1, p. 43, Jan. 1992.
[67] E. Tamechika, S. Matsuo, K. Komatsu, Y. Takeuchi, Y. Mimura, and K. Harada, “Investigation of single sideband optical lithography using oblique incidence illumination,” *J. Vac. Sci. Technol. B*, vol. 10, no. 6, pp. 3027 –3031, Nov. 1992.
[68] Bruce W. Smith, “Optics for Photolithography: Optical Image Enhancement Techniques,” in *Microlithography: Science and Technology*, 2nd ed., Bruce W. Smith and Kazuaki Suzuki, Eds. Boca Raton: CRC Press, 2007, pp. 211–216.

[69] M. D. Levenson, “Wavefront Engineering for Photolithography,” *Physics Today*, vol. 46, no. 7, pp. 28–36, 1993.
[70] X. Ma and G. R. Arce, “Generalized inverse lithography methods for phase-shifting mask design,” *Opt. Express*, vol. 15, pp. 15066–15079, 2007.
[71] R. Walton, “Photoblanks for advanced lithography,” *Solid State Technology*, vol. 46, p. 26, 2003.
[72] M. Yoshizawa, V. Philipsen, L. H. A. Leunissen, E. Hendrickx, R. Jonckheere, G. Vandenberghe, U. Buttgereit, H. Becker, C. Koepernik, and M. Irmscher, “Comparative study of bi-layer attenuating phase-shifting masks for hyper-NA lithography,” *Proc. SPIE*, vol. 6283, p. 62831G–9, 2006.
[73] M. Yoshizawa, V. Philipsen, and L. H. A. Leunissen, “Optimizing absorber thickness of attenuating phase-shifting masks for hyper-NA lithography,” *Proc. SPIE*, vol. 6154, p. 61541E–8, 2006.
[74] B. W. Smith, “Multi-layered attenuated phase shift mask and a method for making the mask,” U.S. Patent 5939227Aug-1999.
[75] V. Philipsen, K. Mesuda, P. De Bisschop, A. Erdmann, G. Citarella, P. Evanschitzky, R. Birkner, R. Richter, and T. Scherubl, “Impact of alternative mask stacks on the imaging performance at NA 1.20 and above,” *Proc. SPIE*, vol. 6730, p. 67301N, 2007.
[76] V. Philipsen, P. De Bisschop, and K. Mesuda, “Mask transmission resonance in bi-layer masks,” *Proc. SPIE*, vol. 7028, pp. 702815–8, 2008.
[77] Z. M. Ma, S. McDonald, and C. Progler, “Revisiting adoption of high transmission PSM: pros, cons and path forward,” Taipei, Taiwan, 2009, vol. 7520, pp. 752017–15.
[78] M.-C. Yang, “Analytical optimization of high-transmission attenuated phase-shifting reticles,” *J. Micro/Nanolith. MEMS MOEMS*, vol. 8, pp. 013015–7, 2009.
[79] N. Kachwala, J. S. Petersen, and M. McCallum, “High-transmission attenuated PSM: benefits and limitations through a validation study of 33%, 20%, and 6% transmission masks,” *Proc. SPIE*, vol. 4000, pp. 1163–1174, 2000.
[80] C. Koepernik, H. W. Becker, J. Butschke, U. Buttgereit, M. Irmscher, L. Nedelmann, F. Schmidt, and S. Teuber, “Patterning of Ta/SiO2 high transmission EAPSM material for 193nm technology,” *Proc. SPIE*, vol. 5853, pp. 463–473, 2005.
[81] O. Nozawa, Y. Shiota, H. Mitsui, T. Suzuki, Y. Ohkubo, M. Ushida, S. Yusa, T. Nishimura, K. Noguchi, S. Sasaki, H. Mohri, and N. Hayashi, “Development of attenuating PSM shifter for F2 and high-transmission ArF lithography,” *Proc. SPIE*, vol. 5130, pp. 39–50, 2003.
[82] K. Sakajiri, A. Trichkov, Y. Granik, E. Hendrickx, G. Vandenberghe, M. Kempsell, G. Fenger, K. Boehm, and T. Scheruebl, “Application of pixel-based mask optimization technique for high transmission attenuated PSM,” *Proc. SPIE*, vol. 7275, p. 72750X–11, 2009.
[83] M. Cheng, B. C. P. Ho, and D. E. Guenther, “Impact of mask topography and resist effects on optical proximity correction in advanced alternating phase-shift process,” *Proc. SPIE*, vol. 5040, pp. 313–326, 2003.
[84] C. Pierrat, A. K. K. Wong, S. Vaidya, and M. Vernon, “Phase-shifting mask topography effects on lithographic image quality,” *Proc. SPIE*, vol. 1927, pp. 28–41, 1993.

[85] C. M. Friedrich, L. Mader, A. Erdmann, S. List, R. L. Gordon, C. K. Kalus, U. A. Griesinger, R. Pforr, J. Mathuni, G. G. Ruhl, and W. Maurer, "Optimizing edge topography of alternating phase-shift masks using rigorous mask modeling," *Proc. SPIE*, vol. 4000, pp. 1323–1335, 2000.
[86] W.-H. Cheng, K. K. Chakravorty, and J. N. Farnsworth, "Alternating phase shift mask architecture scalability, implementations, and applications for 90-nm and 65-nm technology nodes and beyond," *Proc. SPIE*, vol. 5130, pp. 766–777, 2003.
[87] R. L. Gordon, C. A. Mack, and J. S. Petersen, "Design and analysis of manufacturable alternating phase-shifting masks," *Proc. SPIE*, vol. 3546, pp. 606–616, 1998.
[88] D. J. Gerold, J. S. Petersen, and D. Levenson, "Multiple pitch transmission and phase analysis of six types of strong phase-shifting masks," *Proc. SPIE*, vol. 4346, pp. 729–743, 2001.
[89] M. D. Levenson, T. Ebihara, and M. Yamachika, "SCAA mask exposures and Phase Phirst designs for 100 nm and below," *Proc. SPIE*, vol. 4346, pp. 817–826, 2001.
[90] "Dr.LiTHO: Rigorous Electromagnetic Field Modeling." [Online]. Available: http://www.drlitho.com/cms/website.php?id=/en/research/emf.html. [Accessed: 02-Oct-2012].
[91] E. Abbe, "Beiträge zur Theorie des Mikroskops und der mikroskopischen Wahrnehmung [Contributions to the theory of the microscope and the nature of microscopic vision]," *Archive for Microscopic Anatomy*, 1873.
[92] A. Porter, "On the diffraction theory of microscopic vision," *The London, Edinburgh, and Dublin Philosophical Magazine and Journal of Science*, vol. 11, no. 61, pp. 154–166, Jan. 1906.
[93] G. O. Reynolds, "A concept for a high resolution optical lithographic system for producing one-half micron linewidths," *Proc. SPIE*, vol. 633, pp. 228–238, 1986.
[94] C. A. Mack, "Optimum stepper performance through image manipulation," *Proc. KTI Microlithography Seminar Interface*, pp. 209–215, 1989.
[95] D. L. Fehrs, H. B. Lovering, and R. T. Scruton, "Illuminator modification of an optical aligner," *Proc. KTI Microlithography Seminar Interface*, pp. 217–230, 1989.
[96] S. Matsuo, K. Komatsu, Y. Takeuchi, E. Tamechika, Y. Mimura, and K. Harada, "High resolution optical lithography system using oblique incidence illumination," *IEEE International Electron Devices Meeting*, pp. 970 –972, Dec. 1991.
[97] A. E. Rosenbluth, S. J. Bukofsky, M. S. Hibbs, K. Lai, A. F. Molless, R. N. Singh, and A. K. Wong, "Optimum mask and source patterns to print a given shape," *Proc. SPIE*, vol. 4346, pp. 486–502, 2001.
[98] M. Burkhardt, A. Yen, C. Progler, and G. Wells, "Illuminator design for the printing of regular contact patterns," *Microelectronic Engineering*, vol. 41–42, pp. 91–95, 1998.
[99] E. Barouch, S. L. Knodle, S. A. Orszag, and M. S. Yeung, "Illuminator optimization for projection printing," *Proc. SPIE*, vol. 3679, pp. 697–703, 1999.
[100] S. Asai, I. Hanyu, and K. Hikosaka, "Improving projection lithography image illumination by using sources far from the optical axis," *J. Vac. Sci. Technol. B*, vol. 9, no. 6, pp. 2788 –2791, Nov. 1991.

[101] S. Asai, I. Hanyu, and K. Hikosaka, "High performance optical lithography using a separated light source," *J. Vac. Sci. Technol. B*, vol. 10, no. 6, pp. 3023 –3026, Nov. 1992.
[102] S. Asai, I. Hanyu, and M. Takikawa, "New effects of modified illumination in optical lithography," *IEEE Electron Device Letters*, vol. 14, no. 3, pp. 110 –112, Mar. 1993.
[103] M. Noguchi, M. Muraki, Y. Iwasaki, and A. Suzuki, "Subhalf-micron lithography system with phase-shifting effect," *Proc. SPIE*, vol. 1674, no. 1, pp. 92–104, Jun. 1992.
[104] N. Shiraishi, S. Hirukawa, Y. Takeuchi, and N. Magome, "New imaging technique for 64M-DRAM," *Proc. SPIE*, vol. 1674, no. 1, pp. 741–752, Jun. 1992.
[105] K. Kamon, T. Miyamoto, Y. Myoi, H. Nagata, N. Kotani, and M. Tanaka, "Photolithography System Using a Combination of Modified Illumination and Phase Shift Mask," *Jpn. J. Appl. Phys.*, vol. 31, pp. 4131–4136, 1992.
[106] T. A. Brunner, "Rim phase-shift mask combined with off-axis illumination: a path to .5Λ/NA geometries," *Proc. SPIE*, vol. 1927, no. 1, pp. 54–62, Aug. 1993.
[107] R. J. Socha, M. V. Dusa, L. Capodieci, J. Finders, J. F. Chen, D. G. Flagello, and K. D. Cummings, "Forbidden pitches for 130-nm lithography and below," *Proc. SPIE*, pp. 1140–1155, Jul. 2000.
[108] B. W. Smith, "Illumination device for projection system and method for fabricating," U.S. Patent RE40239Apr-2008.
[109] T. Ogawa, M. Uematsu, T. Ishimaru, M. Kimura, and T. Tsumori, "Effective light source optimization with the modified beam for depth-of-focus enhancements," *Proc. SPIE*, vol. 2197, no. 1, pp. 19–30, May 1994.
[110] M. D. Himel, R. E. Hutchins, J. C. Colvin, M. K. Poutous, A. D. Kathman, and A. S. Fedor, "Design and fabrication of customized illumination patterns for low-k1 lithography: a diffractive approach," *Proc. SPIE*, vol. 4346, pp. 1436–1442, 2001.
[111] J. Zimmermann, P. Graupner, J. T. Neumann, D. Hellweg, D. Jurgens, M. Patra, C. Hennerkes, M. Maul, B. Geh, A. Engelen, O. Noordman, M. Mulder, S. Park, and J. De Vocht, "Generation of arbitrary freeform source shapes using advanced illumination systems in high-NA immersion scanners," *Proc. SPIE*, vol. 7640, pp. 764005–15, 2010.
[112] Y. Granik, "Source optimization for image fidelity and throughput," *J. Micro/Nanolith. MEMS MOEMS*, vol. 3, no. 4, pp. 509–522, Oct. 2004.
[113] R. Socha, "Freeform and SMO," *Proc. SPIE*, vol. 7973, pp. 797305–17, 2011.
[114] J. Bekaert, B. Laenens, S. Verhaegen, L. Van Look, D. Trivkovic, F. Lazzarino, G. Vandenberghe, P. van Adrichem, R. Socha, S. Hsu, H.-Y. Liu, O. Mouraille, K. Schreel, M. Dusa, J. Zimmermann, P. Gräupner, and J. T. Neumann, "Experimental verification of source-mask optimization and freeform illumination for 22-nm node static random access memory cells," *J. Micro/Nanolith. MEMS MOEMS*, vol. 10, no. 1, pp. 013008–013008–10, Mar. 2011.
[115] A. K. Jaiswal and R. K. Bhogra, "Images of Periodic Objects under Partially Coherent Illumination," *Optica Acta*, vol. 20, no. 6, pp. 469–486, 1973.
[116] J. Garofalo, "Mask assisted off-axis illumination technique for random logic," *J. Vac. Sci. Technol. B*, vol. 11, no. 6, p. 2651, Nov. 1993.

[117] S.-Y. Chou, J.-C. Lou, F.-J. Liang, T.-S. Gau, R.-G. Liu, C.-K. Chen, and C.-M. Lai, "Customized illumination aperture filter design for through-pitch focus latitude enhancement of deep submicron contact hole printing," *J. Micro/Nanolith. MEMS MOEMS*, vol. 1, pp. 296–306, 2002.
[118] M. Bertero, "Linear Inverse and III-Posed Problems," in *Advances in Electronics and Electron Physics*, vol. 75, P. Hawkes, Ed. Geneva: Academic Press, 1989, pp. 1–120.
[119] R. Easton, "Inverse Imaging Problem," in *Fourier Methods in Imaging*, Hoboken: Wiley- Blackwell, 2010, p. 84.
[120] A. Yagola, V. Titarenko, and A. Leonov, "ILL-Posed Problems and a priori information," in *Inverse Problems in Engineering Mechanics III*, Oxford: Elsevier Science Ltd, 2002, pp. 235–244.
[121] T.-S. Gau, R.-G. Liu, C.-K. Chen, C.-M. Lai, F.-J. Liang, and C. C. Hsia, "Customized illumination aperture filter for low k1 photolithography process," *Proc. SPIE*, vol. 4000, pp. 271–282, 2000.
[122] K. Tian, A. Krasnoperova, D. Melville, A. E. Rosenbluth, D. Gil, J. Tirapu-Azpiroz, K. Lai, S. Bagheri, C. Chen, and B. Morgenfeld, "Benefits and trade-offs of global source optimization in optical lithography," *Proc. SPIE*, vol. 7274, p. 72740C–12, 2009.
[123] Y. Granik, "Fast pixel-based mask optimization for inverse lithography," *J. Micro/Nanolith. MEMS MOEMS*, vol. 5, pp. 043002–13, 2006.
[124] M. L. Kempsell, E. Hendrickx, A. Tritchkov, K. Sakajiri, K. Yasui, S. Yoshitake, Y. Granik, G. Vandenberghe, and B. W. Smith, "Inverse lithography for 45-nm-node contact holes at 1.35 numerical aperture," *J. Micro/Nanolith. MEMS MOEMS*, vol. 8, pp. 043001–9, 2009.
[125] Y. Granik, K. Sakajiri, and S. Shang, "On objectives and algorithms of inverse methods in microlithography," *Proc. SPIE*, vol. 6349, p. 63494R–8, 2006.
[126] Y. Borodovsky, W.-H. Cheng, R. Schenker, V. Singh, B. Hu, K. Toh, S. Bollepalli, and S. Wagner, "Pixelated phase mask as novel lithography RET," *Proc. SPIE*, vol. 6924, p. 69240E–14, 2008.
[127] W.-H. Cheng, J. Farnsworth, W. Kwok, A. Jamieson, N. Wilcox, M. Vernon, K. Yung, Y.-P. Liu, J. Kim, E. Frendberg, S. Chegwidden, R. Schenker, Y. Borodovsky, S. Bollepalli, B. Hu, K. Toh, V. Singh, W. Cheng, and S. Wagner, "Fabrication of defect-free full-field pixelated phase mask," *Proc. SPIE*, vol. 6924, p. 69241G–10, 2008.
[128] R. Schenker, S. Bollepalli, B. Hu, K. Toh, V. Singh, K. Yung, W. Cheng, Y. Borodovsky, W.-H. Cheng, and S. Wagner, "Integration of pixelated phase masks for full-chip random logic layers," *Proc. SPIE*, vol. 6924, p. 69240I–11, 2008.
[129] V. Singh, B. Hu, K. Toh, S. Bollepalli, S. Wagner, Y. Borodovsky, and R. Schenker, "Making a trillion pixels dance," *Proc. SPIE*, vol. 6924, p. 69240S–12, 2008.
[130] R. Schenker, V. Singh, and Y. Borodovsky, "The role of strong phase shift masks in Intel's DFM infrastructure development," *Proc. SPIE*, vol. 7641, p. 76410S–9, 2010.

[131] K. Sakajiri, A. Tritchkov, and Y. Granik, “Model-based SRAF insertion through pixel-based mask optimization at 32nm and beyond,” *Proc. SPIE*, vol. 7028, pp. 702811–12, 2008.
[132] R. J. Socha, D. J. Van Den Broeke, S. D. Hsu, J. F. Chen, T. L. Laidig, N. P. Corcoran, U. Hollerbach, K. E. Wampler, X. Shi, and W. E. Conley, “Contact hole reticle optimization by using interference mapping lithography (IML),” *Proc. SPIE*, vol. 5446, pp. 516–534, 2004.
[133] R. Socha, X. Shi, and D. LeHoty, “Simultaneous source mask optimization (SMO),” *Proc. SPIE*, vol. 5853, pp. 180–193, 2005.
[134] A. Poonawala and P. Milanfar, “OPC and PSM design using inverse lithography: a nonlinear optimization approach,” *Proc. SPIE*, vol. 6154, p. 61543H–14, 2006.
[135] H. Fukuda, T. Terasawa, and S. Okazaki, “Spatial filtering for depth of focus and resolution enhancement in optical lithography,” *J. Vac. Sci. Technol. B*, vol. 9, pp. 3113–3116, 1991.
[136] H. Fukuda and R. Yamanaka, “A New Pupil Filter for Annular Illumination in Optical Lithography,” *Jpn. J. Appl. Phys.*, vol. 31, pp. 4126–4130, 1992.
[137] R. M. von Buenau, H. Fukuda, and T. Terasawa, “Effects of radially nonsymmetric pupil filters and multiple-pupil exposure,” *Proc. SPIE*, vol. 2726, pp. 375–385, 1996.
[138] H. Fukuda, Y. Kobayashi, T. Tawa, and S. Okazaki, “Performance of pupil-filtering stepper-lens system,” *Microelectronic Engineering*, vol. 27, pp. 213–216, 1995.
[139] F. Staals, A. Andryzhyieuskaya, H. Bakker, M. Beems, J. Finders, T. Hollink, J. Mulkens, A. Nachtwein, R. Willekers, P. Engblom, T. Gruner, and Y. Zhang, “Advanced wavefront engineering for improved imaging and overlay applications on a 1.35 NA immersion scanner,” *Proc. SPIE*, vol. 7973, p. 79731G, 2011.
[140] T. Fühner, P. Evanschitzky, and A. Erdmann, “Mutual source, mask and projector pupil optimization,” *Proc. SPIE*, vol. 8326, p. 83260I, Feb. 2012.
[141] P. Evanschitzky, F. Shao, T. Fuhner, and A. Erdmann, “Compensation of mask induced aberrations by projector wavefront control,” *Proc. SPIE*, vol. 7973, p. 797329, 2011.
[142] J. Finders, M. Dusa, P. Nikolsky, Y. van Dommelen, R. Watso, T. Vandeweyer, J. Beckaert, B. Laenens, and L. Van Look, “Litho and patterning challenges for memory and logic applications at the 22-nm node,” *Proc. SPIE*, vol. 7640, p. 76400C, 2010.
[143] J. Finders and T. Hollink, “Mask 3D effects: impact on imaging and placement,” *Proc. SPIE*, vol. 7985, p. 79850I, 2011.
[144] Christiaan Huygens, *Traité de la lumieré [Treatise on Light]*. Leiden, Netherlands: Pieter van der Aa, 1690.
[145] Augustin-Jean Fresnel, “Mémoire sur la diffraction de la lumière,” *Annales de la Chemie et de Physique*, vol. 1, pp. 239–281, 1816.
[146] M. Born and E. Wolf, *Principles of optics : electromagnetic theory of propagation, interference and diffraction of light*. Cambridge, New York: Cambridge University Press, 1999.
[147] G. Kirchhoff, *Ann. d. Physik*, vol. 2, no. 18, p. 663, 1883.

[148] J. D. Gaskill, “One-Dimensional Functions,” in *Linear Systems, Fourier Transforms, and Optics*, 1st ed., New York: Wiley-Interscience, 1978, pp. 41–49.
[149] F. Zernike, “The concept of degree of coherence and its application to optical problems,” *Physica*, vol. 5, no. 8, pp. 785–795, Aug. 1938.
[150] F. Zernike, “Diffraction and Optical Image Formation,” *Proceedings of the Physical Society*, vol. 61, no. 2, pp. 158–164, Aug. 1948.
[151] F. Zernike, “The convection of light under various circumstances with special reference to Zeeman’s experiments,” *Physica*, vol. 13, no. 4–5, pp. 279–288, May 1947.
[152] F. Zernike, “The Anomalous Dilatation of Invar,” *Nature*, vol. 118, no. 2975, pp. 662–662, Nov. 1926.
[153] H. H. Hopkins, “The concept of partial coherence in optics,” *Royal Society of London. Series A, Mathematical and Physical*, vol. 208, pp. 263–277, 1951.
[154] H. H. Hopkins, “On the diffraction theory of optical images,” *Royal Society of London. Series A, Mathematical and Physical*, vol. 217, pp. 408–432, 1953.
[155] N. Cobb, “Sum of coherent systems decomposition by SVD,” University of California at Berkeley, Department of Electrical Engineering and Computer Science, 1995.
[156] N. B. Cobb, A. Zakhor, and E. A. Miloslavsky, “Mathematical and CAD framework for proximity correction,” *Proc. SPIE*, vol. 2726, pp. 208–222, 1996.
[157] Y. Peng and D. Z. Pan, “TIP-OPC: a new topological invariant paradigm for pixel based optical proximity correction,” *IEEE/ACM International Conference on Computer-Aided Design*, pp. 847–853, 2007.
[158] H. Volkmann, “Ernst Abbe and His Work,” *Applied Optics*, vol. 5, no. 11, p. 1720, Nov. 1966.
[159] R. L. Gordon and A. E. Rosenbluth, “Lithographic image simulation for the 21st century with 19th-century tools,” *Proc. SPIE*, vol. 5182, pp. 73–87, 2004.
[160] R. J. Socha, “Propagation Effects of Partially Coherent Light in Optical Lithography and Inspection,” University of California, Berkeley, 1997.
[161] A. Erdmann, P. Evanschitzky, and P. De Bisschop, “Mask and wafer topography effects in immersion lithography,” *Proc. SPIE*, vol. 5754, pp. 383–394, 2004.
[162] A. Erdmann, G. Citarella, P. Evanschitzky, H. Schermer, V. Philipsen, and P. De Bisschop, “Validity of the Hopkins approximation in simulations of hyper-NA (NA > 1) line-space structures for an attenuated PSM mask,” *Proc. SPIE*, vol. 6154, p. 61540G–12, 2006.
[163] M. S. Yeung, D. Lee, R. S. Lee, and A. R. Neureuther, “Extension of the Hopkins theory of partially coherent imaging to include thin-film interference effects,” *Proc. SPIE*, vol. 1927, pp. 452–463, 1993.
[164] B. W. Smith, L. V. Zavyalova, and A. Estroff, “Benefiting from polarization effects on high-NA imaging,” *Proc. SPIE*, vol. 5377, pp. 68–79, 2004.
[165] A. Estroff, Y. Fan, A. Bourov, B. Smith, P. Foubert, L. H. Leunissen, V. Philipsen, and Y. Aksenov, “Mask-induced polarization effects at high NA,” *Proc. SPIE*, vol. 5754, pp. 555–566, 2005.
[166] D. C. Cole, E. Barouch, U. Hollerbach, and S. A. Orszag, “Extending scalar aerial image calculations to higher numerical apertures,” *J. Vac. Sci. Technol. B*, vol. 10, no. 6, p. 3037, Nov. 1992.

[167] Bruce W. Smith, “Optics for Photolithography: Polarized Masks,” in *Microlithography: Science and Technology*, 2nd ed., Bruce W. Smith and Kazuaki Suzuki, Eds. Boca Raton: CRC Press, 2007, pp. 220–221.
[168] W. J. Smith, “Aberrations,” in *Modern optical engineering: the design of optical systems*, New York: McGraw Hill, 2000, pp. 61–89.
[169] W. J. Smith, “Lens Design Data,” in *Modern lens design*, New York: McGraw-Hill, 2005, pp. 85–103.
[170] D. Malacara, “Zernike Polynomial and Wavefront Fitting,” in *Optical shop testing*, Hoboken: Wiley-Interscience, 2007, pp. 498–543.
[171] R. K. Tyson, “Conversion of Zernike aberration coefficients to Seidel and higher-order power-series aberration coefficients,” *Opt. Lett.*, vol. 7, pp. 262–264, 1982.
[172] Rocchini, “Image of the Zernike_polynomials values.” Creative Commons Attribution 3.0 License, 2009.
[173] Bruce W. Smith, “Optics for Photolithography: Imaging Aberrations and Defocus,” in *Microlithography: Science and Technology*, 2nd ed., Bruce W. Smith and Kazuaki Suzuki, Eds. Boca Raton: CRC Press, 2007, pp. 192–194.
[174] T. Matsuyama, Y. Ohmura, and D. M. Williamson, “The lithographic lens: its history and evolution,” *Proc. SPIE*, vol. 6154, pp. 615403–14, 2006.
[175] N. Seong, G. Yeo, H. Cho, and J.-T. Moon, “Measurement of lens aberration by using in-situ interferometer and classification of lens for correct application,” *Proc. SPIE*, vol. 4000, pp. 30–39, 2000.
[176] C. J. Progler and A. K. K. Wong, “Zernike coefficients: are they really enough?,” *Proc. SPIE*, vol. 4000, pp. 40–52, 2000.
[177] B. Macdonald, R. Hunter Jr., and A. Smith, “Imaging and illumination system with aspherization and aberration correction by phase steps,” U.S. Patent 5136413Aug-1992.
[178] A. Smith and R. Hunter, “Method and apparatus for measurement of exit pupil transmittance,” U.S. Patent 7688426Mar-2010.
[179] H. Sewell, J. A. McClay, A. Guzman, and C. Lafiandra, “Aberration control for 70-nm optical lithography,” *Proc. SPIE*, vol. 4404, pp. 279–289, 2001.
[180] Tsujiuchi, “A density filter improving aberrant optical image,” *Journal of the Physical Society of Japan*, vol. 12, p. 744, 1957.
[181] Tsujiuchi, “Correction of optical images by compensation of aberrations by spatial frequency filtering,” *Progress in Optics*, vol. 2, p. 133, 1963.
[182] T. Horiuchi, K. Harada, S. Matsuo, Y. Takeuchi, E. Tamechika, and Y. Mimura, “Resolution Enhancement by Oblique Illumination Optical Lithography Using a Transmittance-Adjusted Pupil Filter,” *Jpn. J. Appl. Phys.*, vol. 34, pp. 1698–1708, 1995.
[183] R. von Bunau, G. Owen, and R. F. W. Pease, “Depth of focus enhancement in optical lithography,” *J. Vac. Sci. Technol. B*, vol. 10, pp. 3047–3054, 1992.
[184] B. W. Smith and H. Kang, “Spatial frequency filtering in the pellicle plane,” *Proc. SPIE*, vol. 4000, pp. 252–265, 2000.
[185] J. Kye and B. La Fontaine, “Pupil filtering for a lithographic tool,” U.S. Patent 6555274Apr-2003.

[186] B. W. Smith, L. Zavyalova, S. G. Smith, and J. S. Petersen, “Resolution and DOF improvement through the use of square-shaped illumination,” *Proc. SPIE*, vol. 3679, pp. 408–419, 1999.
[187] B. W. Smith and G. Vandenberghe, “Image enhancement through square illumination shaping,” *Proc. SPIE*, vol. 4691, pp. 1500–1503, 2002.
[188] T. E. Jewell and D. L. White, “Spatial frequency doubling lithography (SFDL) of periodic structures for integrated optical circuit technology,” *Journal of Lightwave Technology*, vol. 7, pp. 1386–1393, 1989.
[189] S. Butt and M. Burkhardt, “Method and apparatus for amplitude filtering in the frequency plane of a lithographic projection system,” U.S. Patent 6940583Sep-2005.
[190] G. Gaida and H.-J. Miesner, “Optical imaging system having an expand depth of field,” U.S. Patent 7209293Apr-2007.
[191] X. Liu and X. Cai, “Optical tracking system, and optical element therefore with quartic phase plate,” U.S. Patent 20050146790Jul-2005.
[192] G. Benner and M. Matijevic, “Phase contrast electron microscope,” U.S. Patent 7741602Jun-2010.
[193] F. Hosokawa, K. Nagayama, and R. Danev, “Lens system for phase plate for transmission electron microscope and transmission electron microscope,” U.S. Patent 6744048Jun-2004.
[194] K. Nagayama and R. Danev, “Thin-film phase plate, phase-contrast electron microscope using same, and method of preventing charging of phase plate,” U.S. Patent 20040190645Jan-2002.
[195] K. Schultheiß, F. Pérez-Willard, B. Barton, D. Gerthsen, and R. R. Schröder, “Fabrication of a Boersch phase plate for phase contrast imaging in a transmission electron microscope,” *Review of Scientific Instruments*, vol. 77, no. 3, pp. 033701–033701–4, Mar. 2006.
[196] Y. S. Chu, J. M. Yi, F. De Carlo, Q. Shen, W.-K. Lee, H. J. Wu, C. L. Wang, J. Y. Wang, C. J. Liu, C. H. Wang, S. R. Wu, C. C. Chien, Y. Hwu, A. Tkachuk, W. Yun, M. Feser, K. S. Liang, C. S. Yang, J. H. Je, and G. Margaritondo, “Hard-x-ray microscopy with Fresnel zone plates reaches 40 nm Rayleigh resolution,” *Applied Physics Letters*, vol. 92, no. 10, pp. 103119–3, Mar. 2008.
[197] T. Matsuyama, Y. Shibazaki, Y. Ohmura, and T. Suzuki, “High-NA and low-residual-aberration projection lens for DUV scanner,” *Proc. SPIE*, vol. 4691, pp. 687–695, 2002.
[198] Y. Uehara, T. Matsuyama, T. Nakashima, Y. Ohmura, T. Ogata, K. Suzuki, and N. Tokuda, “Thermal aberration control for low-k1 lithography,” *Proc. SPIE*, vol. 6520, p. 65202V–11, 2007.
[199] J. Bekaert, “Characterization and control of dynamic lens heating effects under high volume manufacturing conditions,” *Proc. SPIE*, vol. 7973, p. 79730V, 2011.
[200] C. Pierrat and A. K. K. Wong, “MEF revisited: low k 1 effects versus mask topography effects,” *Proc. SPIE*, vol. 5040, pp. 193–202, 2003.
[201] J. Ruoff, J. T. Neumann, E. Schmitt-Weaver, E. van Setten, N. le Masson, C. Progler, and B. Geh, “Polarization-induced astigmatism caused by topographic masks,” *Proc. SPIE*, vol. 6730, p. 67301T–15, 2007.

[202] R. L. Kostelak, C. Pierrat, J. G. Garofalo, and S. Vaidya, "Exposure characteristics of alternate aperture phase-shifting masks fabricated using a subtractive process," *J. Vac. Sci. Technol. B*, vol. 10, no. 6, p. 3055, Nov. 1992.
[203] K. Adam and A. R. Neureuther, "Simplified models for edge transitions in rigorous mask modeling," *Proc. SPIE*, vol. 4346, pp. 331–344, 2001.
[204] M. Burkhardt, R. L. Gordon, M. S. Hibbs, and T. A. Brunner, "Through-pitch correction of scattering effects in 193-nm alternating phase-shift masks," *Proc. SPIE*, vol. 4691, no. 1, pp. 348–358, Jul. 2002.
[205] R. Ferguson, R. Martino, R. Budd, G. Hughes, J. Skinner, J. Staples, C. Ausschnitt, and J. Weed, "Etched-quartz fabrication issues for a 0.25 mu m phase-shifted dynamic random access memory application," *Proc. SPIE*, vol. 11, pp. 2645–2650, 1993.
[206] A. Erdmann, "Topography effects and wave aberrations in advanced PSM technology," *Proc. SPIE*, vol. 4346, pp. 345–355, 2001.
[207] R. L. Gordon and C. A. Mack, "Lithography simulation employing rigorous solutions to Maxwell's equations," *Proc. SPIE*, vol. 3334, pp. 176–196, 1998.
[208] M. S. Yeung and E. Barouch, "Application of the hybrid finite-difference time-domain method to modeling curved surfaces in three-dimensional lithography simulation," *Proc. SPIE*, vol. 3679, pp. 1093–1103, 1999.
[209] M. S. Yeung and E. Barouch, "Three-dimensional mask transmission simulation using a single integral equation method," *Proc. SPIE*, vol. 3334, pp. 704–713, 1998.
[210] E. Barouch, U. Hollerbach, and S. A. Orszag, "Aerial image of 3D phase-shifted reticle: 3D fast aerial image model," *Proc. SPIE*, vol. 2197, pp. 442–454, 1994.
[211] P. Evanschitzky, A. Erdmann, and T. Fuhner, "Extended Abbe approach for fast and accurate lithography imaging simulations," *Proc. SPIE*, vol. 7470, pp. 747007–11, 2009.
[212] A. Erdmann and C. M. Friedrich, "Rigorous diffraction analysis for future mask technology," *Proc. SPIE*, vol. 4000, pp. 684–694, 2000.
[213] A. K. K. Wong and A. R. Neureuther, "Polarization effects in mask transmission," *Proc. SPIE*, vol. 1674, pp. 193–200, 1992.
[214] A. K. K. Wong, "Rigorous three-dimensional time-domain finite-difference electromagnetic simulation," University of California, Berkeley, 1994.
[215] S. Rizvi, "Finite Difference Time Domain Method," in *Handbook of Photomask Manufacturing Technology*, Boca Raton: CRC Press, 2005, pp. 660–667.
[216] K. Adam, "Domain decomposition methods for electromagnetic simulation of scattering from three-dimensional structures with applications in lithography," University of California, Berkeley, 2001.
[217] T. V. Pistor, A. R. Neureuther, and R. J. Socha, "Modeling oblique incidence effects in photomasks," *Proc. SPIE*, vol. 4000, pp. 228–237, 2000.
[218] A. K. K. Wong, "Two-dimensional electromagnetic simulation of topography scattering and diffraction for optical lithography," University of California, Berkeley, 1992.
[219] T. V. Pistor, "Electromagnetic Simulation and Modeling with Applications in Lithography," University of California, Berkeley, 2001.
[220] M. P. Davidson, B. H. Kleemann, and J. Bischoff, "Comparison between rigorous light-scattering methods," *Proc. SPIE*, vol. 3051, pp. 606–619, 1997.

[221] C. B. BURCKHARDT, “Diffraction of a Plane Wave at a Sinusoidally Stratified Dielectric Grating,” *J. Opt. Soc. Am.*, vol. 56, no. 11, pp. 1502–1508, Nov. 1966.
[222] P. Evanschitzky and A. Erdmann, “Fast near field simulation of optical and EUV masks using the waveguide method,” *Proc. SPIE*, vol. 6533, p. 65330Y–12, 2007.
[223] N. I. Nikolaev and A. Erdmann, “Rigorous simulation of alignment for microlithography,” *J. Micro/Nanolith. MEMS MOEMS*, vol. 2, pp. 220–226, 2003.
[224] S. Burger, L. Zschiedrich, F. Schmidt, P. Evanschitzky, and A. Erdmann, “Benchmark of rigorous methods for electromagnetic field simulations,” *Proc. SPIE*, vol. 7122, p. 71221S–12, 2008.
[225] S. Burger, R. Kohle, L. Zschiedrich, W. Gao, F. Schmidt, R. Marz, and C. Nolscher, “Benchmark of FEM, waveguide and FDTD algorithms for rigorous mask simulation,” *Proc. SPIE*, vol. 5992, pp. 599216–12, 2005.
[226] G. L. Wojcik, D. K. Vaughan, J. Mould, F. A. Leon, Q.-D. Qian, and M. A. Lutz, “Laser alignment modeling using rigorous numerical simulations,” *Proc. SPIE*, pp. 292–303, Jul. 1991.
[227] J. Tirapu-Azpiroz, P. Burchard, and E. Yablonovitch, “Boundary layer model to account for thick mask effects in photolithography,” *Proc. SPIE*, vol. 5040, pp. 1611–1619, 2003.
[228] V. Agudelo, P. Evanschitzky, A. Erdmann, T. Fuhner, F. Shao, S. Limmer, and D. Fey, “Accuracy and performance of 3D mask models in optical projection lithography,” *Proc. SPIE*, vol. 7973, p. 79730O–11, 2011.
[229] K. D. Lucas, H. Tanabe, and A. J. Strojwas, “Efficient and rigorous three-dimensional model for optical lithography simulation,” *J. Opt. Soc. Am. A*, vol. 13, pp. 2187–2199, 1996.
[230] M. Kempsell Sears, G. Fenger, J. Mailfert, and B. W. Smith, “Extending SMO into the lens pupil domain,” *Proc. SPIE*, vol. 7973, p. 79731B, 2011.
[231] J. de Klerk, C. Wagner, R. Droste, L. Levasier, L. Jorritsma, E. van Setten, H. Kattouw, J. Jacobs, and T. Heil, “Performance of a 1.35NA ArF immersion lithography system for 40-nm applications,” *Proc. SPIE*, vol. 6520, p. 65201Y–14, 2007.
[232] J. Holwill, G. McIntyre, W. Poppe, and A. R. Neureuther, “Layout ‘hot spots’ for advancing optical technologies,” *Proc. SPIE*, vol. 6154, p. 61543M–9, 2006.
[233] J. Rubinstein and A. R. Neureuther, “Post-decomposition assessment of double patterning layouts,” *Proc. SPIE*, vol. 6924, p. 69240O–12, 2008.
[234] K. van I. Schenau, H. Bakker, M. Zellenrath, R. Moerman, J. Linders, T. Rohe, and W. Emer, “System qualification and optimization for imaging performance on the 0.80-NA 248-nm step-and-scan systems,” *Proc. SPIE*, vol. 4691, pp. 637–651, 2002.
[235] J. E. Gortych and D. M. Williamson, “Effects of higher order aberrations on the process window,” *Proc. SPIE*, vol. 1463, pp. 368–381, 1991.
[236] D. G. Flagello, J. de Klerk, G. Davies, R. Rogoff, B. Geh, M. Arnz, U. Wegmann, and M. Kraemer, “Toward a comprehensive control of full-field image quality in optical photolithography,” *Proc. SPIE*, vol. 3051, pp. 672–685, 1997.
[237] T. A. Brunner, “Impact of lens aberrations on optical lithography,” *IBM Journal of Research and Development*, vol. 41, no. 1.2, pp. 57–67, 1997.

[238] K. Adam, Y. Granik, A. Torres, and N. B. Cobb, "Improved modeling performance with an adapted vectorial formulation of the Hopkins imaging equation," *Proc. SPIE*, vol. 5040, pp. 78–91, 2003.
[239] V. Philipsen, J. Bekaert, G. Vandenberghe, R. Jonckheere, D. Van Den Broeke, and R. Socha, "Mask topography effect in chromeless phase lithography," *Proc. SPIE*, vol. 5567, pp. 669–679, 2004.
[240] A. Erdmann, "Mask modeling in the low k1 and ultrahigh NA regime: phase and polarization effects," *Proc. SPIE*, vol. 5835, pp. 69–81, 2005.
[241] M. G. Moharam and T. K. Gaylord, "Rigorous coupled-wave analysis of planar-grating diffraction," *J. Opt. Soc. Am.*, vol. 71, no. 7, pp. 811–818, Jul. 1981.
[242] M. D. Smith and C. A. Mack, "Methods for benchmarking photolithography simulators," *Proc. SPIE*, vol. 5040, pp. 57–68, 2003.
[243] M. D. Smith, J. D. Byers, and C. A. Mack, "Methods for benchmarking photolithography simulators: part II," *Proc. SPIE*, vol. 5377, pp. 1475–1486, 2004.
[244] M. D. Smith, T. Graves, J. D. Byers, and C. A. Mack, "Methods for benchmarking photolithography simulators: part III," *Proc. SPIE*, vol. 5992, p. 59925H–9, 2005.
[245] T. Graves, M. D. Smith, and C. A. Mack, "Methods for benchmarking photolithography simulators: part IV," *Proc. SPIE*, vol. 6154, p. 61542X–11, 2006.
[246] T. Graves, M. D. Smith, and S. H. Kapasi, "Methods for benchmarking photolithography simulators: part V," *Proc. SPIE*, vol. 7640, pp. 764033–7, 2010.
[247] *MATLAB Function Reference*. Natick, MA: The MathWorks, Inc., 2010.
[248] A. Tarantola, *Inverse Problem Theory and Methods for Model Parameter Estimation*. Philadelphia: Society for Industrial and Applied Mathematics, 2005.
[249] S. Luke, *Essentials of Metaheuristics*. LuLu, available for free at http://cs.gmu.edu/~sean/book/metaheuristics/, 2011.
[250] J. Yuan and C. Svensson, "A simulation-based fast algorithm for CMOS circuit speed optimization," *IEEE International Symposium on Circuits and Systems*, vol. 2, pp. 868–871, 1989.
[251] L. M. Grzesiak, V. Meganck, J. Sobolewski, and B. Ufnalski, "Genetic Algorithm for Parameters Optimization of ANN-based Speed Controller," *The International Conference on "Computer as a Tool"*, pp. 1700–1705, 2007.
[252] A. A. Khan and O. A. Mohammed, "Parameter optimization for sensorless position and speed control of permanent magnet motor at low speed using genetic algorithm," *IEEE/PES Power Systems Conference and Exposition*, pp. 1–5, 2009.
[253] C. Darwin, *On the Origin of Species by Means of Natural Selection, or the Preservation of Favoured Races in the Struggle for Life*. New York: Bantam Dell, 1859.
[254] A. Erdmann, T. Fuehner, T. Schnattinger, and B. Tollkuehn, "Toward automatic mask and source optimization for optical lithography," *Proc. SPIE*, vol. 5377, pp. 646–657, 2004.
[255] T. Fuhner, A. Erdmann, and S. Seifert, "Direct optimization approach for lithographic process conditions," *J. Micro/Nanolith. MEMS MOEMS*, vol. 6, pp. 031006–20, 2007.
[256] T. Matsunawa, H. Nosato, H. Sakanashi, M. Murakawa, N. Murata, T. Terasawa, T. Tanaka, N. Yoshioka, O. Suga, and T. Higuchi, "The novel approach for optical

proximity correction using genetic algorithms," *Proc. SPIE*, vol. 5992, pp. 599254–9, 2005.
[257] B. Tollkuhn, T. Fuehner, D. Matiut, A. Erdmann, A. Semmler, B. Kuechler, and G. Kokai, "Will Darwin's law help us to improve our resist models?," *Proc. SPIE*, vol. 5039, pp. 291–302, 2003.
[258] M. Kempsell Sears and B. W. Smith, "Modeling the effects of pupil manipulated spherical aberration in optical nanolithography," *J. Micro/Nanolith. MEMS MOEMS*, vol. 12, no. 1, pp. 0130081–0130088, Feb. 2013.
[259] T. Castenmiller, F. van de Mast, T. de Kort, C. van de Vin, M. de Wit, R. Stegen, and S. van Cleef, "Towards ultimate optical lithography with NXT:1950i dual stage immersion platform," *Proc. SPIE*, vol. 7640, p. 76401N, 2010.
[260] C. Bencher, H. Dai, and Y. Chen, "Gridded design rule scaling: taking the CPU toward the 16nm node," *Proc. SPIE*, vol. 7274, p. 72740G–10, 2009.
[261] JSR Corporation, "Electronic Materials." [Online]. Available: http://www.jsr.co.jp/jsr_e/pd/ec_index.shtml. [Accessed: 28-Jun-2012].
[262] Fujifilm, "OPD 262: developer without surfactant." [Online]. Available: http://www.fujifilmusa.com/products/semiconductor_materials/photoresist-ancillaries/developers/index.html#overview. [Accessed: 28-Jun-2012].
[263] S. Tarutani, S. Kamimura, K. Fujii, K. Katou, and Y. Enomoto, "High volume manufacturing capability of negative tone development process," *Proc. SPIE*, vol. 7972, no. 1, p. 79720N, Mar. 2011.
[264] I. Englard, R. Piech, C. Masia, N. Hillel, L. Gershtein, D. Sofer, R. Peltinov, and O. Adan, "Accurate in-resolution level overlay metrology for multipatterning lithography techniques," *Proc. SPIE*, vol. 6922, p. 69221D–69221D, 2008.
[265] M. A. van de Kerkhof, W. de Boeij, H. Kok, M. Silova, J. Baselmans, and M. Hemerik, "Full optical column characterization of DUV lithographic projection tools," *Proc. SPIE*, vol. 5377, pp. 1960–1970, 2004.
[266] A. Chen, M. Dusa, J. van Schoot, T. Theeuwes, M. Janssen, K. van Ingen Schenau, and H. van der Laan, "Utilization of Insitu Metrology Capability of ASML Lithography Scanner to Improve Overall Process Control," *IEEE International Symposium on Semiconductor Manufacturing*, pp. 356 –359, Sep. 2006.
[267] L. Van Look, J. Bekaert, K. D'havé, B. Laenens, G. Vandenberghe, S. Cheng, K. Schreel, and J.-W. Gemmink, "Optical proximity stability control of ArF immersion clusters," *Proc. SPIE*, vol. 7973, p. 79730R–12, 2011.
[268] V. Philipsen, L. Leunissen, R. De Ruyter, R. Jonckheere, P. Martin, C. Wakefield, S. Johnson, M. Cangemi, A. Buxbaum, and T. Morrison, "Through-pitch characterization and printability for 65nm half-pitch alternating aperture phase shift applications," *Proc. SPIE*, vol. 5853, pp. 211–222, 2005.
[269] M. Kempsell Sears, J. Bekaert, and B. W. Smith, "Pupil wavefront manipulation for optical nanolithography," *Proc. SPIE*, vol. 8326, no. 1, p. 832611, Mar. 2012.
[270] KLA-Tencor, "ProDATA Advanced CD Analysis Software - Lithography Modeling." [Online]. Available: http://www.kla-tencor.com/lithography-modeling/pro-data.html. [Accessed: 06-Jun-2012].
[271] M. Kempsell Sears, J. Bekaert, and B. W. Smith, "Lens wavefront compensation for 3D photomask effects in subwavelength optical lithography," *Appl. Opt.*, vol. 52, no. 3, pp. 314–322, Jan. 2013.

[272] A. K. Wong and A. R. Neureuther, “Mask topography effects in projection printing of phase-shifting masks,” *IEEE Transactions on Electron Devices*, vol. 41, no. 6, pp. 895 –902, Jun. 1994.
[273] L. V. Look, B. Kasprowicz, A. Zibold, W. Degel, and G. Vandenberghe, “Image imbalance compensation in alternating phase-shift masks towards the 45nm node through-pitch imaging,” *Proc. SPIE*, vol. 5992, p. 59921S, 2005.
[274] M. Yamana, M. Lamantia, V. Philipsen, S. Wada, T. Nagatomo, and Y. Tonooka, “Comparison of lithographic performance between MoSi binary mask and MoSi attenuated PSM,” *Proc. SPIE*, vol. 7379, no. 1, p. 73791L, Apr. 2009.